NEUTRON-RICH CHROMIUM AND MANGANESE ISOTOPES AND THE ROLE OF THE NEUTRON $0g_{9/2}$ and $1d_{5/2}$ ORBITALS IN THE REGION BELOW ^{68}Ni

By

Travis Baugher

A DISSERTATION

Submitted to
Michigan State University
in partial fulfillment of the requirements
for the degree of

Physics - Doctor of Philosophy

2013

ProQuest LLC.
789 East Eisenhower Parkway
P.O. Box 1346
Ann Arbor, MI 48106 - 1346

ABSTRACT

NEUTRON-RICH CHROMIUM AND MANGANESE ISOTOPES AND THE ROLE OF THE NEUTRON $0g_{9/2}$ and $1d_{5/2}$ ORBITALS IN THE REGION BELOW ^{68}Ni

By

Travis Baugher

Intermediate-energy Coulomb excitation measurements were performed on the neutron-rich isotopes ^{58,60,62}Cr and the electric quadrupole transition probabilities, or $B(E2; 0_1^+ \rightarrow 2_1^+)$ values, of ^{60,62}Cr were determined for the first time. The results quantify the trend of increasing collectivity in the chromium isotopic chain approaching the neutron sub-shell gap $N = 40$. For ^{60,62}Cr, the ratios of neutron to proton transition matrix elements, $|M_n/M_p|$, were determined by combining the Coulomb excitation data with results from inelastic proton scattering measurements. γ-ray spectroscopy was performed on ^{63}Mn and a new transition was added to the level scheme. Excited-state lifetimes were determined for levels in ^{62}Cr and ^{63}Mn using simulations of the γ-ray detection systems. The results are compared with state-of-the-art large-scale shell-model calculations using the LNPS effective interaction, which was developed for this region. Different formulations of the $E2$ effective charge were used to calculate the theoretical $B(E2)$ and $|M_n/M_p|$ values, which are compared to the experimental values. The results emphasize the importance of the $0g_{9/2}$ and $1d_{5/2}$ neutron orbitals, which lie beyond the $N = 40$ sub-shell gap, for describing nuclear structure in this region.

TABLE OF CONTENTS

LIST OF TABLES

LIST OF FIGURES

Chapter 1

Introduction

The atomic nucleus is a quantum many-body system, consisting of two types of *nucleons*: positively charged protons and electrically neutral neutrons. The number of protons and neutrons making up a nucleus will be referred to as Z and N, respectively, and the total number of nucleons is $A = N + Z$. Nuclei are also referred to in the notation ${}^{A}X(Z)$, where $X(Z)$ is the chemical symbol for the element with Z protons. Nucleons are bound together to form a nucleus by the *strong force*. The range of the strong force is on the order of the nucleon size ($\sim 10^{-15}$ m = 1 fm) and is attractive on those lengthscales [1]. The *binding energy*, $BE(N, Z)$, of a nucleus is the difference between the sum of the masses of the constituent nucleons and the mass of the bound nucleus itself:

$$BE(N, Z) = (Zm_{\mathrm{p}} + Nm_{\mathrm{n}} - m_{N,Z})c^2. \tag{1.1}$$

In Equation 1.1, $m_{\mathrm{p}} = 938.272046(21)$ MeV/c^2 is the proton mass, $m_{\mathrm{n}} = 939.565379(21)$ MeV/c^2 is the neutron mass [2], $m_{N,Z}$ is the mass of the nucleus with N neutrons and Z protons, and $c = 299,792,458$ m/s is the speed of light [3].

By taking the difference in binding energies of neighboring nuclei, we can define the

neutron and proton *separation energies*, $S_{\rm n}(N,Z)$ and $S_{\rm p}(N,Z)$:

$$S_{\rm n}(N,Z) = BE(N,Z) - BE(N-1,Z), \tag{1.2}$$

$$S_{\rm p}(N,Z) = BE(N,Z) - BE(N,Z-1). \tag{1.3}$$

The differences in one-nucleon separation energies, $\Delta S_{\rm n}$ and $\Delta S_{\rm p}$ are

$$\begin{aligned} \Delta S_{\rm n}(N,Z) &= S_{\rm n}(N,Z) - S_{\rm n}(N+1,Z), \\ \Delta S_{\rm p}(N,Z) &= S_{\rm p}(N,Z) - S_{\rm p}(N,Z+1). \end{aligned} \tag{1.4}$$

By examining $S_{\rm n}$ and $\Delta S_{\rm n}$ as functions of neutron number, features can be observed. The top panel of Figure 1.1 shows one-neutron separation energies as a function of neutron number for even-even nuclei near stability with $N > Z$. The lines connect nuclei with the same number of protons. At neutron numbers 20, 28, 50, 82 and 126 there is a sudden decrease in neutron separation energy for the next neutron. This can be seen more dramatically in the bottom panel of Figure 1.1, which shows $\Delta S_{\rm n}(N,Z)$ for the same set of nuclei. The peaks highlight the so called *magic numbers*, and they arise from gaps in the energy levels occupied by the nucleons. Similar plots can be made for $S_{\rm p}$ and $\Delta S_{\rm p}$ which reveal the same set of magic numbers for protons.

A useful way of visualizing the nuclear landscape is the chart of the nuclides, shown in Figure 1.2. The nuclear chart gives the proton number on the vertical axis and the neutron number on the horizontal axis, so each square represents a different nuclide. The black squares represent the stable nuclides, the blue squares represent unstable nuclides that have been produced or studied, and the red region marks nuclides that may exist but have never

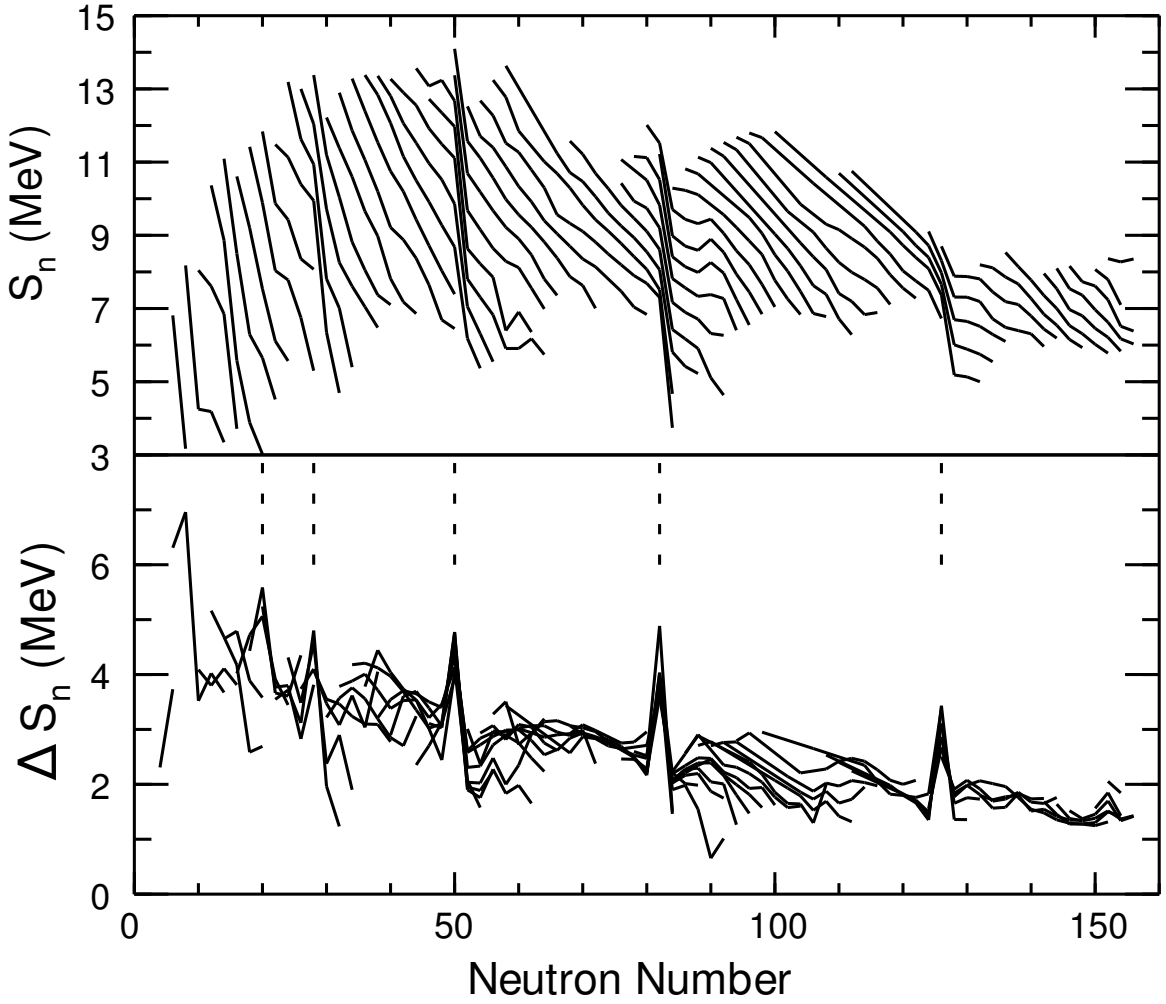

Figure 1.1: Top panel: One-neutron separation energies as a function of neutron number for even-even $N > Z$ nuclei near stability. The solid lines connect nuclei with the same Z. Bottom panel: $\Delta S_{\rm n}$ for the same set of nuclei. Figure taken from [4].

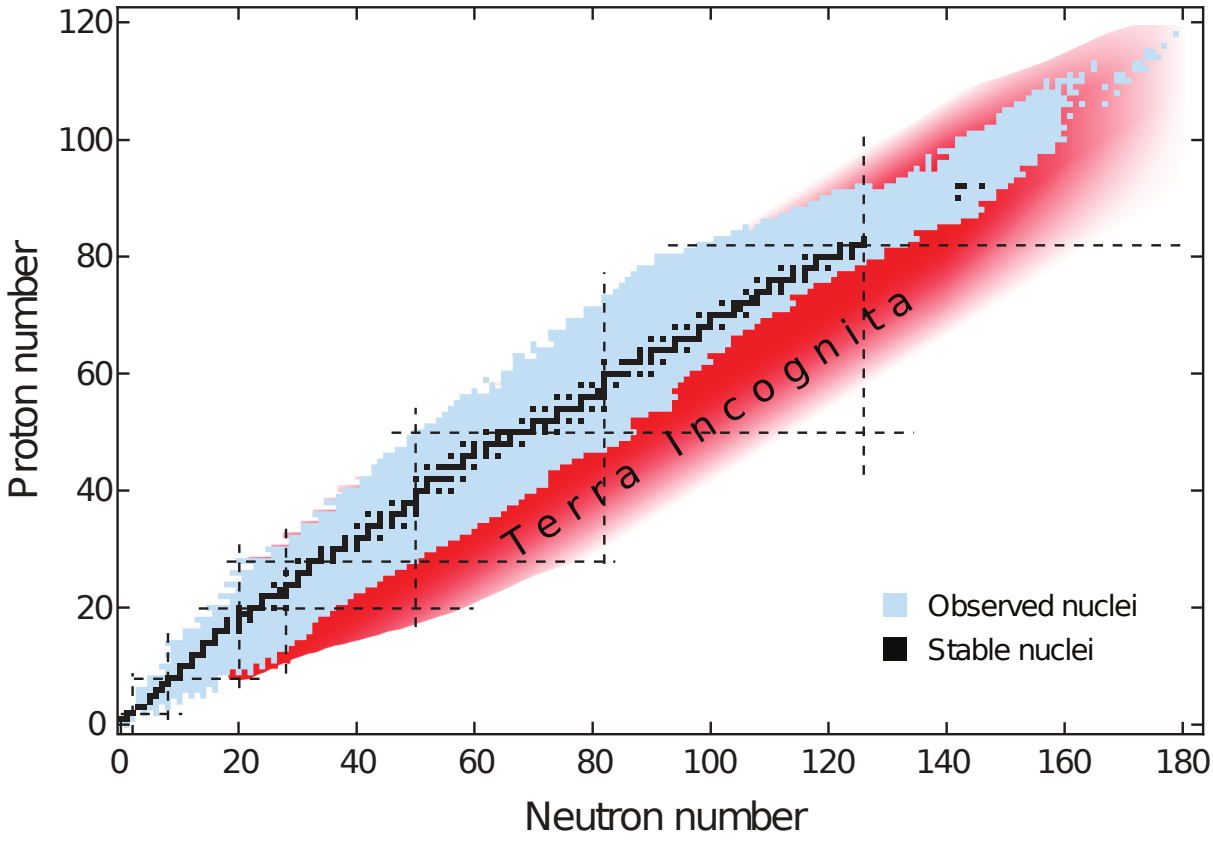

Figure 1.2: *For interpretation of the references to color in this and all other figures, the reader is referred to the electronic version of this dissertation.* A visual representation of the nuclear landscape. Each square represents a nuclide, with proton number as the y coordinate and neutron number as the x coordinate. Black squares represent stable isotopes, while blue squares represent radioactive nuclides that have been observed. The red region represents nuclides that might exist, but have not been observed. The dashed lines highlight the magic numbers of protons or neutrons.

been observed. The dashed lines at proton and neutron numbers 2, 8, 20, 28, 50, 82 and 126 indicate the magic numbers of protons and neutrons near stability. Nuclei with a magic number of either protons or neutrons are said to be *magic nuclei* and a nuclei with a magic number of both protons and neutrons is said to be *doubly magic*. Magic and doubly-magic nuclei tend to be more strongly bound than nearby nuclei, as evidenced by the abrupt changes in neutron-separation energies shown in Figure 1.1. Even-N, even-Z magic nuclei have enhanced 2_1^+ excitation energy and $B(E2 : 0_{\rm gs}^+ \rightarrow 2_1^+)$ transition probability relative to their even-even neighbors.

Nuclear shell structure arises from gaps in the energy levels occupied by the nucleons. Due to the *Pauli principle*, no two like nucleons are allowed to have the same set of quantum numbers. Nucleons have intrinsic spin angular momentum quantum number $s = 1/2$ and orbital angular momentum quantum number $\ell = 0, 1, 2, 3, \ldots$, which couple to the total angular momentum $j = \ell \pm s$. A nucleon in a single-particle state is labeled by its quantum numbers using the notation $n\ell_j$, where $n = 0, 1, 2, \ldots$ is the principle quantum number. The orbital angular momentum, ℓ, is usually referred to in spectroscopic notation, where $\ell = 0, 1, 2, 3, 4, \ldots$ is equivalent to $\ell = s, p, d, f, g, \ldots$, respectively. Each state has $2j + 1$ magnetic substates, labeled m, which run from j to $-j$ in integer steps. States are also defined by their *parity*, π, which can take the values ± 1 and is determined by $\pi = (-1)^\ell$.

The discovery of the magic numbers led to the development of the *nuclear shell model* [5, 6]. Nucleons tend to fill the lowest energy orbits preferentially. In this model, the nucleons in orbits below the last shell gap form an inert core, while the remaining nucleons outside the core are the valence nucleons. In the *extreme single-particle shell model* of a nucleus with one particle more or less than the inert core, the core contributes 0 angular momentum, and only the unpaired particle or hole determines the total spin, J, of the ground state [1]. In

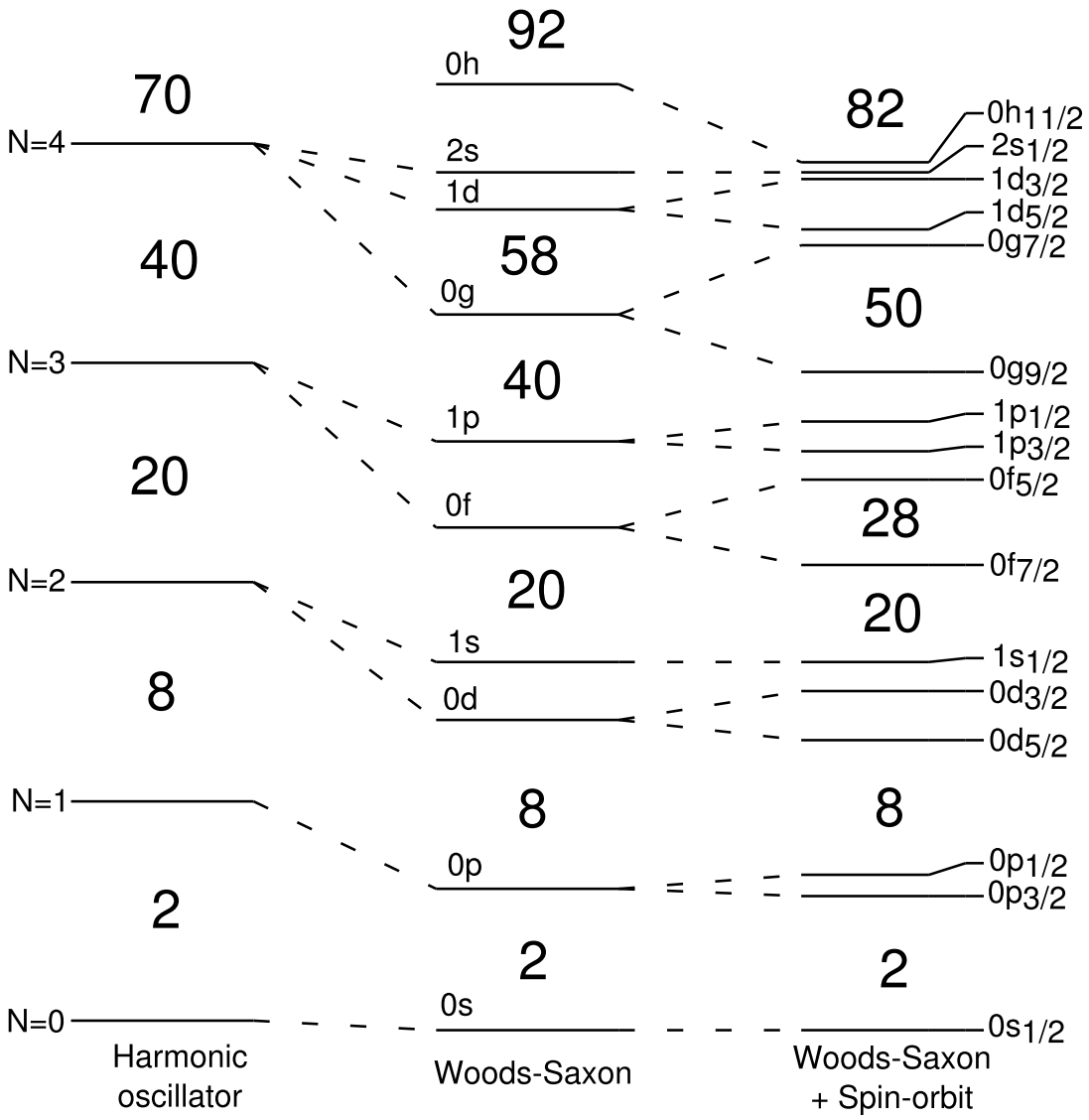

Figure 1.3: Calculated single-particle energy levels for ^{208}Pb using harmonic oscillator, Woods-Saxon, and Woods-Saxon plus spin-orbit potentials. Figure modified from [4].

more realistic shell models, multiple nucleons outside the core and mixing between nucleon configurations are taken into account [7]. For very light nuclei ($A < 12$), the no-core shell model can include all of the nucleons in the calculation [8].

A theoretical description of a nucleus is given by a solution to the Schrödinger equation, but the exact form of the nuclear Hamiltonian is not known, so assumptions must be made. In first order, one assumes that a nucleon moves in a central potential created by the other nucleons in the nucleus, thus a convenient starting point is the harmonic oscillator potential. Part (a) of Figure 1.3 shows calculated single-particle energy levels for ^{208}Pb using a harmonic oscillator potential. This simple potential is able to reproduce the first three magic numbers at 2, 8 and 20, but further predictions disagree with observation. A more realistic form is the Woods-Saxon potential:

$$V_{\mathrm{WS}}(r) = \frac{-V_0}{1 + \exp[(r - R)/a]}, \tag{1.5}$$

where V_0 is the depth of the potential, r is the radial distance from the center of the potential, and R and a are the radius and diffuseness parameters, respectively. Part (b) of Figure 1.3 shows calculated single-particle energies for ^{208}Pb with a Woods-Saxon potential. The Woods-Saxon potential breaks the degeneracy associated with the harmonic oscillator energy levels, but still fails to reproduce the observed magic numbers. As shown in Part (c) of Figure 1.3, the correct magic numbers are reproduced by adding a strong and attractive spin-orbit term to $V_{\mathrm{WS}}(r)$:

$$V_{\mathrm{so}}(r) = -V(r)\vec{\ell} \cdot \vec{s}. \tag{1.6}$$

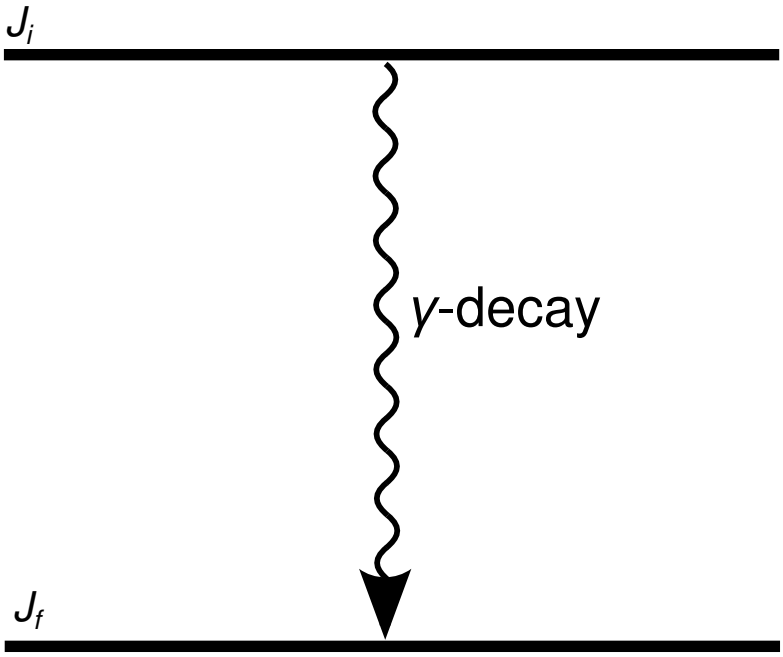

Figure 1.4: An illustration of electromagnetic decay. A bound excited state with spin J_i decays via γ-ray emission to the state J_f. The energy of the γ ray is equal to the energy difference between the states.

1.1 Electromagnetic Transitions

Most bound excited states, $|i\rangle$, will decay via γ-ray emission to a state, $|f\rangle$, that has lower energy. The energy of the γ ray is equal to the energy difference between the initial and final states (neglecting the nuclear recoil, which is usually vanishing when compared to the transition energy). The transitions can be classified according to the spin, J, and parity, π, of the initial and final states, J_i^π and J_f^π, respectively. This is schematically illustrated in Figure 1.4.

The *multipolarity*, λ, of the transition is determined by the amount of angular momentum

carried away by the photon. $\lambda = 1$ (dipole), $\lambda = 2$ (quadrupole), $\lambda = 3$ (octupole), *etc.* $\lambda = 0$ is not allowed because photons are spin-1 bosons and must carry away at least one unit of angular momentum. The allowed multipolarities are restricted by the conditions

$$|J_i - J_f| \leq \lambda \leq J_i + J_f,$$
$$\lambda \neq 0. \tag{1.7}$$

The transition is further classified as electric or magnetic based on the parities of the initial and final states, π_i and π_f, respectively, which can be either ± 1. The classification is based on the conditions:

$$\pi_i \pi_f (-1)^\lambda = \begin{cases} +1 & \text{electric} \\ \\ -1 & \text{magnetic.} \end{cases} \tag{1.8}$$

The notation $\sigma = E$ or M is used to refer to electric and magnetic transitions, respectively. The transition rate, T, depends on σ, λ and its projection, μ:

$$T_{fi}^{\sigma\lambda\mu} = \frac{2}{\epsilon_0 \hbar} \frac{\lambda + 1}{\lambda[(2\lambda+1)!!]^2} \left(\frac{E_\gamma}{\hbar c}\right)^{2\lambda+1} |\langle f|\mathcal{M}_{\sigma\lambda\mu}|i\rangle|^2. \tag{1.9}$$

$\mathcal{M}_{\sigma\lambda\mu}$ is the electromagnetic operator for the $\sigma\lambda\mu$ radiation. In many experiments, the M states are not observed individually, so it is useful to average over the projections of the initial state and sum over the projections of the final state and multipolarity:

$$T_{fi}^{\sigma\lambda} = \frac{1}{2J_i + 1} \sum_{M_i} \sum_{\mu M_f} T_{fi}^{\sigma\lambda\mu} \tag{1.10}$$

$$= \frac{2}{\epsilon_0 \hbar} \frac{\lambda + 1}{\lambda[(2\lambda+1)!!]^2} \left(\frac{E_\gamma}{\hbar c}\right)^{2\lambda+1} B(\sigma\lambda; i \to f). \tag{1.11}$$

The quantity $B(\sigma\lambda; i \to f)$ is the *reduced transition probability* and is defined as:

$$B(\sigma\lambda; i \to f) \equiv \frac{1}{2J_i + 1} |\langle f || \mathcal{M}_{\sigma\lambda} || i \rangle|^2. \tag{1.12}$$

The double bar notation indicates that M_i, M_f and μ have been summed over. The $B(\sigma\lambda)$ value depends on the direction of the transition. For a transition from state a to state b, the relationship between $B(\sigma\lambda; a \to b)$ and $B(\sigma\lambda; b \to a)$ is

$$B(\sigma\lambda; b \to a) = \frac{2J_a + 1}{2J_b + 1} B(\sigma\lambda; a \to b). \tag{1.13}$$

If state b is higher in energy than a, we define the shorthand $B(\sigma\lambda; \uparrow) \equiv B(\sigma\lambda; a \to b)$ for an excitation and $B(\sigma\lambda; \downarrow) \equiv B(\sigma\lambda; b \to a)$ for a decay.

For electric transitions, the operators $\mathcal{M}_{\sigma\lambda}$ are

$$\mathcal{M}_{E\lambda} = \sum_j^A r_j^\lambda Y_{\lambda\mu}(\theta_j, \phi_j) e_j, \tag{1.14}$$

where the sum runs over all nucleons in the nucleus, e_j is the electric charge of the j^{th} nucleon, and $Y_{\lambda\mu}$ is the spherical harmonic. For magnetic transitions,

$$\mathcal{M}_{M\lambda} = \frac{\mu_N}{\hbar c} \sum_j^A \left[\frac{2}{\lambda + 1} g_j^\ell \vec{\ell}_j + g_j^s \vec{s}_j \right] \nabla [r_j^\lambda Y_{\lambda\mu}(\theta_j, \phi_j)], \tag{1.15}$$

where g_j^s and g_j^ℓ are the spin and orbital angular momentum g-factors, respectively, $\vec{s}$ and $\vec{\ell}$ are the spin and orbital angular momentum vectors, respectively. The values of the g-factors

are $g_p^s = 5.586$, $g_n^s = -3.826$, $g_p^\ell = 1$, $g_n^\ell = 0$ for free protons and neutrons, and

$$\mu_N = \frac{e\hbar}{2m_p c} \tag{1.16}$$

is the nuclear magneton and its value is 0.105 $e$fm.

The lowest allowed electric or magnetic component with multipolarity λ usually dominates over the component with $\lambda + 2$ by several orders of magnitude. If a transition is allowed to proceed by electric and magnetic components, the component with $\lambda + 1$ will compete with the λ component. In this case it is important to consider the multipole mixing of the transition. The multipole mixing ratio, $\delta(E2/M1)$, for mixed $E2 - M1$ transitions is

$$\delta^2 \left(\frac{E2}{M1} \right) = \frac{T(E2)}{T(M1)}. \tag{1.17}$$

For $E2$ and $M1$ transitions, Equation 1.11 gives

$$T(E2) = 1.223 \times 10^9 E_\gamma^5 B(E2)\ \mathrm{s}^{-1} e^{-2} \mathrm{fm}^{-4} \mathrm{MeV}^{-5} \tag{1.18}$$

and

$$T(M1) = 1.779 \times 10^{13} E_\gamma^3 B(M1)\ \mathrm{s}^{-1} \mu_N^{-2} \mathrm{MeV}^{-3}, \tag{1.19}$$

so for mixed $E2/M1$ transitions, the mixing ratio is

$$\delta^2 \left(\frac{E2}{M1} \right) = E_\gamma^2 \frac{B(E2)}{B(M1)} 6.87 \times 10^{-5}\ \frac{\mu_N^2}{e^2 \mathrm{fm}^4 \mathrm{MeV}^2}. \tag{1.20}$$

The sign of $\delta(E2/M1)$ is defined as the opposite of the sign of the ratio of the reduced matrix elements: $\mathrm{sign}[\delta(E2/M1)] = -\mathrm{sign}[\langle f||\mathcal{M}(E2)||i\rangle / \langle f||\mathcal{M}(M1)||i\rangle]$ [4]. $\delta(E2/M1)$ can be

determined experimentally by measuring the angular distribution of γ rays from the transition [9] or by determining the $B(E2)$ value from Coulomb excitation, the lifetime of the excited state, and using Equation 1.24, for example.

The *lifetime*, τ, of an excited state is the inverse of the transition rate:

$$\tau = \frac{1}{T_{fi}}, \tag{1.21}$$

so the lifetime can be deduced from the transition rates and vice versa. For $E2$ transitions specifically,

$$\tau = \frac{816}{E_\gamma^5 B(E2:\downarrow)} e^2\mathrm{fm}^4\mathrm{MeV}^5\mathrm{ps}. \tag{1.22}$$

For mixed multipolarity transitions, the total rate is the sum of the rate for each multipolarity:

$$T_{fi} = \sum_\lambda (T_{fi}(E\lambda) + T_{fi}(M\lambda)), \tag{1.23}$$

so for mixed $E2/M1$ transitions, the lifetime is

$$\tau = \frac{\delta^2}{1+\delta^2} \frac{816}{E_\gamma^5 B(E2:\downarrow)} e^2\mathrm{fm}^4\mathrm{MeV}^5\mathrm{ps}. \tag{1.24}$$

$E2$ and mixed $E2/M1$ transitions are the most important in the discussions in this thesis.

1.2 Nuclear Collectivity and Deformation

In the single-particle model, nuclear properties are determined by the individual nucleons. This can be a good approximation near shell closures. In contrast, nuclei, in particular those away from shell closures, also exhibit *collective* behavior, where many nucleons contribute

to the behavior of the nucleus. In the *vibrational model*, the nucleus is treated as an incompressible fluid which oscillates about an average spherical shape.

In the *rotational model*, for the most common case of quadrupole deformation, the nucleus is treated as a statically deformed rotor, which rotates about an axis perpendicular to the symmetry axis. The deformation is characterized by the *quadrupole deformation parameter*, β, with the radius, $R(\theta, \phi)$, described by

$$R(\theta, \phi) = R_0(1 + \beta Y_{2,0}(\theta, \phi)), \tag{1.25}$$

where $R_0 = 1.25A^{1/3}$ is the average radius and $Y_{2,0}(\theta, \phi)$ is the spherical harmonic. In this model, $\beta > 0$ gives a *prolate* (elongated) shape, and $\beta < 0$ describes an *oblate* (flattened) shape. The deformation parameter is related to the $B(E2;\uparrow)$ value by

$$|\beta| = \frac{4\pi}{3}\frac{\sqrt{B(E2;\uparrow)}}{ZeR^2}. \tag{1.26}$$

Note that the sign of the deformation parameter cannot be determined from the $B(E2)$ value alone and therefore the prolate or oblate nature of the deformation cannot be determined from this relationship. Experimental signatures of nuclear collectivity in even-N, even-Z nuclei include a large $B(E2; 0^+_{\rm gs} \rightarrow 2^+_1)$ value and a small excited-state energy, $E(2^+_1)$.

1.3 Inelastic Scattering

Inelastic scattering is a type of a *direct reaction* [10, 11] in which the target and/or projectile are excited by the interaction with one another, while leaving each nucleus intact. Inelastic scattering experiments are sensitive to the collective structure of the nucleus. The specific

probe used to cause the excitation must be understood, as different probes have different sensitivities. An electromagnetic probe is ideal since the electromagnetic interaction is well understood and the electromagnetic force is relatively weak, so the excitation can be treated perturbatively as outlined in [12]. If the probe couples via the strong force, the interaction must be modeled, for example using the *optical model* and coupled channels calculations [10, 11].

To study stable isotopes, scattering experiments traditionally use a target made of the isotope of interest and a beam of particles acting as the probe are impinged on the target, causing excitations. To study radioactive isotopes, scattering experiments must be performed in *inverse kinematics* where the particle being studied is the projectile and the probe is the target. This is due to the simple constraint that it is impractical, if not impossible, to make a target of radioactive isotopes that may live only for milliseconds, for example. The advent of rare-isotope research facilities and advances in production techniques of radioactive ion beams has made it possible to study very short-lived isotopes [13].

1.3.1 Intermediate-energy Coulomb Excitation

Intermediate-energy Coulomb excitation is a well-developed and robust technique used to determine $B(E2)$ values from excitation cross sections [14, 15, 13]. Intermediate-energy Coulomb excitation is discussed in detail in Chapter .

1.3.2 Inelastic Proton Scattering in Inverse Kinematics

Proton inelastic scattering, denoted (p, p'), probes the proton-neutron degrees of freedom of a nucleus and strongly excites collective states in even-even nuclei. Combined with Intermediate-

energy Coulomb excitation, inelastic proton scattering can be used to determine the ratio of neutron to proton matrix elements, denoted $|M_n/M_p|$, which can provide information about the relative contributions of the neutrons and protons to a collective excitation mode. In the simplest picture of a collective nucleus, protons and neutrons contribute equally and the ratio of the matrix elements should follow N/Z. For nuclei with singly closed shells, $|M_n/M_p|$ can deviate from N/Z as the transition will be dominated by the valence nucleons. The neutron/proton matrix elements are defined as [16]

$$M_{n/p} = \int \rho_{\mathrm{fi}}^{n/p}(r) r^{\lambda+2} \mathrm{d}r, \tag{1.27}$$

where $\rho_{\mathrm{if}}^{n/p}$ is the neutron/proton transition density from state $|\mathrm{i}\rangle$ to $|\mathrm{f}\rangle$ and λ is the multipolatity of the transition.

By using a pair of probes that differ in their sensitivity to protons and neutrons, the ratio of the matrix elements can be deduced. Coulomb excitation is an electromagnetic probe, and so it is sensitive to M_p, while inelastic proton scattering at 30-50 MeV proton energy is mainly sensitive to M_n, as determined by nucleon-nucleon scattering [16]. Using the description of Bernstein *et al.*, [17], the ratio is

$$\frac{M_n}{M_p} = \frac{b_p}{b_n}\left[\frac{\delta_{(p,p')}}{\delta_p}\left(1 + \frac{b_n}{b_p}\frac{N}{Z}\right) - 1\right]. \tag{1.28}$$

In Equation 1.28, b_n/b_p is the relative sensitivity of the probes to the protons and neutrons. b_n/b_p depends on the energy at which the reaction takes place, and ranges from $b_n/b_p = 3$ at 50 MeV to $b_n/b_p = 1$ at 1 GeV [16]. $\delta_{(p,p')}$ and δ_p in Equation 1.28 are the deformation lengths deduced from inelastic proton scattering and Coulomb excitation, respectively. δ

is related to the quadrupole deformation parameter, β, by $\delta = \beta R$, where R is the nuclear radius. $\delta_{(p,p')}$ can be determined from inelastic proton scattering experiments by fitting the proton angular distribution or the inelastic cross sections with DWBA or coupled-channels calculations, while δ_p can be determined from Coulomb excitation via the relationship

$$\delta_p = \frac{4\pi}{3}\frac{\sqrt{B(E2:\uparrow)}}{ZeR}. \tag{1.29}$$

The optical model is often used to model the nuclear potential in inelastic proton scattering experiments in order to extract cross sections and $\delta_{(p,p')}$, for example. In the optical model, the nuclear potential is modeled as

$$U(r) = V(r) + iW(r), \tag{1.30}$$

where the real component accounts for elastic scattering and the imaginary part accounts for all other scattering processes. $V(r)$ typically includes a central term such as a Woods-Saxon potential, $V_0(r)$, a surface-peaked, spin-orbit term proportional to $dV_0(r)/dr\ell \cdot s$, and a Coulomb term, while $W(r)$ typically includes only central and surface-peaked terms. A detailed description of the optical-model potential can be found in, for example, [18, 19]. The parameters in the optical model potential can be determined by fitting to elastic scattering angular distributions, using a global parameter set, for example, [18, 19], or by performing folding model calculations [11].

To account for deformation, the potentials become functions of $R(\theta) = R_0[1 + \beta Y_{2,0}(\theta)]$ instead of the usual spherical radius $R = 1.25A^{1/3}$. The Schrödinger equation can then be solved with the deformed potential using the coupled channels method [10, 11]. The

quadrupole deformation parameter can then be adjusted so that the calculations agree with the experimental cross sections.

1.4 Shell Model and Effective Charge

All but the lightest nuclei are too complex for the Schrödinger equation to be solved for every particle in the A-body system. To simplify the problem, an inert core of A_{core} nucleons is chosen, thereby reducing the problem to one of $A - A_{\text{core}}$ particles. The core is typically chosen to be a nearby doubly-magic nucleus. The remaining nucleons outside the core are then the valence nucleons. Due to computational constraints, a *model space* must be chosen to limit the single-particle levels available to the valence nucleons. The valence space must be large enough to reproduce the low-lying excitations but small enough to be computationally tractable. A typical choice is to include the orbitals in the major harmonic oscillator shell of the valence nucleons. An *effective interaction*, consisting of a mean-field potential and a *residual interaction*, must be derived within the chosen model space. The residual interaction accounts for the two-body interaction, which is not included in the mean field potential. Examples of effective interactions include Cohen and Kurath for the p shell [20], USDA and USDB interactions for the sd shell [21], and GXPF1A for the pf shell [22, 23].

The Hamiltonian, H, for a system of A nucleons is

$$H = T + V \tag{1.31}$$

$$= \sum_{i}^{A} t_i + \sum_{i<j}^{A} v_{ij}, \tag{1.32}$$

where t_i is the kinetic energy operator for the i^{th} nucleon and v_{ij} is the interaction between

the i^{th} and j^{th} nucleons. The single-particle potential, U, which is the sum contribution of the potentials from all the nucleons which create the mean field, is

$$U = \sum_{i}^{A} v_i, \tag{1.33}$$

and can be the harmonic oscillator or Woods-Saxon potential plus spin-orbit. U can be added and subtracted from the Hamiltonian to give:

$$H = (T + U) + (V - U) \equiv H_0 + H_1. \tag{1.34}$$

H_0 is the mean-field Hamiltonian and H_1 is the residual interaction, which is treated as a perturbation to H_0.

Transition rates between nuclear states depend on the transition operators, $\mathcal{M}_{\sigma\lambda\mu}$. For example, the $E2$ transition operator is

$$\mathcal{M}_{E2} = \sum_{i} e r_i^2 Y^2 e_i, \tag{1.35}$$

where i sums over all nucleons, e is the charge unit, e_i is the charge of the i^{th} nucleon, Y^2 is the spherical harmonic, and r is the radius. In the reduced model space of the shell model, effects outside the model space must be taken into account. For the $E2$ operator, this is done by introducing *effective charges*, e_n and e_p, for protons and neutrons, respectively, that enter into the sum in the definition 1.35. As demonstrated in [8], introducing an effective charge is a way of taking into account interactions between the valence nucleons and the core that are left out of the shell model description due to the model space restraint, for example. As valence nucleons move in their orbits, they disturb the core nucleons and induce

a quadrupole moment of the core. The $E2$ effective charge takes into account coupling of the single-particle motion of the valence nucleons with the quadrupole vibrational modes of the core [24]. Effective charge is usually parameterized as

$$e_p/e = 1 + \delta e_p \tag{1.36}$$

$$e_n/e = \delta e_n, \tag{1.37}$$

where the $\delta e_{p/n}$ are the proton and neutron *polarization charges*. A standard value of the polarization charge is taken as 0.5 for both δe_p and δe_n. In more detailed phenomenological approaches, different sets of effective charge are used in different model spaces. For example, $\delta e_p = 0.2$ and $\delta e_n = 0.5$ in the *sd* shell [25] and $\delta e_p = 0.15$, $\delta e_n = 0.8$ [26] or $\delta e_p = 0.31$, $\delta e_n = 0.46$ [27] in the *fp* shell. These effective charges are assumed to be constant, although it is not clear that this assumption is correct throughout the model space at increasing neutron-richness, for example. The polarization charges have an isoscaler component and an isovector component which arise from the excitation of the isoscaler and isovector giant quadrupole resonances of the core coupling to the valence nucleons. To account for this, the effective charges also have isoscaler (IS) and isovector (IV) components such that $\delta e_p = \delta e_p^{IS} - \delta e_p^{IV}$ and $\delta e_n = \delta e_n^{IS} + \delta e_n^{IV}$ [26]. Bohr and Mottleson proposed N- and Z-dependent $E2$ polarization charges that take into account the neutron excess ($N - Z$) and approximates the coupling to in-phase (isoscaler) and out-of-phase (isovector) vibrations of the protons and neutrons in the core [24].

The effective charges enter into the shell-model transition probabilities via

$$\begin{aligned} B(E2; 0^+ \rightarrow 2^+) =& (e_n A_n + e_p A_p)^2 \\ =& |M_p|^2, \end{aligned} \tag{1.38}$$

as well as the proton and neutron transition matrix elements:

$$\begin{aligned} M_p &= e_n A_n + e_p A_p \\ M_n &= e_p A_n + e_n A_p, \end{aligned} \tag{1.39}$$

where A_n and A_p are the shell-model transition amplitudes for neutrons and protons, respectively. It is clear from Equations 1.38 and 1.39 that an accurate theoretical description of the transition rate and transition matrix elements depends on the understanding of the effective charges in a given shell model space.

1.5 Evolution of Nuclear Structure Away from Stability

Changes in nuclear shell structure have been observed in nuclei as a function of the *isospin* projection $T_z = \frac{1}{2}(N - Z)$. For example, the erosion of the $N = 20$ magic number has been observed in nuclei in the *island of inversion* region around ^{32}Na. Ground state $(sd)^{-2} - (fp)^{+2}$ neutron configurations that involve particle-hole excitations across $N = 20$ are energetically favored over configurations one would expect in normal level ordering [28, 29]. In the neutron-rich calcium, titanium and chromium isotopes, a new magic number at $N = 32$ was observed

[30, 31, 32, 33, 34]. Among the isotopes with $N = 40$, many changes in structure have been observed: the $N = Z = 40$ nucleus ^{80}Zr is highly deformed with a quadrupole deformation parameter of $\beta \approx 0.4$ [35], while ^{68}Ni has a high first 2^+ state and a small $B(E2; 0^+ \rightarrow 2^+)$ transition probability [36]. Only two and four protons away from ^{68}Ni, ^{66}Fe and ^{64}Cr are among the most collective nuclei in the region [37].

One cause of this evolution is the shifting of the effective single-particle energies, driven by the spin-isospin part of the nucleon-nucleon interaction [38], for example. This monopole part of the tensor force acts in addition to the spin-orbit force and affects the effective single-particle energies as a function of the isospin. A nucleon in a single-particle orbit j has a single-particle energy that is determined by the mean effect of all the other nucleons in the nucleus. When a nucleon is added to the orbit j', it changes the mean field, thus changing the effective single-particle energy of the nucleon in orbit j. The nucleons in j and j' couple to total angular momentum J. By averaging over the possible J values, the monopole component of an interaction V is [39]

$$V^T_{jj'} = \frac{\sum_J (2J+1)\langle jj'|V|jj'\rangle_{JT}}{\sum_J (2J+1)}, \tag{1.40}$$

where $\langle jj'|T|jj'\rangle_{JT}$ is the matrix element for j and j' coupled to spin J and isospin T. The $T = 0$ (proton-neutron) component of the tensor interaction is stronger than the $T = 1$ (neutron-neutron or proton-proton) component [38].

The shift in single-particle energy, $\Delta\epsilon_p(j)$, of a proton in orbital j due to a neutron in orbital j' is [38]

$$\Delta\epsilon_p(j) = \frac{1}{2}\left[V^{T=0}_{j,j'} + V^{T=1}_{j,j'}\right] n_n(j'), \tag{1.41}$$

where $n_n(j')$ is the number of neutrons in the orbital j'. So the strength of the single-particle

energy shift of j depends on the number of particles in j'. Swapping n and p gives the similar expression for the neutron single-particle energy shift.

For protons, with orbital angular momentum ℓ, and neutrons, with orbital angular momentum ℓ', the tensor force between the orbitals $j_< = \ell - 1/2$ and $j'_> = \ell' + 1/2$ and $j_> = \ell + 1/2$ and $j'_< = \ell' - 1/2$ force is attractive. For protons and neutrons in $j_<$ and $j'_<$ or $j_>$ and $j'_>$, the tensor force is repulsive. The tensor force is maximized for $\ell = \ell'$, so the strongest coupling is expected for protons and neutrons in spin-orbit partner orbitals [39, 38].

In the region below ^{68}Ni, the proton-neutron tensor force plays a key role in reducing the $N = 40$ gap between the positive-parity fp shell and the negative-parity $0g_{9/2}$ and $1d_{5/2}$ neutron orbitals. Neutron excitations into these orbitals are enhanced by this reduced energy gap, generating quadrupole collectivity [40]. The gap is reduced going from ^{68}Ni to ^{64}Cr by the combination of the repulsion between the $0f_{5/2}$ neutron orbital and the $0f_{7/2}$ proton holes and the attraction between the $0f_{7/2}$ proton holes and the $0g_{9/2}$ and $1d_{5/2}$ neutron orbitals. By measuring the $B(E2)$ values of ^{60,62}Cr, the quadrupole collectivity in this region can be further quantified.

Chapter 2

Intermediate-energy Coulomb Excitation

2.1 The Theory of Intermediate-energy Coulomb Excitation

The experimental technique used to determine the $B(E2)$ values of ^{58,60,62}Cr was intermediate-energy Coulomb excitation. In general, in Coulomb excitation, the projectile and/or target nuclei are excited from the initial state $|i\rangle$ to the final state $|f\rangle$ in the Coulomb field of one another. "Safe" (low-energy) Coulomb excitation can be accomplished by keeping the beam energy below the Coulomb barrier for the given target-projectile combination, thus ensuring that the charge distributions of the projectile and target never overlap; *i.e.*, the nuclei never come close enough for the short-range nuclear force to contribute to the excitation process. For some radioactive beams, such low energies are impractical because they are most effectively produced by in-flight fragmentation and available for experiments with more than 50 MeV/nucleon; whereas, energies no greater than 3 MeV/nucleon would be needed to keep a ^{62}Cr + ^{197}Au collision safely below the Coulomb barrier. To prevent nuclear contributions in the case of beam energies above the Coulomb barrier, events with large scattering angles, which correspond to small impact parameters (see Figure 2.1), must be excluded from the

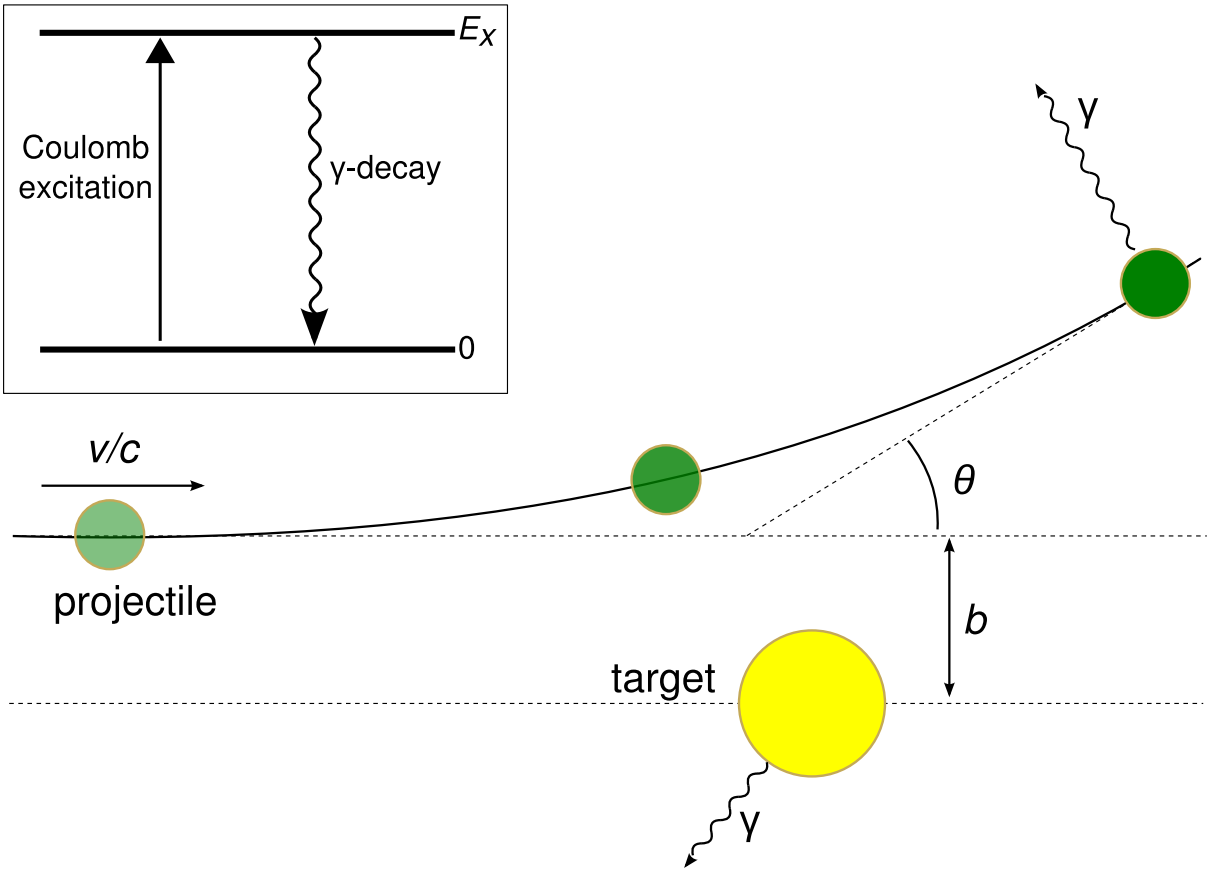

Figure 2.1: A cartoon illustrating the scattering of a projectile from a target nucleus with and impact parameter b and corresponding scattering angle θ. Inset is a diagram of the Coulomb-excitation process in which a nucleus is excited from the ground state and subsequently decays be γ-ray emission. The energy of the emitted γ ray equals the energy difference between the nuclear levels.

analysis.

The equations in this section involving Z_{p} or Z_{t} assume that the Coulomb excitation of the *projectile* is taking place. For equations describing the Coulomb excitation of the target, simply replace Z_{p} with Z_{t} and vice versa. The calculations of the Coulomb-excitation cross sections and γ-ray angular distribution coefficients used in this work were performed with a Mathematica program described in [41].

In their semi-classical theory of relativistic Coulomb excitation [12], Alder and Winther assume that the scattering takes place along a classical trajectory and that the Coulomb

excitation cross section can be described as the product of the Rutherford cross section [11] for inelastic scattering and the (small) Coulomb excitation probability $P_{i\to f}$:

$$\left(\frac{\mathrm{d}\sigma}{\mathrm{d}\Omega}\right)_{i\to f} = \left(\frac{\mathrm{d}\sigma}{\mathrm{d}\Omega}\right)_{\text{Rutherford}} P_{i\to f}, \tag{2.1}$$

where the probability to undergo Coulomb excitation, $P_{i\to f}$, is defined as the square of the excitation amplitude $a_{i\to f}$

$$P_{i\to f} = \left|a_{i\to f}\right|^2. \tag{2.2}$$

By treating the Coulomb potential as time-dependent perturbation, the excitation amplitude is

$$a_{i\to f} = \frac{1}{i\hbar}\int_{-\infty}^{\infty} \mathrm{d}t\, \mathrm{e}^{i\omega_{fi}t}\, \langle f|V(\mathbf{r}(t))|i\rangle\,. \tag{2.3}$$

Here, $\omega_{fi} = \left(E_f - E_i\right)/\hbar = \Delta E/\hbar$ and $V\left(\mathbf{r}\left(t\right)\right)$ is the Coulomb potential. For large impact parameters or high projectile velocities, Alder and Winther assume straight-line trajectories. After expanding the potential into its multipole components, $V_{\lambda\mu}\left(\mathbf{r}\right)$, and expressing it in terms of the electric multipole matrix elements, $\mathcal{M}\left(\pi\lambda\mu\right)$, where $\pi = E$ for electric transitions, $\pi = M$ for magnetic transitions, λ is the multipolarity of the excitation, and μ is its projection, the excitation amplitude can be expressed as

$$a_{i\to f} = i\sum_{\lambda} \chi^{(\lambda)}_{i\to f} f_\lambda\left(\xi\right). \tag{2.4}$$

The factor χ is a measure of the interaction strength,

$$\chi^{(\pi\lambda)}_{i\to f} \approx \frac{Z_{\mathrm{t}} e\, \langle f|\mathcal{M}\left(\pi\lambda\mu\right)|i\rangle}{\hbar c b^\lambda}, \tag{2.5}$$

where b is the distance of closest approach in the collision. $f_\lambda(\xi)$ describes how the cross section depends on the *adiabaticity* of the collision. ξ is equal to the amount of time the projectile spends in the vicinity of the target, the collision time, τ_{coll}, divided by the timescale of the internal motion of the nucleus undergoing excitation τ_{nuc}:

$$\xi = \frac{\tau_{\text{coll}}}{\tau_{\text{nuc}}}. \tag{2.6}$$

τ_{coll} depends on the particle's velocity and impact parameter,

$$\tau_{\text{coll}} = \frac{b}{\gamma v}, \tag{2.7}$$

where γ is the relativistic factor and β is the projectile speed as a fraction of the speed of light, c:

$$\gamma = \frac{1}{\sqrt{1-\beta^2}}, \tag{2.8}$$

$$\beta = \frac{v}{c} \tag{2.9}$$

τ_{nuc} depends on the energy of the excitation

$$\tau_{\text{nuc}} = \frac{1}{\omega_{fi}} = \frac{\hbar}{\Delta E}. \tag{2.10}$$

If the adiabatic parameter is large, due to a large impact parameter, low velocity or large excitation energy, the collision will be adiabatic. In this case, the nucleus moves gently through the field, following the slowly changing, time-dependent potential and is less likely to be excited. In this case, $f_\lambda(\xi)$ should fall off as $\mathrm{e}^{-\pi\xi}$ for large ξ. If ξ is small, the interaction

will be more violent and the excitation is more likely to occur. This implies that in the limit of $\xi \to 0$, $f_\lambda(\xi)$ should approach 1.

Alder and Winther show that Coulomb distortion causes the trajectory to deviate from a straight line and that this deviation is most important in the calculation of the adiabaticity parameter ξ. They introduce a rescaling of the impact parameter to account for the increased distance of closest approach due to Coulomb repulsion between the projectile and target [12]:

$$b \to b + \frac{\pi}{2}\frac{a_0}{\gamma}, \tag{2.11}$$

where

$$a_0 = \frac{Z_\mathrm{t} Z_\mathrm{p} e^2}{m_0 c^2 \beta^2} \tag{2.12}$$

is the half-distance of closest approach in a head-on collision, and m_0 is the reduced mass of the projectile and target. With the re-scaled impact parameter, ξ is:

$$\xi = \frac{\Delta E}{\hbar \gamma v}\left(b + \frac{\pi}{2}\frac{a_0}{\gamma}\right), \tag{2.13}$$

The *adiabatic cutoff* sets in when $\xi = 1$, and the corresponding impact parameter b_a is

$$b_\mathrm{a} = \frac{v\gamma\hbar}{\Delta E}, \tag{2.14}$$

above which excitations of energy greater than ΔE are not possible.

The approximate cross section is found by integrating $|\chi|^2$ over impact parameters from b_min to b_max:

$$\sigma_\lambda = 2\pi \int_{b_\mathrm{min}}^{b_\mathrm{a}} b\,\mathrm{d}b P_{i\to f} \approx 2\pi \int_{b_\mathrm{min}}^{b_\mathrm{a}} b\,\mathrm{d}b \left|\chi^{(\pi\lambda)}(b)\right|^2, \tag{2.15}$$

resulting in

$$\sigma_{\pi\lambda} \approx \left(\frac{Z_{\mathrm{t}}e^2}{\hbar c}\right)^2 \frac{\pi B\left(\pi\lambda; 0 \rightarrow \lambda\right)}{e^2 b_{\mathrm{min}}^{2\lambda-2}} \begin{cases} (\lambda-1)^{-1} & \text{for } \lambda \geq 2 \\ 2\ln\left(b_{\mathrm{a}}/b_{\mathrm{min}}\right) & \text{for } \lambda = 1 \end{cases}, \tag{2.16}$$

which is summed over all possible values of π and λ to obtain the total cross section:

$$\sigma_{i\rightarrow f} = \sum_{\pi\lambda} \sigma_{\pi\lambda}. \tag{2.17}$$

Equation 2.16 shows the proportionality of the $B(E2)$ value and the Coulomb-excitation cross section. Also of note is the dependence of the cross section on Z_{t}, the atomic number of the target. This can be exploited by using high-Z targets for Coulomb excitation experiments.

The full result is derived in [12, 41]. The resulting excitation amplitude is:

$$a_{i\rightarrow f} = -i\frac{Z_{\mathrm{t}}e^2}{\hbar v\gamma} \sum_{\pi\lambda\mu} G_{\pi\lambda\mu}\left(\frac{c}{v}\right)(-1)^{\mu} K_{\mu}\left(\xi\left(b\right)\right) k^{\lambda}\sqrt{2\lambda+1} \times \frac{\left\langle J_f M_f \middle| \mathcal{M}\left(\pi\lambda-\mu\right) \middle| J_i M_i \right\rangle}{e}, \tag{2.18}$$

where $k = \Delta E/\hbar c$ and K_{μ} are modified Bessel functions. The function $G_{\pi\lambda\mu}$ is defined for electric transitions ($\pi = E$) as

$$G_{E\lambda\mu}\left(\frac{c}{v}\right) = i^{\lambda+\mu}\frac{\sqrt{16\pi}}{\lambda\left(2\lambda+1\right)!!}\left(\frac{(\lambda-\mu)!}{(\lambda+\mu)!}\right)^{\frac{1}{2}}\left(\left(\frac{c}{v}\right)^2-1\right)^{-\frac{1}{2}} \times\left(\frac{(\lambda+1)\left(\lambda+\mu\right)}{2\lambda+1}P^{\mu}_{\lambda-1}\left(\frac{c}{v}\right)-\frac{\lambda\left(\lambda-\mu+1\right)}{2\lambda+1}P^{\mu}_{\lambda+1}\left(\frac{c}{v}\right)\right) \tag{2.19}$$

and for magnetic transitions ($\pi = M$) as

$$G_{M\lambda\mu}\left(\frac{c}{v}\right) = i^{\lambda+\mu+1}\frac{\sqrt{16\pi}}{\lambda\left(2\lambda+1\right)!!}\left(\frac{(\lambda-\mu)!}{(\lambda+\mu)!}\right)^{\frac{1}{2}}\left(\left(\frac{c}{v}\right)^2-1\right)^{-\frac{1}{2}}{}_{\mu}P_{\lambda}^{\mu}\left(\frac{c}{v}\right), \tag{2.20}$$

where P_{λ}^{μ} are the associated Legendre polynomials.

For the full cross section, Alder and Winther obtain

$$\begin{aligned}\sigma_{i\to f} &= 2\pi\int_{b_{\min}}^{\infty}\frac{b\,\mathrm{d}b}{2J_i+1}\sum_{M_iM_f}\left|a_{i\to\ f}\right|^2 \\ &= \left(\frac{Z_{\mathrm{t}}e^2}{\hbar c}\right)^2\sum_{\pi\lambda\mu}k^{2(\lambda-1)}\frac{B\left(\pi\lambda;J_i\to J_f\right)}{e^2}\left|G_{\pi\lambda\mu}\left(\frac{c}{v}\right)\right|^2 g_{\mu}\left(\xi\left(b_{\min}\right)\right),\end{aligned} \tag{2.21}$$

where $g_{\mu}\left(\xi\left(b_{\min}\right)\right)$ is defined as

$$\begin{aligned}g_{\mu}\left(\xi\left(b_{\min}\right)\right) &= 2\pi\left(\frac{\omega}{v\gamma}\right)^2\int_{b_{\min}}^{\infty}b\,\mathrm{d}b\left|K_{\mu}\left(\xi\left(b\right)\right)\right|^2 \\ &= 2\pi\int_{\xi}^{\infty}\left|K_{\mu}\left(x\right)\right|^2 x\,\mathrm{d}x,\end{aligned} \tag{2.22}$$

which can be evaluated using modified Bessel functions:

$$g_{\mu}\left(\xi\left(b_{\min}\right)\right) = g_{-\mu}\left(\xi\left(b_{\min}\right)\right) = \pi\xi^2\left[\left|K_{\mu+1}\left(\xi\right)\right|^2-\left|K_{\mu}\left(\xi\right)\right|^2-\frac{2\mu}{\xi}K_{\mu+1}\left(\xi\right)K_{\mu}\left(\xi\right)\right]. \tag{2.23}$$

2.2 Experimental Considerations

In this work, the minimum impact parameter b_{min} was taken as

$$b_{\text{min}} = r_0 \left(A_{\text{t}}^{1/3} + A_{\text{p}}^{1/3} \right) + 2 \text{ fm}, \tag{2.24}$$

where $r_0 = 1.25\,\text{fm}$. The choice of adding 2 fm to the "touching-spheres" radius is based on work done in [42, 13]. The relationship between b and θ is [43]:

$$b = \frac{a_0}{\gamma} \cot \left(\frac{\theta_{\text{cm}}}{2} \right), \tag{2.25}$$

where a_0 is defined in Equation 2.12.

The experimentally determined Coulomb-excitation cross section σ is calculated as

$$\sigma = \frac{N_\gamma}{N_{\text{beam}} N_{\text{target}} \epsilon}, \tag{2.26}$$

where N_γ is the intensity of the γ-ray peak resulting from the de-excitation of the Coulomb-excited nucleus. Figure 2.1 shows a schematic of the excitation and de-excitation process. N_{target} is the number of target atoms, N_{beam} is the number of beam particles, and ϵ is the detection efficiency of all detection systems.

2.3 Angular Distribution of γ rays

Because the magnetic substates are not populated equally in Coulomb excitation[1], the γ-ray emission is anisotropic. This is important in determining the efficiency of the γ-ray detection

[1] see, for example [44, 45]

system to γ rays emitted following Coulomb excitation if less than 4π are covered. The angular distribution can be parametrized as

$$W(\theta) = \sum_{k \text{ even}} a_k P_k(\cos\theta), \tag{2.27}$$

where the index k runs from 0 to the smaller of 2λ or $2J_i$, and P_k are the Legendre polynomials. The coefficients a_k are given by [41, 46]:

$$a_k = \sum_{\mu L L'} \left| G_{\lambda\mu}\left(\frac{c}{v}\right)\right|^2 g_\mu(\xi)(-1)^\mu \begin{pmatrix} \lambda & \lambda & k \\ \mu & -\mu & 0 \end{pmatrix} \times \begin{Bmatrix} J_f & J_f & k \\ \lambda & \lambda & J_i \end{Bmatrix} F_k\left(L, L', J_{ff}, J_f\right)\sqrt{2k+1}\,\delta_L\delta_{L'}. \tag{2.28}$$

The $\gamma-\gamma$ correlation function $F_k\left(L, L', J_f, J_i\right)$ is

$$F_k\left(L, L', J_f, J_i\right) = (-1)^{J_f+J_i-1}\sqrt{(2k+1)(2J_i+1)(2L+1)(2L'+1)} \times \begin{pmatrix} L & L' & k \\ 1 & -1 & 0 \end{pmatrix} \begin{Bmatrix} L & L' & k \\ J_f & J_i & J_f \end{Bmatrix}. \tag{2.29}$$

Chapter 3

Experimental Devices

3.1 Beam Production

The experimental measurements were performed at the National Superconducting Cyclotron Laboratory (NSCL) at Michigan State University. A diagram of the NSCL Coupled Cyclotron Facility (CCF) is shown in Figure 3.1. The process of producing a radioactive beam at the NSCL [47] begins with stable atoms which must be ionized before they can be accelerated. The ions are accelerated in the K500 cyclotron to $\sim 0.15c$ before being transferred to the K1200 cyclotron where they are further stripped of electrons and accelerated to $\sim 0.5c$. After extraction from the K1200, the primary beam is then impinged on a production target which fragments the primary beam into many isotopes, most of which need to be discarded while keeping the isotopes of interest. This is accomplished by the A1900 fragment separator [48]. Finally, the desired beam of typically short-lived isotopes is sent to the experimental area.

Ionization is accomplished with one of three ion sources. The Superconducting ECR (SC-ECR) [49], Advanced Room TEMperature Ion Source (ARTEMIS) [50] and Superconducting Source for Ions (SuSI) [51, 52]. All use the *electron cyclotron resonance* (ECR) method of ionizing the atoms. If the desired primary beam is a solid, it can be heated in an oven until it vaporizes and is then injected into the ion source where it is confined to a magnetic trap.

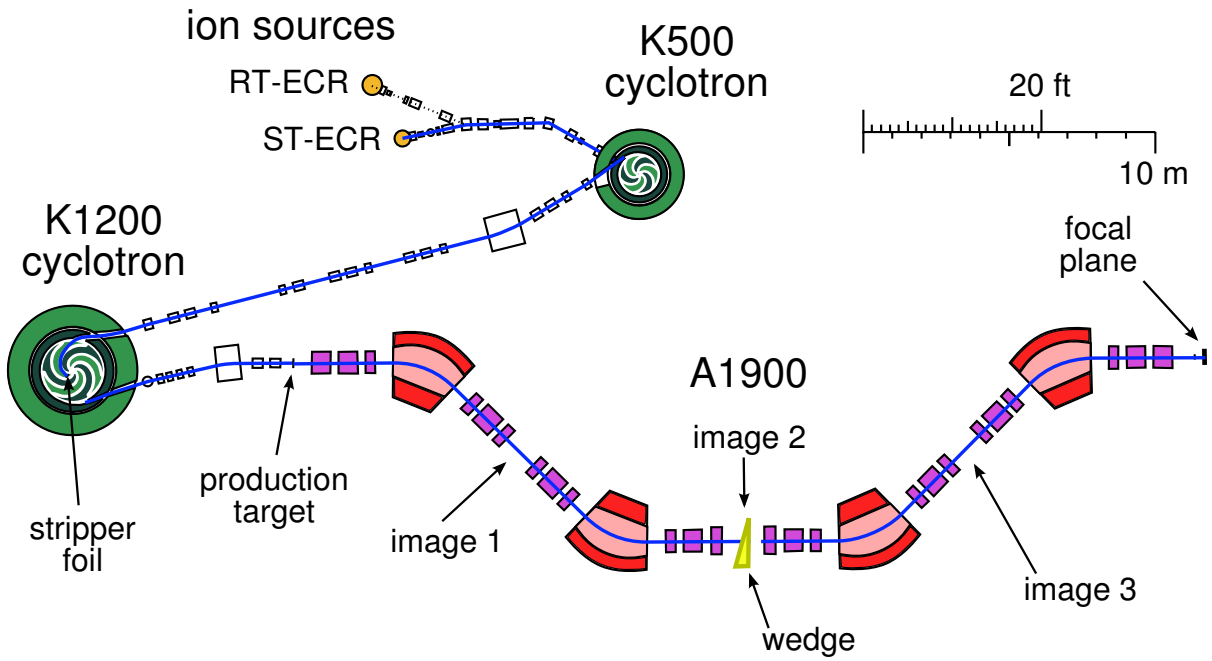

Figure 3.1: Layout of the NSCL Coupled Cyclotron Facility. Figure is modified from [48].

Electrons are accelerated by microwaves tuned to the electron cyclotron frequency ω_c:

$$\omega_c = \frac{eB}{m_e}, \tag{3.1}$$

where e and m_e are the electron charge and mass, respectively, and B is the magnetic field inside the cavity. The accelerated electrons collide with the atoms, stripping them of electrons. Once ionized, the ions are extracted by an applied voltage. The primary beam for this experiment was ^{76}Ge ionized in ARTEMIS to a charge state of $^{76}Ge^{+12}$.

Due to the Lorentz force law, charged particles moving perpendicular to a magnetic field will move in a circle of radius ρ:

$$\rho = \frac{p}{Bq} = \frac{\gamma m v}{Bq}, \tag{3.2}$$

where p is the momentum, γ is the relativistic factor, m is the mass of the particle, B is the magnetic field strength, and q is the charge of the particle. Cyclotrons take advantage of this

fact by using a strong magnetic field and three pairs of blade shaped "dees", which produce a radio-frequency electric field that accelerates the ions in the gaps between the dees, while the trajectory is confined by the magnetic field. Ions are injected into the center of the cyclotron, and each time an ion passes a gap, it is accelerated. As it gains energy, the magnetic field is no longer strong enough to confine the ion to a circle and it spirals outward toward the edge of the cyclotron. Once the ion reaches its maximum energy in the K500, it is extracted by a port on the outer edge of the cyclotron and transported via a coupling beamline to the K1200 cyclotron where the process is started again. There is a thin carbon foil, known as a *stripper foil*, at the entrance port of the K1200 that strips more, if not all, electrons off the ions. At extraction from the K500, the primary beam was 11.59 MeV/nucleon $^{76}Ge^{+12}$ and at extraction of the K1200 it was 130 MeV/nucleon $^{76}Ge^{30+}$.

The production of the radioactive beam from a stable one is accomplished via *projectile fragmentation*, in which the stable beam is collided with a stationary target, usually beryllium. The fragmentation can be described as a two step process, where first some number of nucleons are violently removed from the nucleus, creating a highly excited *prefragment*. The prefragment then decays by statistical nucleon emission, resulting in a wide range of stable and radioactive nuclei [53]. For the Coulomb excitation of ^{58,60,62}Cr, a 423-mg/cm^2 Be production target was used. Most of the nuclei produced are not the desired nuclei and need to be filtered out before an experiment can be done, this is accomplished with the A1900 fragment separator.

The A1900 [48, 54] analyzes and separates the reaction products and delivers them to the experimental area. The A1900 achieves isotopic separation via a three-step $B\rho$-ΔE-$B\rho$

technique. The key quantity, $B\rho$, or *magnetic rigidity* is found by rearranging Eqution 3.2:

$$B\rho = \frac{\gamma m v}{q}. \tag{3.3}$$

According to Equation 3.3, a dipole magnet with a given radius and magnetic field will only allow particles with a certain range of momentum-to-charge ratio to pass through. Other particles will either be deflected too much or two little and run into either side of the magnet exit bore. Particles with similar p/q ratios will all make it through selection, necessitating further purification. The remaining reaction products will be dispersed in space, according to their p/q ratio. Several pairs of slits located at the image points and focal plane of the A1900 can be partially closed on the beam, eliminating some of the contaminants and allowing a certain percentage of the momentum distribution of the beam through. The slits are partially opened or closed, depending on the needs of the experiment. The beam is then passed through an achromatic wedge, (which is not actually a wedge, but a curved aluminium foil [55]), where the particles lose energy according to the *Bethe formula* [56]:

$$-\frac{\mathrm{d}E}{\mathrm{d}x} = \frac{4\pi e^4 Z_\mathrm{p}^2}{m_0 v^2} N Z_\mathrm{t} \left[\ln \frac{2 m_0 v^2}{I} - \ln\left(1 - \frac{v^2}{c^2}\right) - \frac{v^2}{c^2} \right]. \tag{3.4}$$

$\mathrm{d}E/\mathrm{d}x$ is the energy loss per differential path length, e is the charge unit, Z_p and Z_t are the atomic number of the projectile and the degrader, respectively, v is the velocity of the projectile, m_0 is the electron rest mass, N is the number density of atoms in the degrader, and I is the average excitation energy of the stopping material, which is usually determined experimentally. As can be seen from Equation 3.4, the energy loss will be proportional to Z_p^2, so different elements in the beam will lose different amounts of energy in the wedge. After

the wedge, the particles are $B\rho$ selected again and delivered to the experimental setup. For the Coulomb excitation of ^{58,60,62}Cr, the wedge was 300-mg/cm^2 Al, and the momentum acceptance of the separator was set to 0.5% for ^{58}Cr and 3%for ^{60,62}Cr. Three different settings of the A1900 were used to deliver cocktail beams containing ^{58,60,62}Cr to the target position of the S800 at mid-target energies of 81.1, 81.7, and 79.0 MeV/nucleon for ^{58,60,62}Cr, respectively. The targets used to induce Coulomb excitation were placed at the target position of the S800 and were 252-mg/cm^2 ^{197}Au for ^{58,60}Cr and 238.4-mg/cm^2 ^{209}Bi for ^{62}Cr.

3.2 The S800 Spectrograph

After passing through the A1900 and transfer hall, the secondary beam enters the S800 spectrograph beam line [57, 58]. The S800 is a high-resolution, large-acceptance device designed for analyzing projectile-like residues from reactions induced at the target position of the spectrograph. The S800 consists of two sections (Figure 3.2), the analysis line and the spectrograph itself. The analysis line transports the beam from the A1900 focal plane, through the object scintillator and to the S800 target position via a series of magnets - four dipoles, five sets of quadrupole triplets, one quadrupole doublet and four sextupoles [59]. At the S800 entrance, a quadrupole focuses the beam before being directed to the focal plane using two large dipole magnets.

The analysis line has two complementary modes of operation, *focused mode* and *dispersion matched mode*. When operated in dispersion matched mode, a momentum resolution of 0.02% (for a 1 mm beamspot) can be achieved, albeit at the expense of a maximum momentum acceptance of only $\pm$0.25% for a typically sized target. Dispersion matching is achieved by tuning the analysis line achromatically so that the momentum spread in the beam at the object

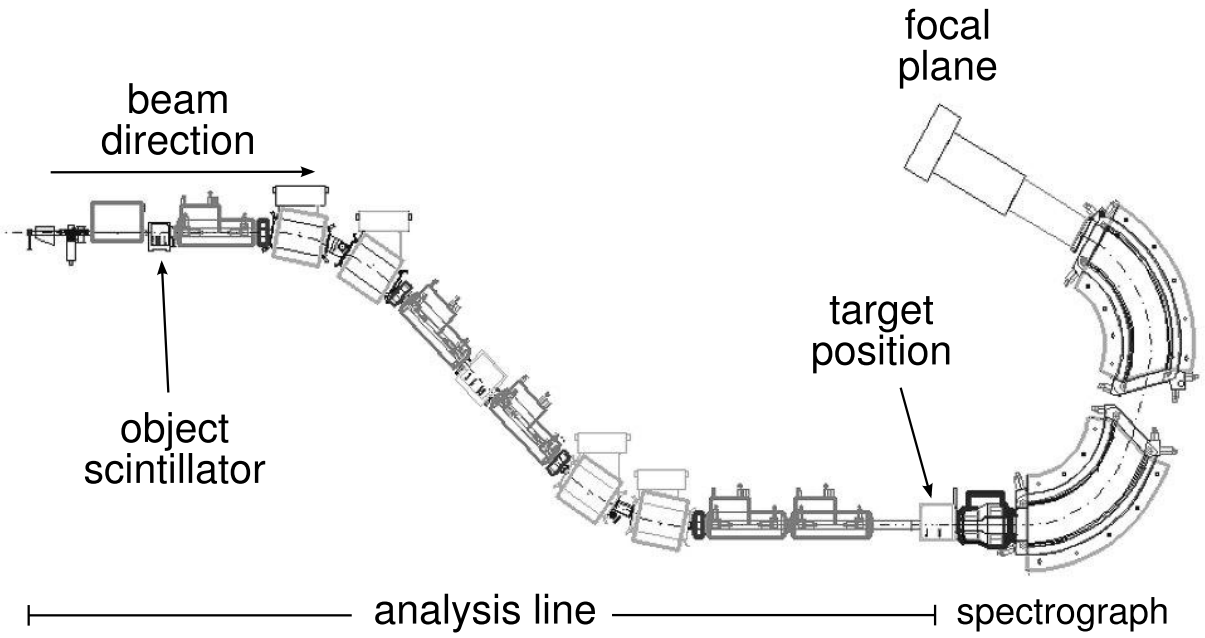

Figure 3.2: The S800 spectrograph. The location of the object scintillator, the target position, and the focal plane are identified. The target was surrounded by the γ-ray detection system SeGA.

is cancelled at the focal plane. This means, however, that the beam is momentum-dispersed at the target position (11 cm/%).

In focus mode, the beam is focused on the target and dispersed in the focal plane. The maximum momentum acceptance in focus mode is increased to $\pm 2\%$ at the expense of the momentum resolution being limited to the intrinsic momentum spread of the beam. The Coulomb-excitation measurements of ^{58,60,62}Cr were performed in focused mode.

3.2.1 Particle Detection Systems in the S800

The object scintillator (OBJ) is a thin plastic scintillator at the start of the analysis line. The 125 μm thick plastic scintillator is coupled to a photomultiplier tube to detect the florescence light generated by the beam particles passing through the film. The OBJ scintillator provides a timing signal used to determine the time-of-flight of each particle passing through the S800.

The S800 focal plane contains a suite of detectors used to characterize incoming particles [60, 58]. As shown in Figure 3.3, the first detectors encountered by a particle entering the focal plane are a pair of position-sensitive cathode-readout drift counters (CRDCs) spaced 1 m apart. These are used to determine the xy-position of each particle as it enters the focal plane. This information is used to reconstruct the trajectory of each particle through the spectrograph. Next, the particle passes through an ionization chamber (ic) to determine their energy loss, ΔE, which is used for particle Z identification. Finally there is a 1 mm thick plastic scintillator, called the E1 scintillator, used for timing information and triggering of the data acquisition. The difference between the E1 scintillator and the object scintillator times is the time of flight of the particle through the S800 beamlines (a measure of their velocity), which is used in conjunction with the ionization chamber energy loss for complete A and Z information.

The CRDCs have an active area of 59 cm in the dispersive direction and 26 cm in the non-dispersive direction and are 1.5 cm deep filled with 50 Torr of 80% CF_4 and 20% isobutane (C_4H_{10}) [58]. A voltage is applied to the CRDC in the dispersive direction. As particles pass through the CRDCs, molecules in the gas are ionized and the electrons drift toward the Frisch grid and anode wire where they are multiplied and collected on the anode. Bordering the anode wire are 224 cathode pads where the induced signal from the anode wire is measured. The center of gravity of the induced charge distribution on the pads is taken as the interaction point of the particle in the non-dispersive direction (x direction) in the CRDC. The position in the dispersive direction is determined by the drift time of the electrons via the time difference between the electron collection on the anode wire and the signal from the E1 scintillator. The $x - y$ coordinates in each CRDC are then combined to calculate the angle of the reaction residue as it entered the focal plane (Equation 4.4).

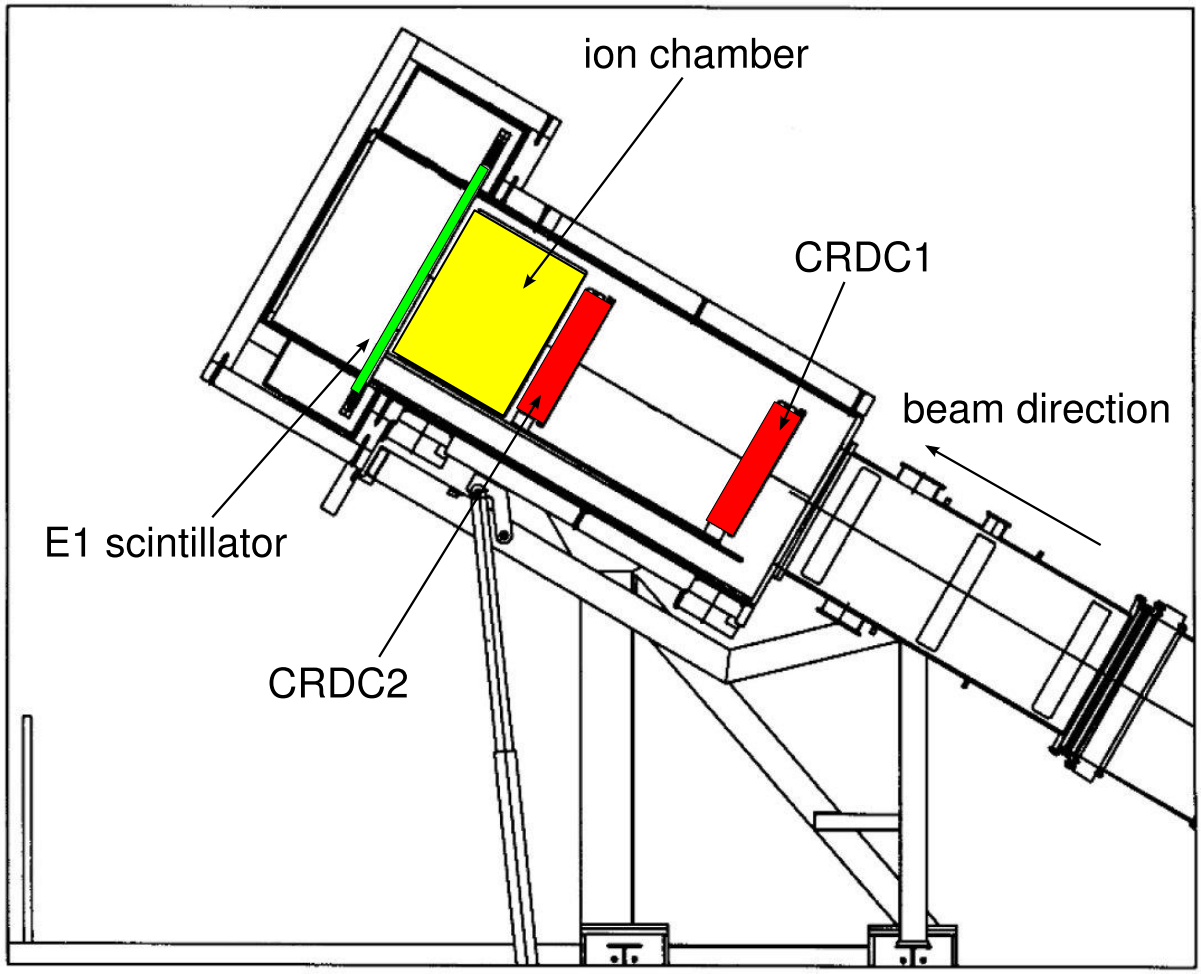

Figure 3.3: Diagram of the S800 focal plane with the CRDCs, ionization chamber, and E1 scintillator highlighted.

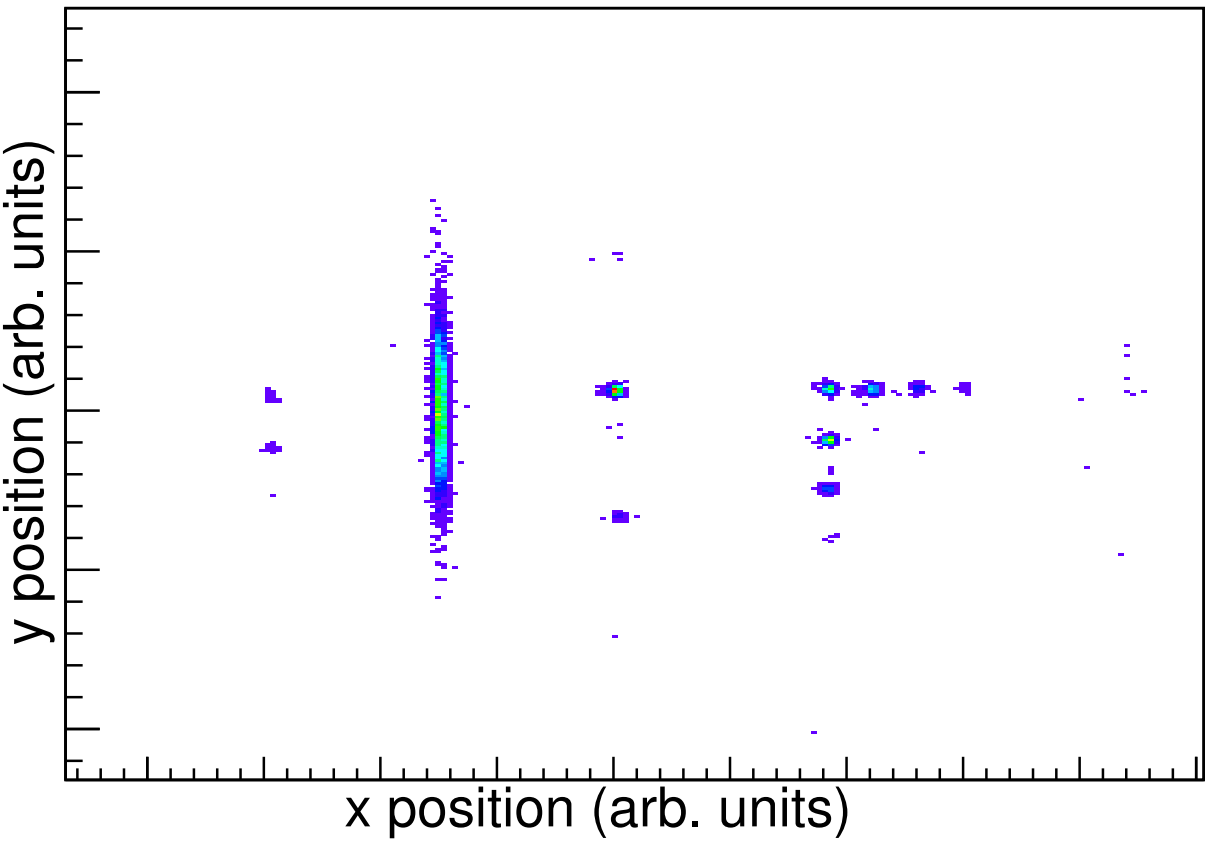

Figure 3.4: A typical CRDC mask calibration run of the $x - y$ positions of CRDC1. The areas of high intensity correspond to where holes and slits are drilled in the mask, allowing particles to pass through the CRDC and trigger the data acquisition.

The drift time of the electrons in the CRDCs depends on the position of the interaction, the specific properties of the fill gas, and the drift voltage applied and therefore needs to be calibrated. For the purpose of this calibration, a mask can be inserted in front of each CRDC. The mask has holes drilled at known locations, allowing the drift times to be converted to positions via a linear calibration. A typical CRDC mask run is shown in Figure 3.4.

Tracking of the particle's trajectory through the spectrograph is done by an inverse map of the spectrograph's magnetic field. The ion optics code COSY infinity [61] is used to calculate the inverse map based on the measured field profile [57]. The dispersive and non-dispersive positions and angles of the particles entering the focal plane are transformed into the dispersive and non-dispersive angles, position in the non-dispersive direction, and

fractional difference between the energy of the tracked particle and the energy of a particle on the central path through the spectrograph. The tracking can be summarized as follows [57]:

$$(a_{\mathrm{ta}}, y_{\mathrm{ta}}, b_{\mathrm{ta}}, d_{\mathrm{ta}}) = S^{-1}\left(x_{\mathrm{fp}}, a_{\mathrm{fp}}, y_{\mathrm{fp}}, b_{\mathrm{fp}}\right), \tag{3.5}$$

where S^{-1} is the inverse map, x, y, a, b and d stand for dispersive position, non-dispersive position, dispersive angle, non-dispersive angle, and fractional energy deviation from the central ray, respectively ($d_{\mathrm{ta}} = (E - E_0)/E_0$), where E is the energy of the tracked particle, and E_0 is the energy of a particle following the central path through the spectrograph). The subscripts *fp* and *ta* stand for focal plane and target, respectively. The scattering angle, θ, of the particle as it leaves the target, which is needed to ensure a safe scattering angle for Coulomb excitation, can be calculated from a_{ta} and b_{ta} using Equation 4.5.

The ionization chamber (ic) is filled with P10 gas and has 16 1-inch anode segments for measuring the energy loss of each particle. As the particles traverse the chamber, the fill gas is ionized and the electrons drift toward the anode. The energy lost by the particle in the gas goes as Z^2, according to Equation 3.4, making the energy loss ΔE useful for element identification in the absence of charge states where $Q \neq Z$ (not present in this work).

The E1 scintillator is a plastic scintillator behind the ionization chamber and is used for timing measurements. The time difference between the object scintillator and E1 times is the time-of-flight through the S800 and is used as part of the particle identification. The time difference between E1 and the anode wire in the CRDCs is taken as the drift time of the electrons in the CRDC and is used to determine the x (dispersive) position in the CRDCs. The projectile passes through the CRDC, ionizing the fill gas. The electrons drift toward the anode due to the drift voltage while the projectile continues through the E1 scintillator,

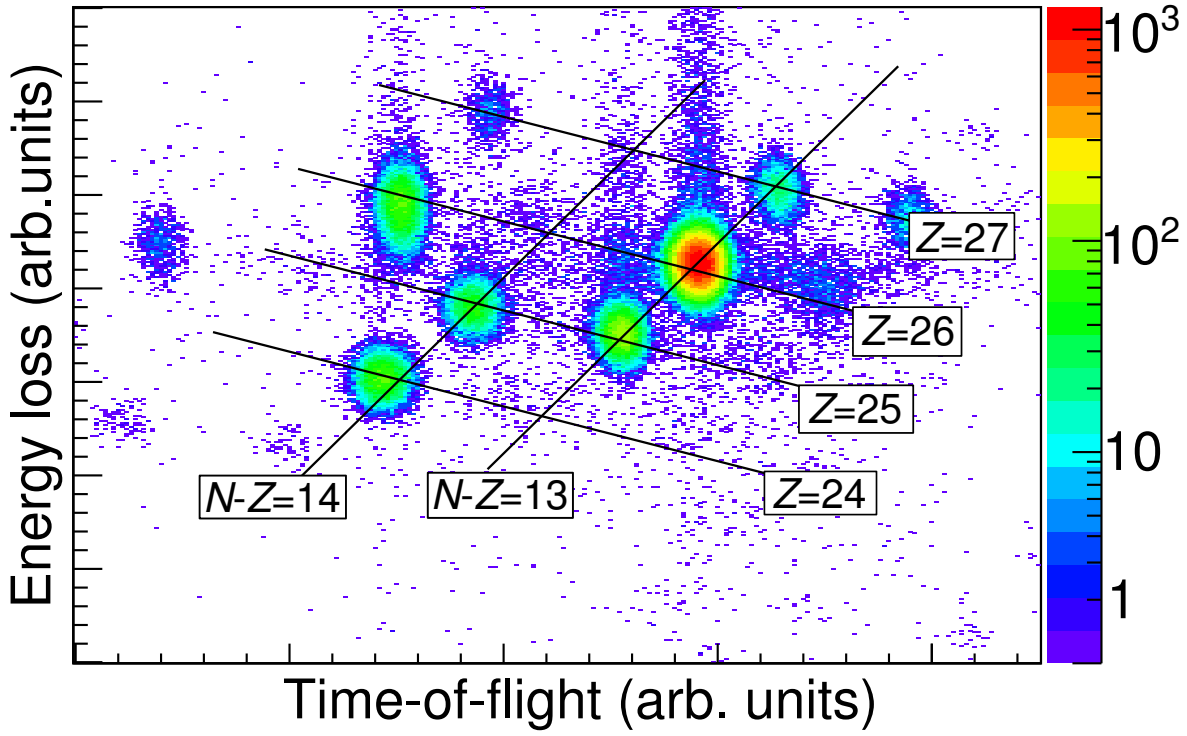

Figure 3.5: Example energy loss versus time-of-flight spectrum. The spectrograph was set to transmit the incoming beam after energy loss in the target (Coulomb-excitation setting). Energy loss is proportional to the square of the proton number and time-of-flight is proportional to the mass-to-charge ratio of the particles. Lines of constant Z and constant neutron excess $(N - Z)$ are drawn to guide the eye.

producing scintillation light. The time difference between the signals is the drift time of the electrons. The E1 signal also served as the common start and trigger for the data acquisition electronics.

Figure 3.5 shows an example particle identification spectrum. The vertical axis shows energy loss in the ionization chamber, which is proportional to the square of the nuclear charge (Z^2), and the horizontal axis shows the flight time of the particle between the OBJ and E1 scintillators, which is proportional to the mass-to-charge ratio of the projectile (m/q).

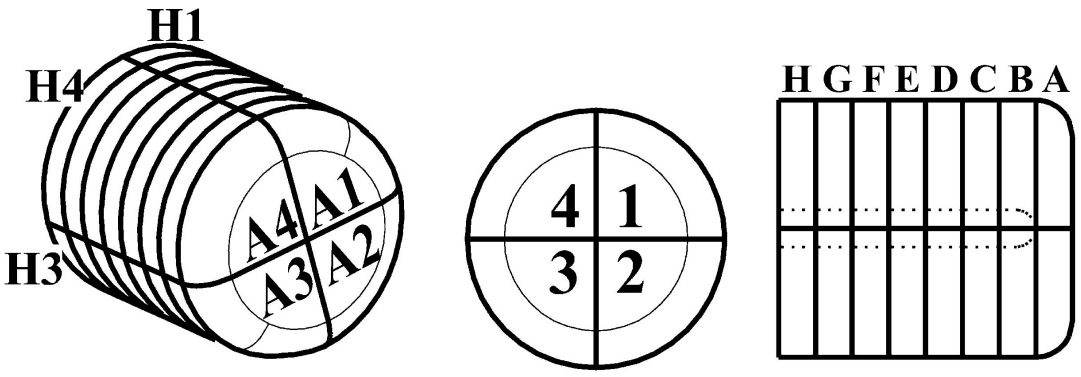

Figure 3.6: Angle, front and side views of a SeGA crystal, showing the segmentation. The dotted line in the side view shows the position of the central contact. Figure is from [62].

3.3 The Segmented Germanium Array SeGA

Surrounding the Coulomb-excitation target at the target position of the S800 was the Segmented Germanium Array SeGA [62]. SeGA is a γ-ray detection system comprised of up to 18 n-type, coaxial, high-purity germanium detectors which have been electrically segmented into quarters radially and eight slices perpendicular to the central axis. This segmentation geometry is shown in Figure 3.6. The crystals are 80 mm long and have a radius of 70 mm.

The configuration of SeGA used in this work is shown from the side in Figure 3.7. Seven of the detectors were arranged in a forward ring at an angle of 37° relative to the beam axis and the remaining ten formed the backward ring at 90°.

γ rays emitted from nuclei moving at a large fraction of the speed of light will be significantly *Doppler shifted* in energy when measured in the laboratory frame. The energy of the γ ray detected in the laboratory, $E_\gamma^{\rm lab}$, is related to the energy emitted in the rest frame of the nucleus $E_\gamma^{\rm cm}$ by

$$E_\gamma^{\rm lab} = \frac{E_\gamma^{\rm cm}\sqrt{1-\beta^2}}{(1-\beta\cos\theta)} = \frac{E_\gamma^{\rm cm}}{\gamma\,(1-\beta\cos\theta)}, \tag{3.6}$$

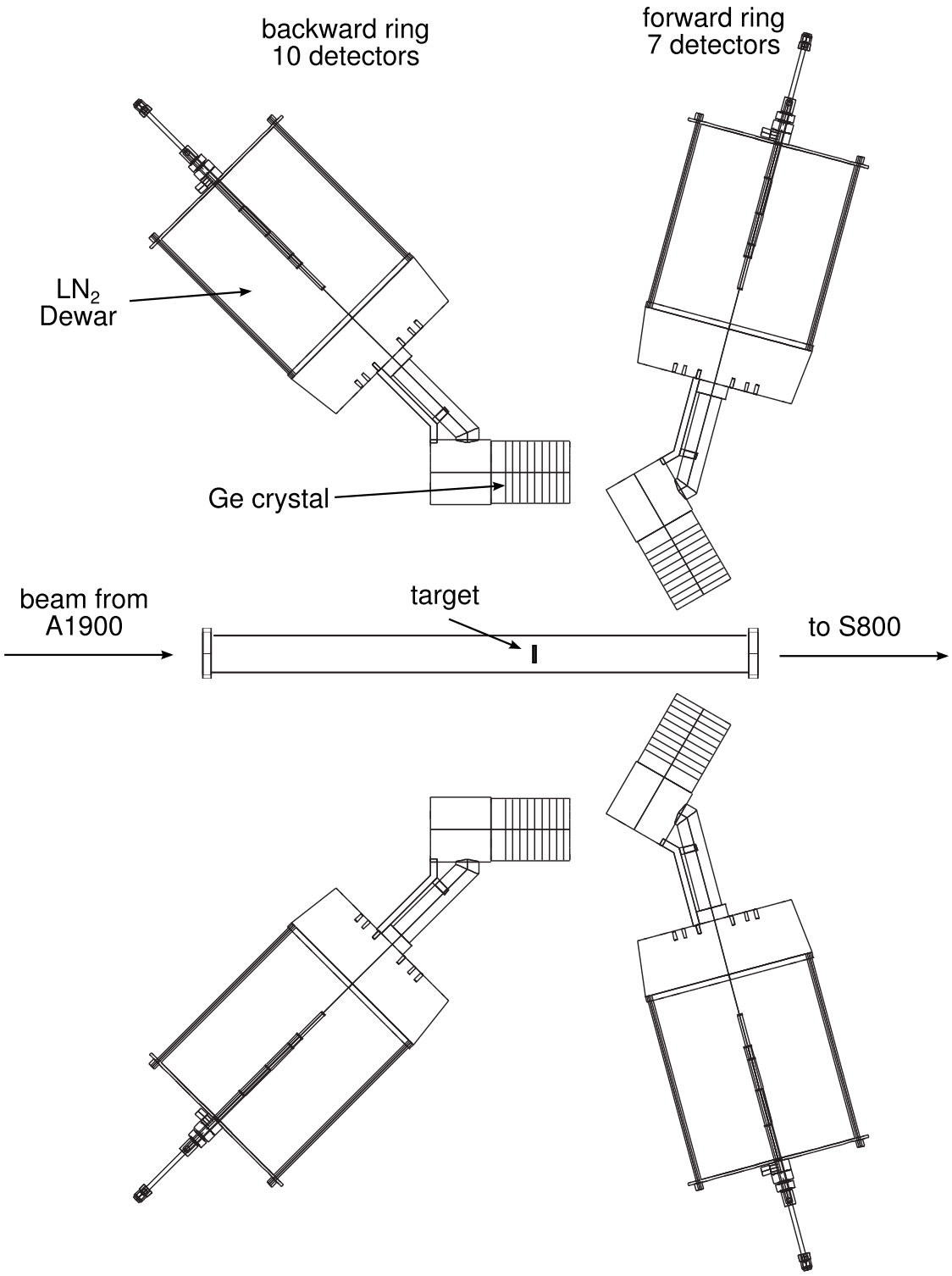

Figure 3.7: Diagram of a side view of SeGA showing the location of the target and the position of the rings surrounding it.

where $\beta = v/c$ is the velocity of the emitting nucleus, γ is the relativistic γ factor, and θ is the angle of emission of the γ ray with respect to the direction of travel of the nucleus. If the quantities β and θ are known, $E_\gamma^{\rm lab}$ can be *Doppler corrected* to obtain $E_\gamma^{\rm cm}$:

$$E_\gamma^{\rm cm} = E_\gamma^{\rm lab}\gamma(1 - \beta\cos\theta^{\rm lab}). \tag{3.7}$$

The energy resolution after Doppler-correction, $\Delta E_\gamma/E_\gamma$, is affected by three main factors: The uncertainty in the velocity, $\Delta\beta$, of the nucleus at the time of γ-ray emission due to its losing energy as it passes through the target, the uncertainty in θ due to the finite opening angle of the γ-ray detector, and uncertainty in the direction of travel of the scattered nucleus which emits the γ ray, $\Delta\theta$, and the intrinsic energy resolution of the detector $\Delta E_\gamma^{\rm intr}$, which is negligible for SeGA. The total energy resolution due to these factors can be written as [62]:

$$\left(\frac{\Delta E_\gamma^{\rm cm}}{E_\gamma^{\rm cm}}\right)^2 = \left(\frac{\beta\sin\theta}{1-\beta\cos\theta}\right)^2(\Delta\theta)^2 + \left(\frac{\beta-\cos\theta}{\left(1-\beta^2\right)(1-\beta\cos\theta)}\right)^2(\Delta\beta)^2 + \left(\frac{\Delta E_\gamma^{\rm intr}}{E_\gamma}\right)^2, \tag{3.8}$$

where all quantities on the right are in the lab frame. Figure 3.8 shows the contributions to the energy resolution due to the individual terms in Equation 3.8.

The segmentation of SeGA limits the uncertainty in the γ-ray emission angle and allows for event-by-event Doppler reconstruction of the γ-ray energy. The angle used in Doppler reconstruction is the angle of the segment, relative to the beam axis, which registers the highest energy deposit for each event. SeGA also takes advantage of the excellent intrinsic energy resolution of germanium, measured to be less than 0.2% FWHM at 1332 keV, rendering this contribution negligible [62]. This is especially good when compared to scintillator materials such as CsI(Na), where an intrinsic resolution of 6% FWHM is typical at 1332 keV [63].

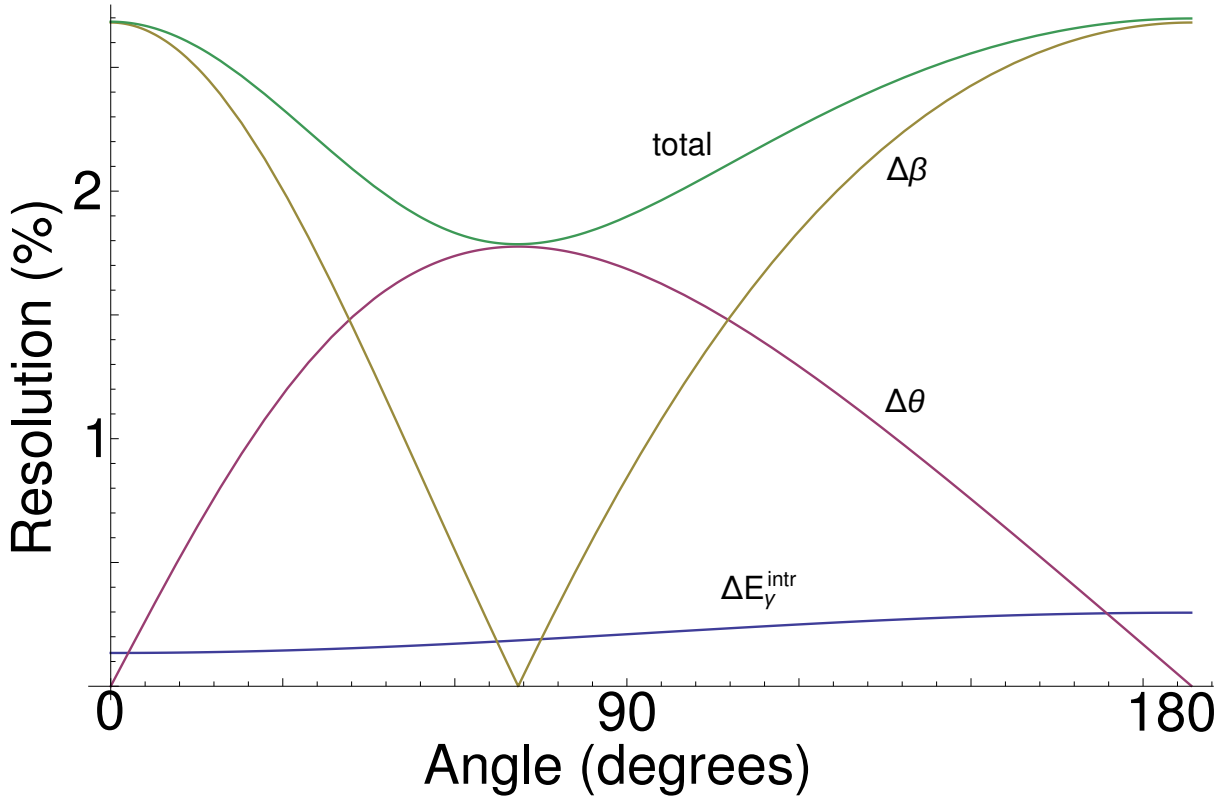

Figure 3.8: Contributions to the γ-ray energy resolution as a function of laboratory angle. For ^{62}Cr, $\beta = 0.377$, $\Delta\theta = 2.5$, $\Delta\beta = 0.23$, and $\Delta E_\gamma^{\rm intr}/E_\gamma = 0.002$. The contribution due to uncertainty in angle is labeled $\Delta\theta$, the contribution due to uncertainty in particle velocity is labeled $\Delta\beta$, and the contribution due to the intrinsic energy resolution is labeled $\Delta E_\gamma^{\rm intr}$. The curve labeled total is the three terms added in quadrature.

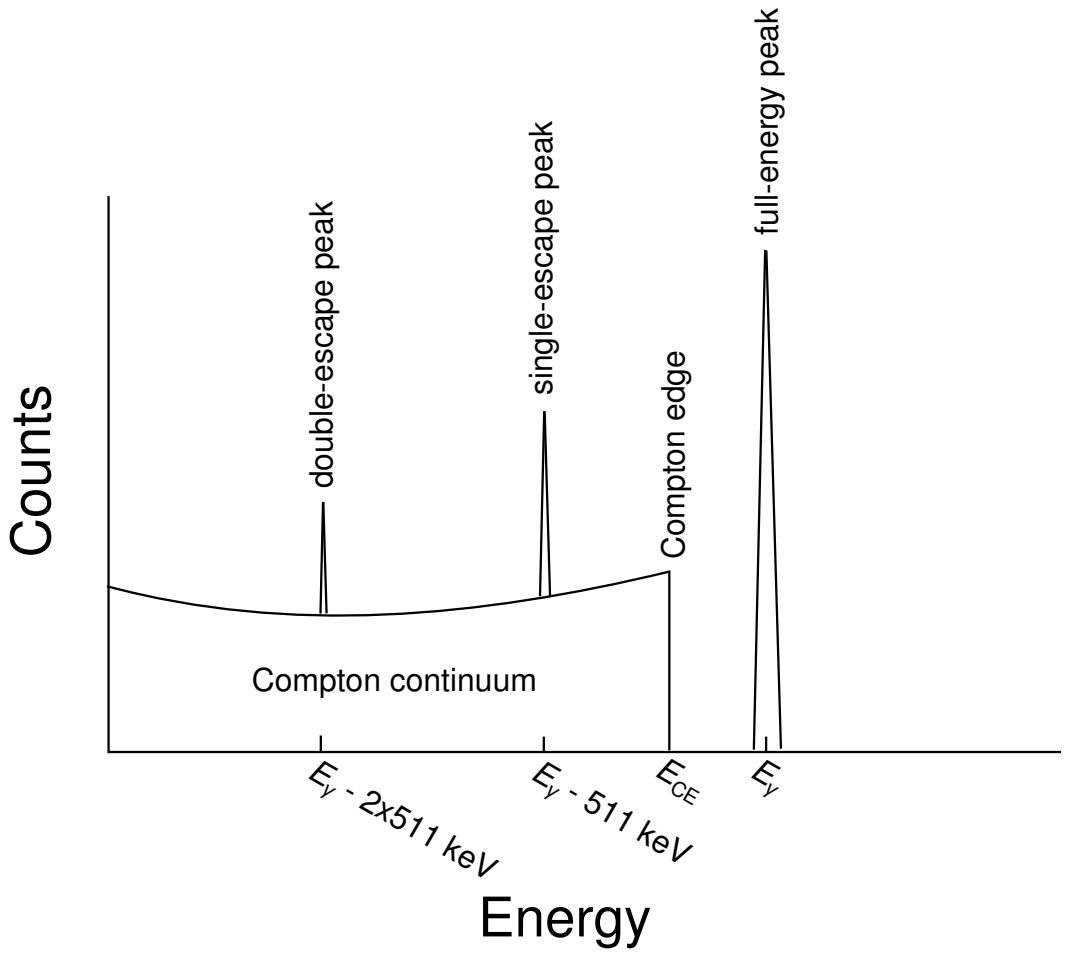

Figure 3.9: Example of a γ-ray detector response to many monoenergetic γ rays. The components of the spectrum are explained in the text

There are three primary ways γ rays interact with matter that are of interest in a γ-ray detector. These are the *photoelectric absorption*, *Compton scattering*, and *pair production*. In each case, the γ ray is converted into one or more energetic electrons which can be measured. In the case of semiconductor detectors, such as germanium, the electrons excite electron-hole pairs that are collected due to an applied drift voltage, producing a signal. Each process contributes to the shape of a γ-ray spectrum in a different way. An example of a detector response to monoenergetic γ rays interacting with the detector is shown in Figure 3.9. The various labeled components will be explained below.

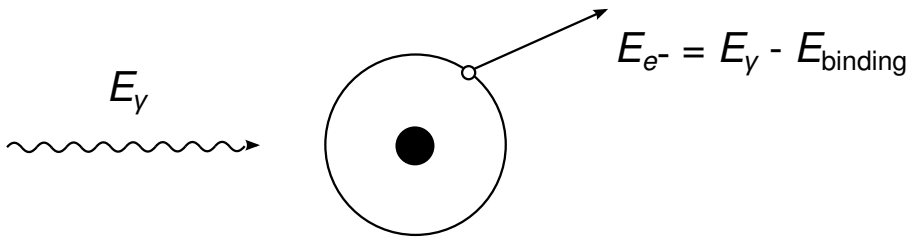

Figure 3.10: Schematic illustration of the photoelectric absorption process.

In photoelectric absorption, illustrated in Figure 3.10, the incoming γ ray is absorbed by an atom of the detector material and an electron is emitted. The energy of the electron is equal to the energy of the absorbed photon minus the binding energy of the electron, which is usually small compared to the photon energy. As long as the electron does not leave the detector volume, the full energy will be detected and this will contribute to the *full-energy peak*. This makes photoelectric absorption an ideal process for γ-ray detection because all the energy is transferred to a single electron. Because the probability for photoelectric absorption goes roughly as $Z^n/E_\gamma^{3.5}$, with n varying between 4 and 5, depending on the γ ray energy, it is desirable to use high-Z materials for γ-ray detection. Photoelectric absorption is the dominant process for γ-ray energies of a few-hundred keV and below [56].

In Compton scattering, illustrated in Figure 3.11, a γ ray of energy E_γ is scattered off of an electron of an absorber atom. Some of the γ-ray energy is transferred to the electron, and the γ ray is scattered by an angle, θ. The energy transferred to the electron depends on the scattering angle and is given by the Compton formula:

$$\frac{1}{E'_\gamma} - \frac{1}{E_\gamma} = \frac{(1 - \cos\theta)}{m_0 c^2}, \tag{3.9}$$

where m_0 is the electron mass. The angular distribution of Compton scattered γ rays is

governed by the *Klein-Nishina formula* for the the differential scattering cross section [56]:

$$\frac{\mathrm{d}\sigma}{\mathrm{d}\Omega} = r_0^2 Z \left(\frac{1}{1+\alpha\left(1-\cos\theta\right)}\right)^2 \left(\frac{1+\cos^2\theta}{2}\right) \left(1+\frac{\alpha^2\left(1-\cos\theta\right)^2}{\left(1+\cos^2\theta\right)\left[1+\alpha\left(1-\cos\theta\right)\right]}\right), \tag{3.10}$$

where $\alpha \equiv E_\gamma / m_0 c^2$ and r_0 is the classical electron radius. The scattered γ ray can either leave the detector or continue to interact through multiple Compton scatterings until it undergoes photoelectric absorption. Since the γ ray can scatter through any angle from 0-180°, the electron can be imparted with any energy on a continuum from 0 to the maximum allowed. The maximum allowed energy transfer occurs when the γ ray scatters by 180°. This is the maximum energy transferable in a single Compton scattering event and is given by:

$$E_{\mathrm{CE}} = \frac{2E_\gamma^2}{m_0 c^2 + 2E_\gamma}, \tag{3.11}$$

where E_{CE} is the energy of the *Compton edge*. The energy between 0 and E_{CE} is known as the *Compton continuum* or *Compton plateau*. γ rays leaving the detector after Compton scattering will contribute to the Compton plateau, while γ rays undergoing photoelectric absorption after one or more Compton scatters will contribute to the full-energy peak. Compton scattering is the most probable interaction for a γ ray with an energy between hundreds of kev and a few MeV, the most common region of interest for nuclear physics, and the probability increases linearly with Z and decreases gradually with γ-ray energy [56].

For γ rays with energy greater than twice the rest mass of the electron, ($2m_0c^2$=1.022 MeV), pair production can occur in the presence of a nucleus. In pair production, illustrated in Figure 3.12, a γ ray is converted into an electron-positron pair, and the remaining γ-ray energy (above 1.022 MeV) becomes kinetic energy shared by the electron-positron pair; *i.e.*,

Figure 3.11: Schematic illustration of the Compton-scattering process.

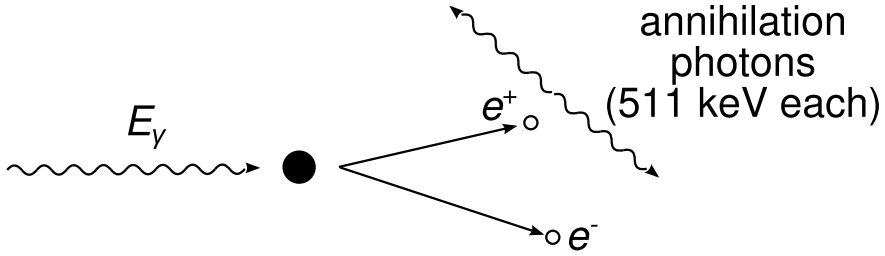

Figure 3.12: Schematic illustration of the pair production process.

$E_{e-} + E_{e+} = E_\gamma - 2m_0c^2$. Following pair production, the electron is detected, and the positron will eventually encounter an electron and annihilate, producing two *annihilation photons* of energy $m_0c^2 = 511$ keV each. The annihilation photons can then undergo photoelectric absorption, leave the detector, or Compton scatter. In the case where both annihilation photons are absorbed, the full energy of the γ ray is detected. If one of the annihilation photons leave the detector, while the other is absorbed, the energy detected will be $E_\gamma - m_0c^2 = E_\gamma - 511$ keV. This will lead to a *single-escape peak* in the γ-ray spectrum. If both annihilation photons leave the detector, the result will be an energy of $E_\gamma - 2m_0c^2 = E_\gamma - 1.022$ MeV recorded. This will result in a *double-escape peak* in the γ-ray spectrum. Pair production is only possible for γ-ray energies above 1.022 MeV, and is not the dominant interaction until the γ-ray energy approaches several MeV. The probability of pair production increases approximately as Z^2 of the absorber and increases strongly with γ-ray energy [56].

Chapter 4

Intermediate-energy Coulomb Excitation of ^{58,60,62}Cr

Nuclear shell structure is well-established for stable nuclei. Beyond the valley of β stability, some of the canonical magic numbers disappear and new ones emerge [13, 65]. Spin-isospin parts of the NN interaction, in particular the monopole components of the proton-neutron tensor force, have been identified as robust driving forces for shell evolution in exotic systems [39, 38, 66]. The chain of nuclei with neutron number $N = 40$, a harmonic-oscillator magic number and possibly sub-shell gap, is particularly interesting. Along this isotonic line, the $N = Z = 40$ nucleus ^{80}Zr is highly deformed with a quadrupole deformation parameter of $\beta_2 \approx 0.4$ [35]. On the neutron-rich end of this line, ^{68}Ni has its first 2^+ state near 2 MeV and a small $B(E2; 0^+ \rightarrow 2^+)$ transition probability [36], with a highly deformed proton intruder 0^+ state predicted at about 2.2 MeV [67].

Only two and four protons away from ^{68}Ni, the first 2^+ states of ^{66}Fe and ^{64}Cr are low-lying in energy with evidence for collectivity [68, 69]. A variety of complementary experimental studies have elucidated the influence of the $N = 40$ energy gap on the structure of ^{68}Ni [36, 70, 71, 72, 73], with theoretical models suggesting that below $Z = 28$ the decreased occupation of the $\pi 0f_{7/2}$ orbital leads to an onset of collectivity and deformation

Excerpts and figures reprinted from [64].

[36, 74, 75, 40].

These structural changes are strongly influenced by the $\nu 0g_{9/2}$ and $\nu 1d_{5/2}$ neutron orbitals [40, 74]. The proton-neutron tensor force between the $\pi 0f_{7/2}$ and $\nu 0f_{5/2}$ orbitals is attractive and strongest when both are fully occupied [38], as is the case for ^{68}Ni. This attraction draws the $\nu 0f_{5/2}$ orbital down in energy, creating an $N = 40$ gap of about 3 MeV [40]. Moving to Fe ($Z = 26$) and Cr ($Z = 24$) progressively weakens the monopole parts of the proton-neutron tensor interaction and shrinks the $N = 40$ gap by about 1 MeV, while the quadrupole-correlated ($\Delta\ell = 2$) $0g_{9/2}$ and $1d_{5/2}$ orbitals become nearly degenerate, enhancing the probability of their occupation by neutrons [40].

Recent excited-state lifetime measurements on neutron-rich Fe isotopes have quantified the increased collectivity in ^{64,66}Fe [76, 77] through the extracted $B(E2; 0^+ \rightarrow 2^+)$ values. The chain of Cr isotopes displays a particularly rich picture of shell evolution: Stable ^{52}Cr exhibits the expected signatures of the $N = 28$ neutron shell closure, while four neutrons heavier, ^{56}Cr reveals the presence of a new sub-shell gap at $N = 32$ [33], generated by the same robust driving force that is behind the onset of collectivity toward $N = 40$ [39]. Adding more neutrons leads to strongly increasing collectivity, with experimental evidence coming from decreasing 2_1^+ energies out to $N = 40$ [69], increasing $B(E2)$ values out to $N = 34$ [78], and increasing deformation parameters out to $N = 38$ [79] as well as the presence of rotational bands at higher spin in $^{55-59}$Cr [80, 81, 82]. The intermediate-energy Coulomb excitation measurements of ^{58,60,62}Cr reported here quantify the onset of collectivity with N in neutron-rich Cr nuclei with extracted $B(E2; 0^+ \rightarrow 2^+)$ values. They also benchmark the latest nuclear models in this region of rapid structural change. The experimental setup is described in Chapter and the Coulomb-excitation technique is described in Chapter .

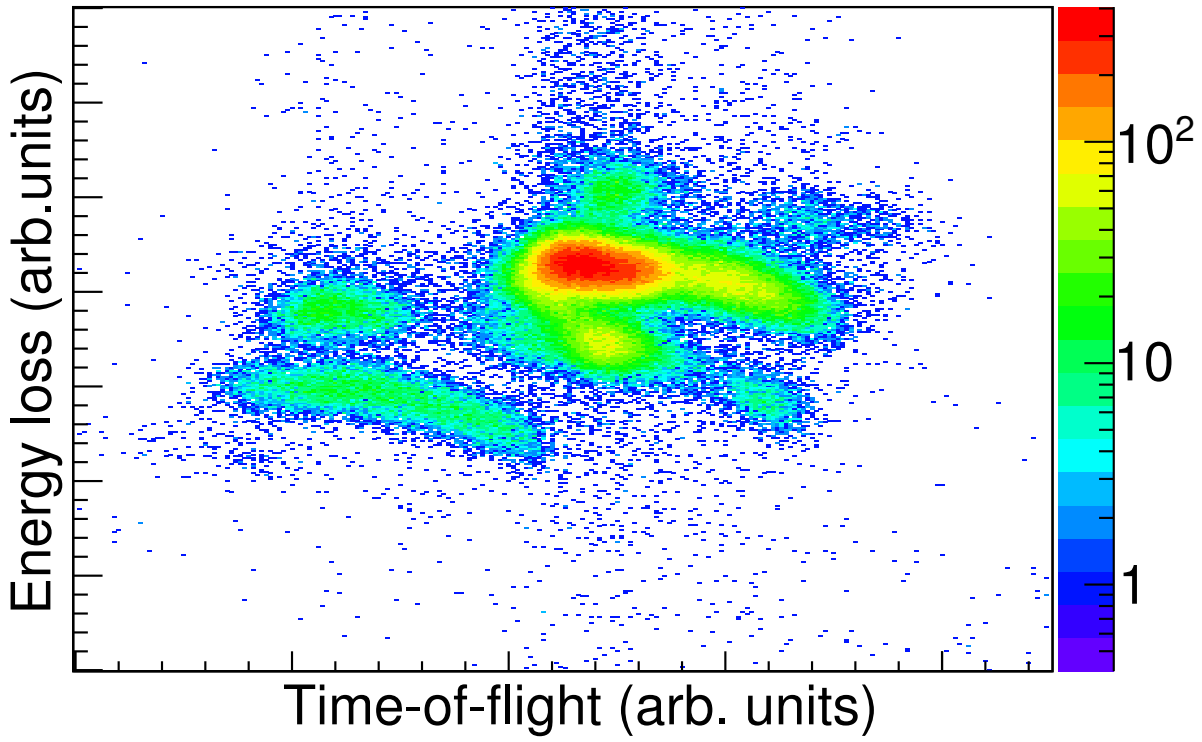

Figure 4.1: Particle-identification matrix for the ^{62}Cr setting before any corrections were performed.

4.1 Data Analysis

The data analysis utilized several software programs, NewSpecTcl [83, 84] was used for the main data sorting. Tv [85] was used for the energy and efficiency calibrations, and GEANT4 [86] and ROOT [87] were used for the simulations and final γ-ray analysis.

4.1.1 Particle Identification

Particle identification is achieved by plotting time-of-flight through the S800 beam line and spectrograph versus the energy lost in the S800 ionization chamber for each particle detected. Figure 4.1 shows this plot for the ^{62}Cr setting, before any trajectory corrections have been applied.

The time-of-flight (tof) through the S800 is the time difference between the object

scintillator (obj) and the E1 scintillator. The tof depends on the path taken by the particle, which depends on the particle's velocity and angle. Since the beam is not monoenergetic, different particles of the same species (A/Z) will take slightly different paths, resulting in different x positions and dispersive angles in the focal plane. This creates a correlation between both a_{fp} and obj and x_{fp} and obj. The corrected tof is denoted $obje1$ and is calculated as

$$obje1 = obj + a_x x_{\mathrm{fp}} + a_\theta a_{\mathrm{fp}}, \tag{4.1}$$

where a_x and a_θ are the correction coefficients for the dispersive position (x_{fp}) and dispersive angle (a_{fp}), respectively.

The ion-chamber data also needs several corrections. The 16 ion-chamber segments are gain matched with a linear calibration. A position correction is also needed to account for correlations between the energy loss in the ion chamber, ic_{sum}, and x_{fp} and y_{fp}. The corrected energy loss, ic_{de}, is

$$ic_{\mathrm{de}} = ic_{\mathrm{sum}}\left(1 + a_y y_{\mathrm{fp}}\right) \begin{cases} \mathrm{e}^{a_x\left(x_0 - x_{\mathrm{fp}}\right)} & x_{\mathrm{fp}} < x_0 \\ 1 & x_{\mathrm{fp}} \geq x_0 \end{cases} \tag{4.2}$$

where a_y, a_x and x_0 are the correction constants. Figure 4.2 shows the resulting particle identification after all corrections have been applied. The result is a drastic improvement in the ability to identify and separate the constituents of the beam.

4.1.2 Scattering Angle Reconstruction

An important aspect of intermediate-energy Coulomb excitation experiments is the measurement of the scattering angle of the scattered projectiles. The scattering angle measured in the

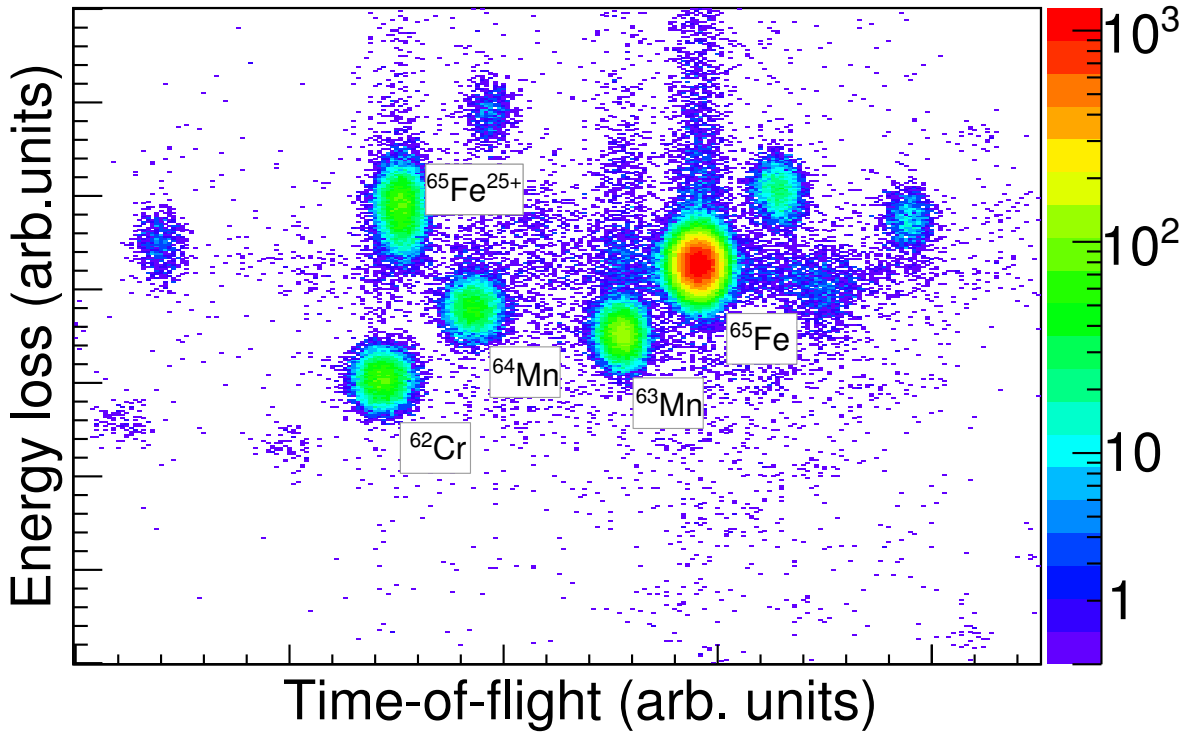

Figure 4.2: Particle-identification matrix for ^{62}Cr after corrections to the time-of-flight and ionization chamber have been applied. The strongest components are identified.

Setting	Purity (%)	$\Delta p/p$ (%)	Rate (pps)	Total Particles	Major Contaminants
^{58}Cr	80	0.5	3400	1×10^8	^{59}Mn, ^{57}V, ^{55}Ti
^{60}Cr	50	2.5	1400	7×10^7	^{62}Mn, ^{61}Mn, ^{63}Fe
^{62}Cr	10	2.5	66	3×10^7	^{65}Fe, ^{63}Mn, ^{64}Mn

Table 4.1: Approximate purities, average rates, total particles of interest after the running time, and major contaminants for each of the three settings used.

lab is the connection to the impact parameter of the collision, as shown in Figure 2.1, and is required to restrict the analysis to safe impact parameters. The dispersive and non-dispersive parts of the scattering angle, a_{fp} and b_{fp}, respectively, of each particle are calculated from the CRDC positions. The focal-plane angles are calculated as

$$\tan a_{\mathrm{fp}} = \left(\frac{\mathrm{CRDC2}_x - \mathrm{CRDC1}_x}{d} \right) \tag{4.3}$$

$$\tan b_{\mathrm{fp}} = \left(\frac{\mathrm{CRDC2}_y - \mathrm{CRDC1}_y}{d} \right) \tag{4.4}$$

where d is the distance between the CRDCs, 1.073 m. With the aid of the inverse map, the dispersive and non-dispersive scattering angles at the target, a_{ta} and b_{ta} are reconstructed. Figure 4.3 shows the distribution of non-dispersive angle (b_{ta}) versus dispersive angle (a_{ta}) for ^{62}Cr particles. The uncertainty in the scattering angle due to the position resolution of the CRDCs was assumed to be 2 mrad.

From a_{ta} and b_{ta} the scattering angle, θ, of each particle is calculated as

$$\sin\theta = \sqrt{\sin^2 a_{\mathrm{ta}} + \sin^2 b_{\mathrm{ta}}}. \tag{4.5}$$

Figure 4.4 shows the distribution of scattering angles for ^{62}Cr particles measured in this experiment. The azimuthal angle of the scattered particle is calculated from a_{ta} and b_{ta} as shown in Table 4.2, and the distribution for ^{62}Cr is shown in Figure 4.5.

The asymmetry seen in 4.5 is due to different angular emittances in the incoming beam in the dispersive and non-dispersive directions. The finite angular emittance smears out the scattering angle distribution. On average this will not lead to a significant net bias in the centroid of the scattering angle distribution but to a broadening around θ_{max}. Since we

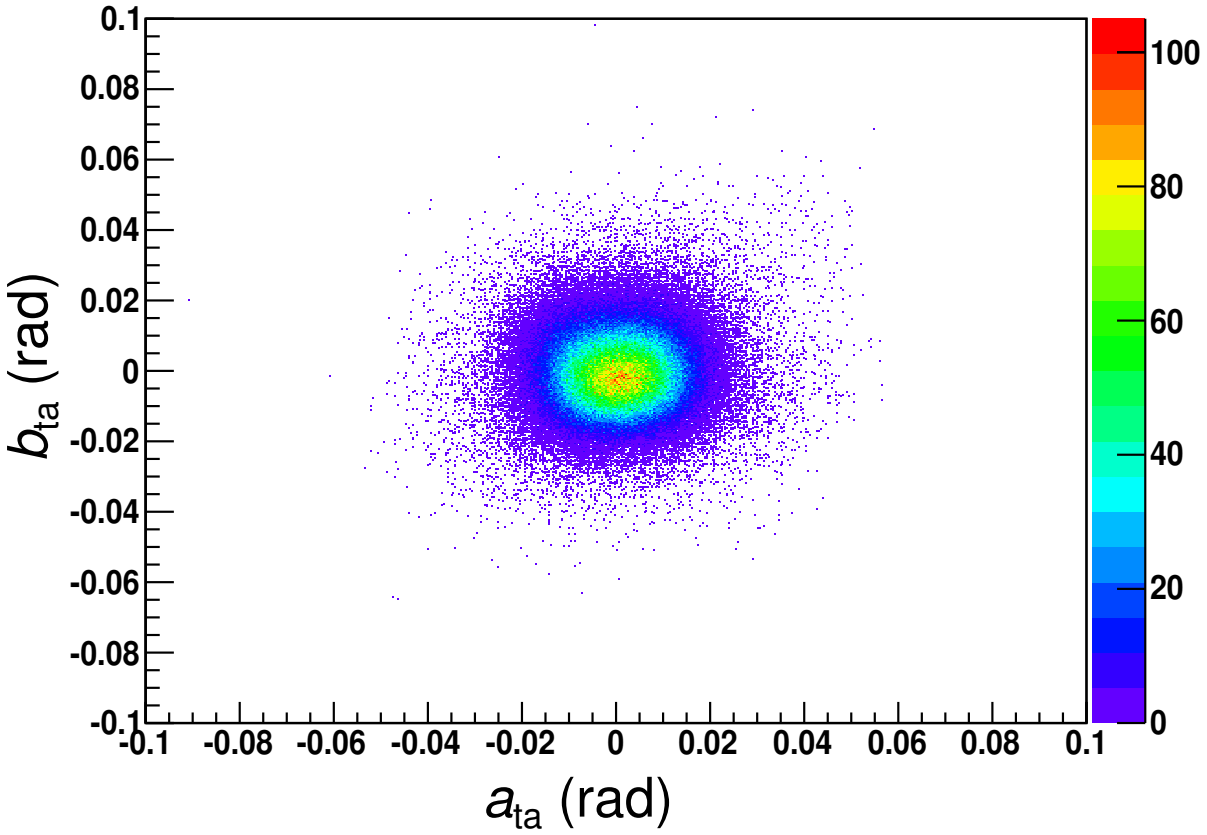

Figure 4.3: Non-dispersive (b_{ta}) versus dispersive (a_{ta}) angles of ^{62}Cr particles as they exit the target.

$\sin a_{\mathrm{ta}}$	$\sin b_{\mathrm{ta}}$	ϕ
> 0	> 0	$\arctan\left(\frac{\sin b_{\mathrm{ta}}}{\sin a_{\mathrm{ta}}}\right)$
< 0	> 0	$\pi - \arctan\left(\frac{\sin b_{\mathrm{ta}}}{\lvert\sin a_{\mathrm{ta}}\rvert}\right)$
< 0	< 0	$\pi + \arctan\left(\frac{\lvert\sin b_{\mathrm{ta}}\rvert}{\lvert\sin a_{\mathrm{ta}}\rvert}\right)$
> 0	< 0	$2\pi - \arctan\left(\frac{\lvert\sin b_{\mathrm{ta}}\rvert}{\sin a_{\mathrm{ta}}}\right)$

Table 4.2: The azimuthal angle ϕ is calculated as shown in the table.

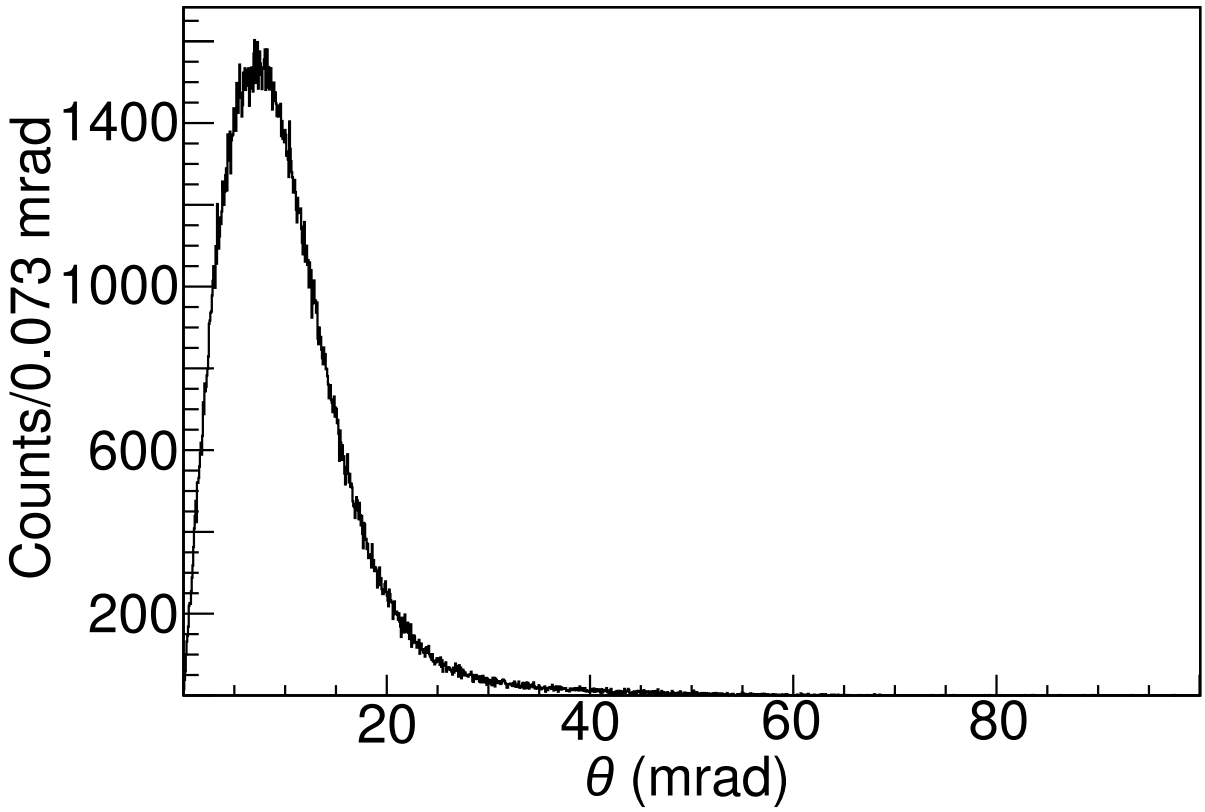

Figure 4.4: Distribution of scattering angles of ^{62}Cr particles, event-by-event reconstructed from the positions in the focal plane and the inverse map.

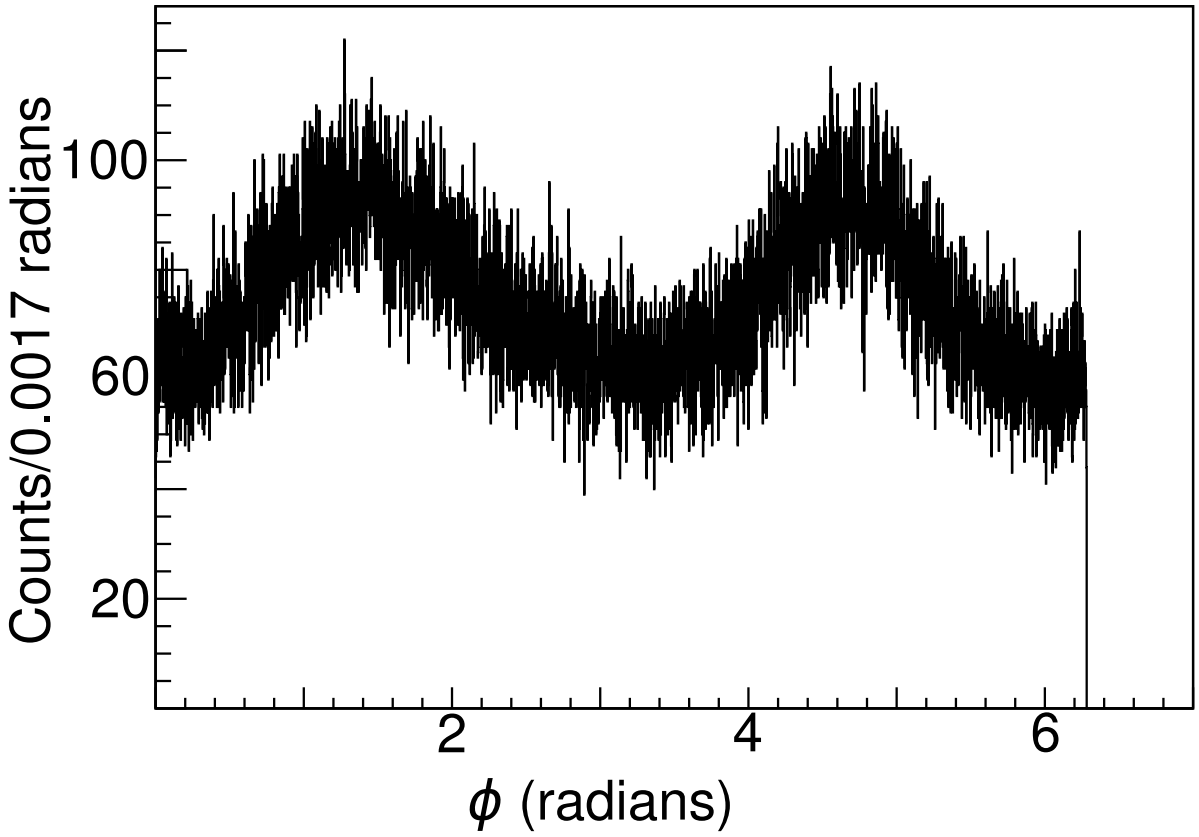

Figure 4.5: Distribution of azimuthal angles of scattered ^{62}Cr particles. The structure is due to different emittances of the beam in the dispersive and non-dispersive directions.

do not measure the details and shape of the angular distribution and only set a maximum scattering angle condition, the position of the centroid matters the most. Locally, the Coulomb-excitation cross section is essentially linear for the small range of angles being discussed (Figure 4.33), and only a small net bias might be introduced in the translation from angle-integrated cross section to $B(E2)$ value. The test cases used in this measurement - the Coulomb excitation of the gold target and the confirmation of the known ^{58}Cr $B(E2)$ value - confirm that the effect is not detectable within the experimental uncertainties. This experiment was the first where such large emittance effects were observed [88]. Subsequent experiments measure the effects of the angular emittance by comparing data measured with and without a target and the effects were determined to be small. Test cases are always used as a check on the setup and analysis, here the Coulomb excitation of the gold target and ^{58}Cr were the test cases that validated the analysis procedure. Tweaks of the optics introduced to optimize transmission are suspected to lead to the asymmetric beam emittance and future Coulomb excitation results will not use the modifications to the beam line tune and cope with reduced transmission.

4.1.3 SeGA Calibrations

γ-ray spectroscopy experiments rely on γ rays to identify and quantify the inelastic process. In order to correctly extract energies and cross sections from γ-ray spectra, the SeGA detectors must be calibrated. Energy calibrations assure that the peaks in the γ-ray spectrum are aligned and in the proper position, and efficiency calibrations are needed to determine the number of γ rays that will be detected for a given number of emitted γ rays.

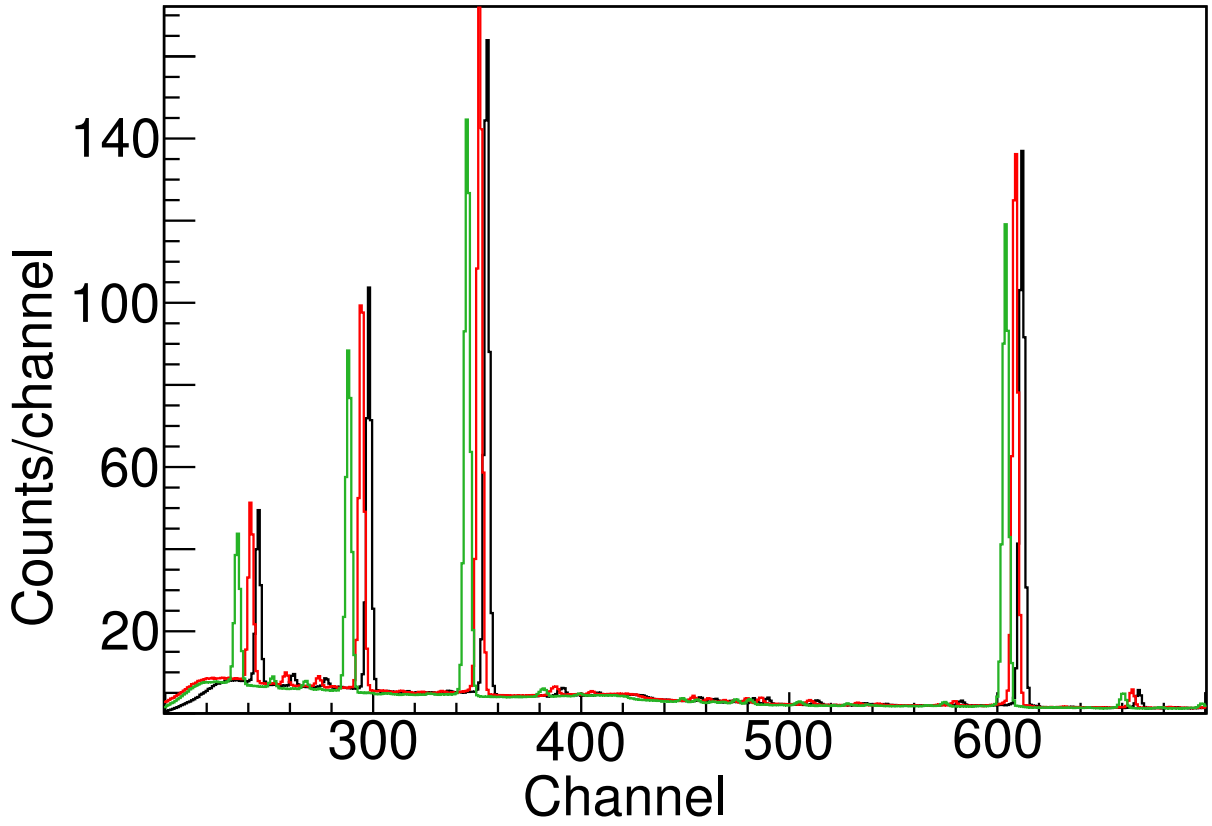

Figure 4.6: A portion of the response of three different SeGA detectors and electronics channels to a ^{226}Ra source. The detectors have not been calibrated and the full-energy peaks do not line up, demonstrating the need for an energy calibration. In the calibration process, the ADC channels are mapped to energies with the known ^{226}Ra calibration peaks.

4.1.3.1 Energy Calibration

Each SeGA detector and its signal processing chain will have a different response to a γ-ray of a given energy. The full-energy peak will be in a different ADC channel for each detector; therefore, each detector needs to be calibrated individually. A ^{226}Ra source was used to perform the energy calibration. ^{226}Ra has a half life of 1600 years and decays by a chain of α and β decays ending in stable ^{208}Pb, resulting in γ rays ranging in energy from 200 keV to 3 MeV. Figure 4.6 shows a portion of the response of three different SeGA detectors to a ^{226}Ra γ-ray source. The full-energy peaks are not aligned and are in ADC channels which must be associated with energies. The need for a calibration is apparent.

To perform the energy calibration, the peak positions of several prominent full-energy peaks were determined from the measured, uncalibrated spectrum from each detector. A fit was performed against the known energies of the γ-ray peaks from the ^{226}Ra source in order to determine the quadratic calibration for each detector. The calibration coefficients were chosen as to minimize the χ^2

$$\chi^2 = \sum_i \frac{\left(E_\gamma^{\text{meas}} - E_\gamma^{\text{known}}\right)^2}{\sigma^2}, \tag{4.6}$$

where E_γ^{meas} is the measured centroid of the γ-ray peak, E_γ^{known} is the known energy of the γ-ray transition, σ is the uncertainty in the measured peak position, and the sum runs over all peaks included in the fit.

Each segment of a SeGA detector gives its own energy signal in addition to the core. Since the angle of the segment registering the largest energy deposit is taken as the angle used for Doppler reconstruction, the segments need to be calibrated as well, although not as precisely as the core. Once the core calibration has been completed, the segment calibration can be done. To calibrate the segments, an algorithm selects events in which the entire energy of the interaction is recorded in a single segment. Since the core is calibrated, the energy recorded in the core is known and can be used to calibrate the segment that registered the event. This algorithm continues until enough calibration points are recorded to have an individual calibration for each segment [83].

4.1.3.2 Efficiency Calibration

In order to determine a cross section from an experiment, the efficiency of the detector system must be known. For SeGA, this is accomplished by using a γ-ray source of known activity

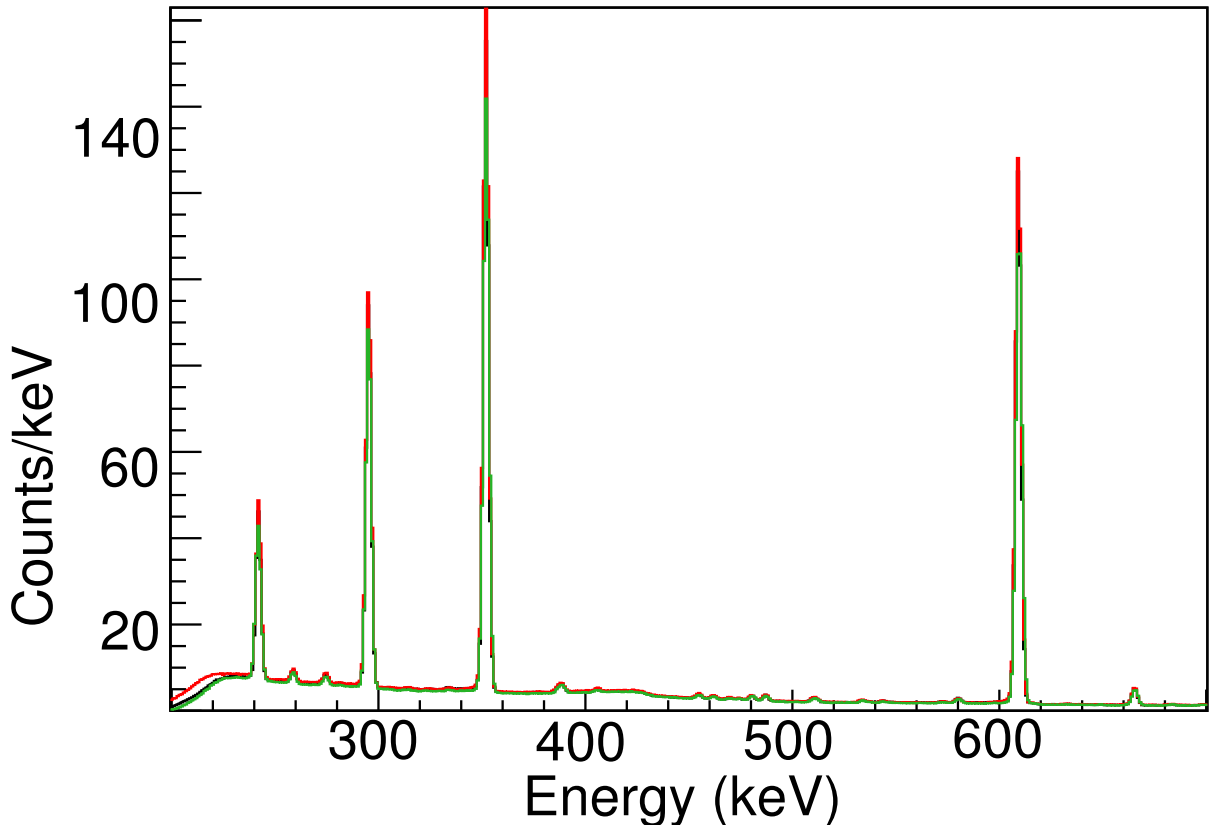

Figure 4.7: The same three detectors from Figure 4.6 after the energy calibration. The peaks now are aligned and have the correct ADC-channel to energy attribution.

to perform an efficiency calibration. In separate runs, ^{152}Eu and ^{226}Ra γ-ray sources were placed in the same position as the Coulomb-excitation target would be placed, in order to ensure the same detector solid angle for both the source and in-beam measurements. If the activity of the source and the emission probability of each γ-ray transition is known, the number of counts in the measured γ-ray spectrum, divided by the number of emitted γ rays and the live time of the data acquisition system, gives the detection efficiency of SeGA for that energy. The γ-ray *efficiency curve*, $\epsilon\left(E_\gamma\right)$, is obtained by fitting the measured efficiencies over a range of energies. The function used to describe the efficiency curve in this work was

$$\epsilon\left(E_\gamma\right) = \frac{a}{\left(E_\gamma - c + \mathrm{e}^{-0.269E_\gamma}\right)^b}, \tag{4.7}$$

where a, b and c are the parameters of the fit. Figure 4.8 shows the efficiency curves for each ring of SeGA. Two γ-ray sources were used in the calibration. The ^{152}Eu data, shown as blue points in Figure 4.8, was taken using a ^{152}Eu source of known activity, while the ^{226}Ra data, red points in Figure 4.8, were taken with a source for which the activity is not precisely known. For this reason, the ^{226}Ra data was fit with an additional parameter to scale the overall curve to match the ^{152}Eu data. The total efficiency of SeGA is the sum of the efficiency of each ring. Due to the angular dependence of the Lorentz boost, the 90° and 37° rings of SeGA must be treated separately in order to determine the in-beam efficiency.

4.1.4 Doppler-shift Reconstruction

The beam particles are traveling at a large fraction of the speed of light ($v/c > 0.3$) when they emit γ rays, so the energy of the γ rays is significantly Doppler shifted in the laboratory frame, according to Equation 3.6. At the beam velocities used in this experiment, the Doppler

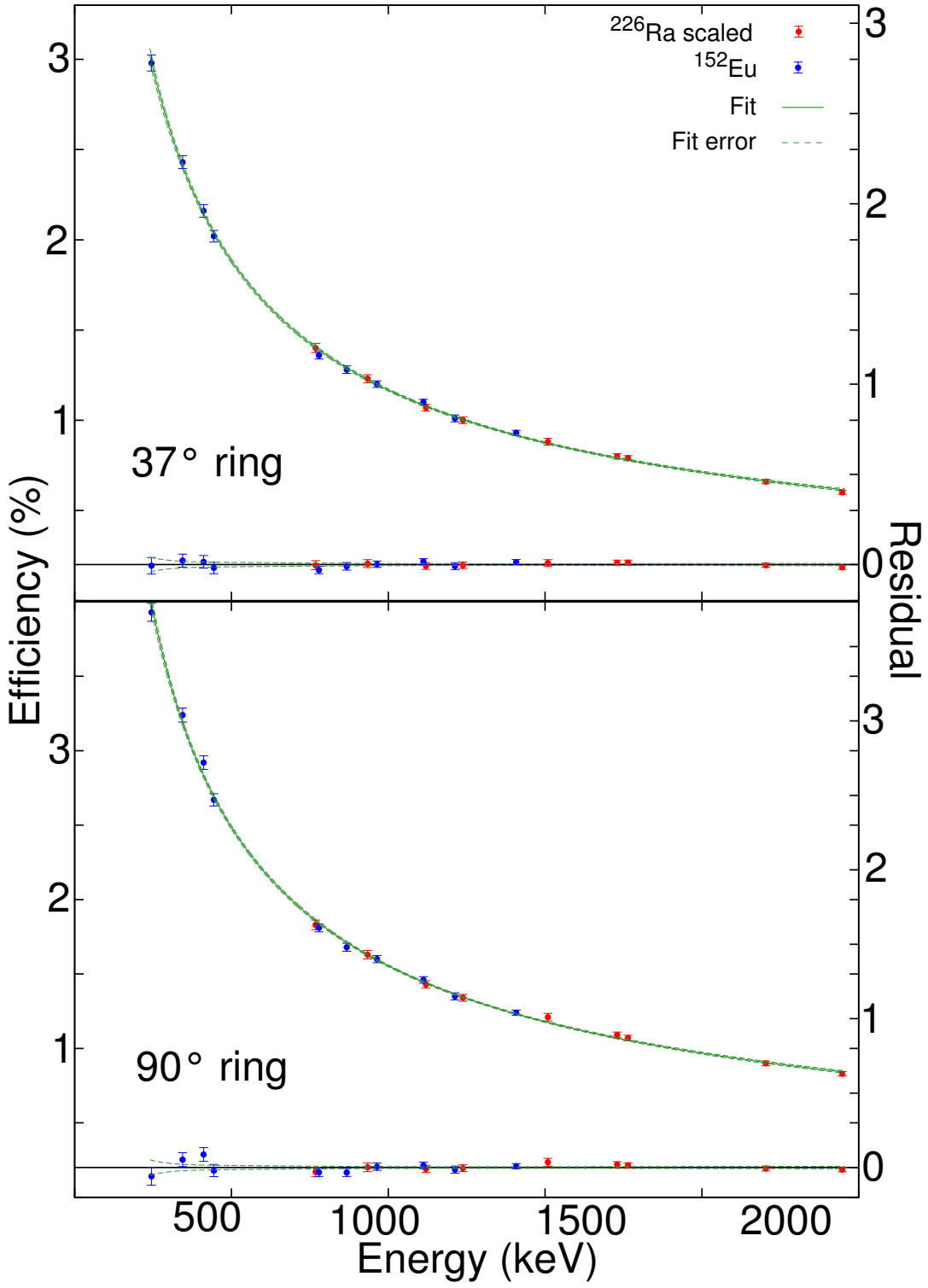

Figure 4.8: γ-ray detection efficiency curves for the two rings of SeGA.

shift is clearly evident. Figure 4.9 shows the γ-ray spectrum detected in coincidence with ^{58}Cr for each of the two rings of SeGA. In Figure 4.9, no Doppler correction has been applied. Visible are several γ-ray lines originating from the room background. Common sources of background radiation include ^{40}K and the natural ^{238}U and ^{232}Th decay chains. The most prominent lines have been labeled. Figure 4.10 explores the cluster of lines around 500 keV. Here, the 547-keV peak corresponds to the deexcitation of the $7/2_1^+$ level to the $3/2_{\rm gs}^+$ ground state from the Coulomb excitation of the ^{197}Au target. Also apparent is the large low-energy background in both rings below approximately 400 keV. This is beam-correlated background caused by *bremsstrahlung*: radiation produced by electrons of target nuclei gaining energy from collisions with beam particles as the beam passes through the target. Also visible are two broad structures, one in each ring. These are the Doppler-shifted $2^+ \rightarrow 0^+$ deexcitation γ rays from the Coulomb excitation of ^{58}Cr. The opening angle of the SeGA detectors spreads out the peak due to the Doppler shift. The positions of the Doppler-shifted peaks are given by Equation 3.6.

To transform the γ-ray spectra into the rest frame of the projectile, an event-by-event Doppler correction is performed. The γ-ray energy in the rest frame, $E_\gamma^{\rm rest}$, is given in terms of the lab energy, $E_\gamma^{\rm lab}$, by

$$E_\gamma^{\rm rest} = E_\gamma^{\rm lab}\gamma\left(1 - \beta\cos\theta\right), \tag{4.8}$$

where $\beta = v/c$ and θ is the emission angle of the γ ray relative to the direction of travel of the projectile. In SeGA experiments, this angle is taken to be the angle of the detector segment which registered the highest energy deposit.

Figure 4.11 shows the γ-ray spectrum measured in coincidence with ^{58}Cr particles after Doppler correction. The sharp background lines evident in Figures 4.9 and 4.10 are no longer

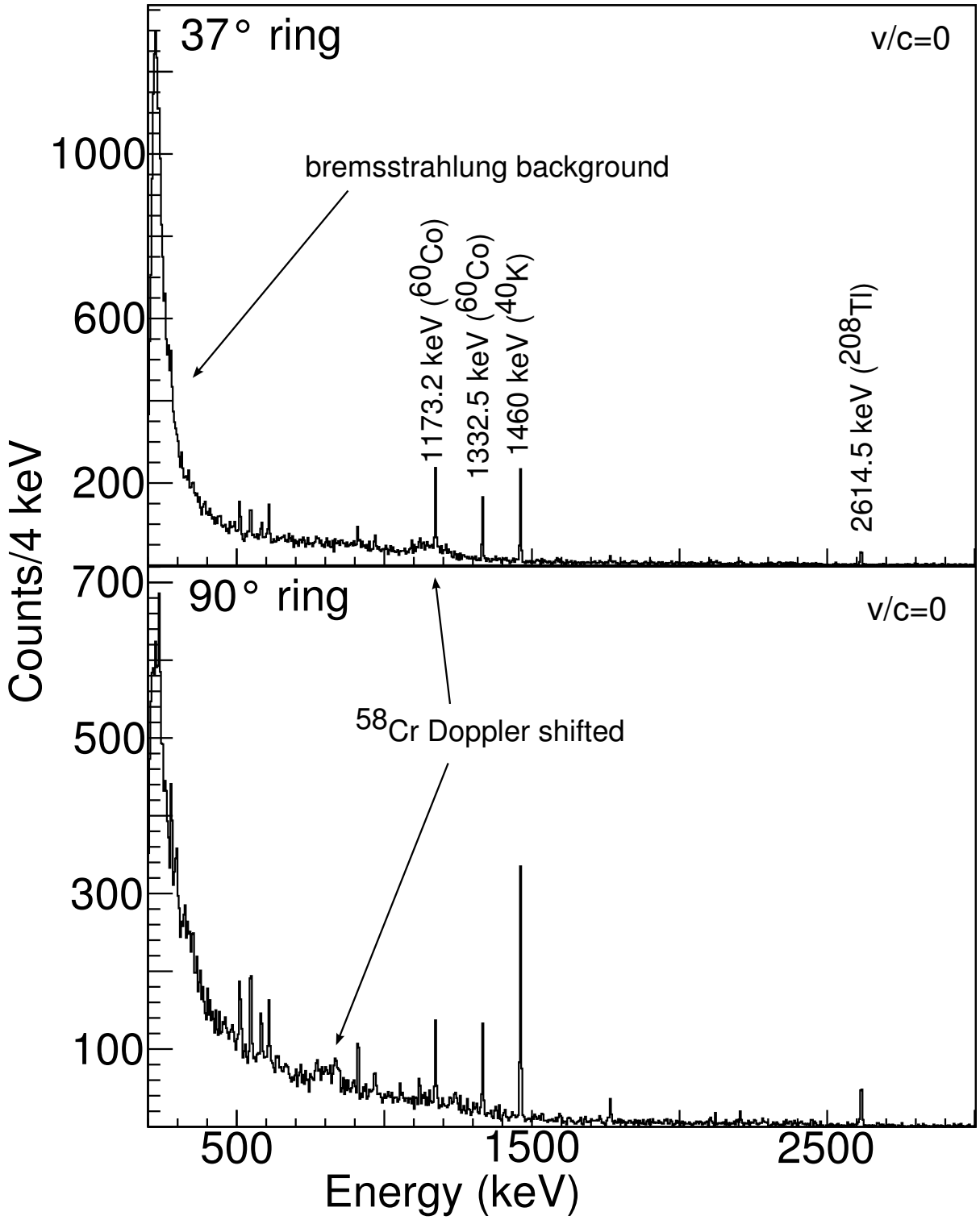

Figure 4.9: γ-ray spectrum measured in coincidence with ^{58}Cr particles in the laboratory frame. The cluster of peaks around 500 keV is expanded in Figure 4.10.

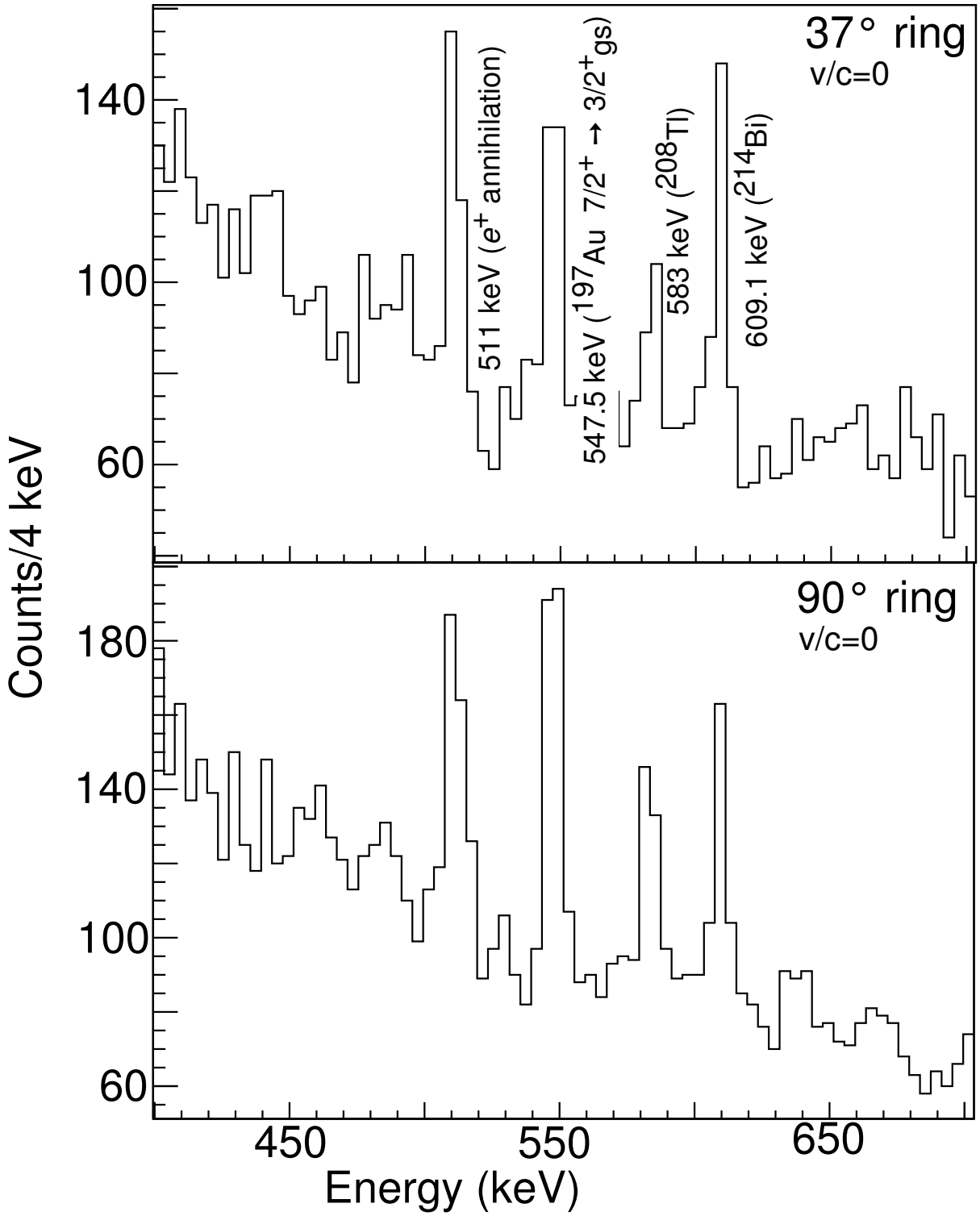

Figure 4.10: Expanded view of the spectra shown in Figure 4.9.

visible, they have been distributed among the background in Figure 4.11 in the Doppler reconstruction. The main feature in Figure 4.11 is the peak at 881(6) keV corresponding to the deexcitation of the 2_1^+ state in ^{58}Cr to the 0_{gs}^+ ground state.

4.1.5 Scattering-angle Cuts and γ-ray Spectra

In order to constrain the impact parameter in the Coulomb excitation reaction, cuts must be made on the scattering angle, θ, restricting the minimum impact parameter. The effect of the scattering-angle cut on the γ-ray spectrum is illustrated in Figure 4.12 and quantified in Table 4.3 for ^{58}Cr.

Angle Cut (mrad)	Peak Area	Percentage of Total (%)
All angles	952(53)	100
<40	666(49)	70
<30	462(47)	48
<20	263(45)	28

Table 4.3: Effect on peak area of the scattering angle cuts shown in Figure 4.12.

The *safe scattering angle*, $\theta^{\max}$, is the scattering angle corresponding to the minimum impact parameter, $b_{\min}$. $b_{\min}$ is defined in Equation 2.24 as the sum of the radii of the target and projectile nuclei plus 2 fm. According to Equation 2.25, $\theta^{\max}$ is given by

$$b_{\min} = \frac{a_0}{\gamma} \cot\left(\frac{\theta_{\mathrm{cm}}^{\max}}{2}\right). \tag{4.9}$$

The minimum impact parameters, maximum scattering angles in the lab and center of mass frames are summarized in Table 4.4.

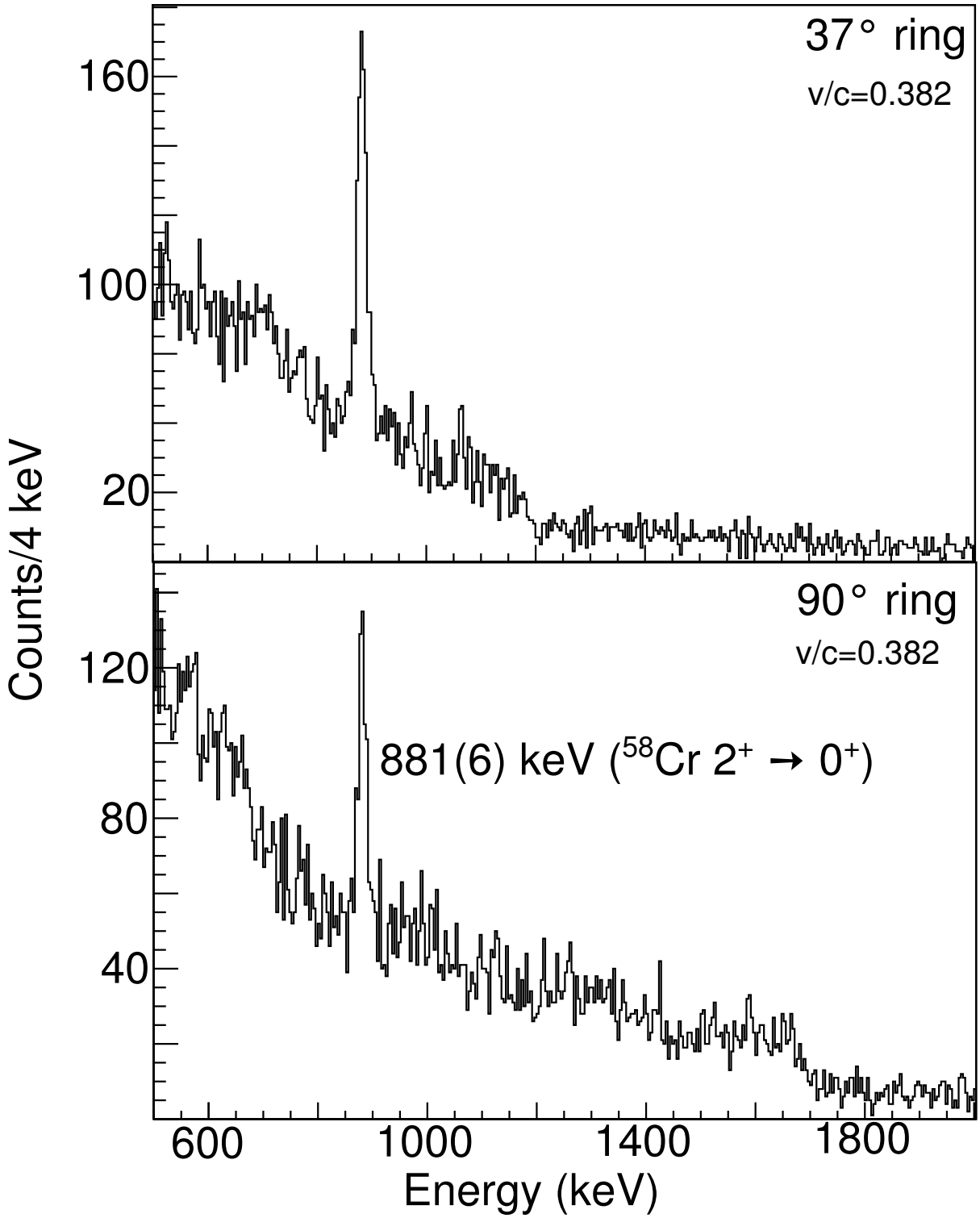

Figure 4.11: γ-ray spectrum measured in coincidence with ^{58}Cr particles with Doppler correction applied. The many background peaks have been replaced by a single peak from the deexcitation of ^{58}Cr nuclei excited by Coulomb excitation in the ^{197}Au target.

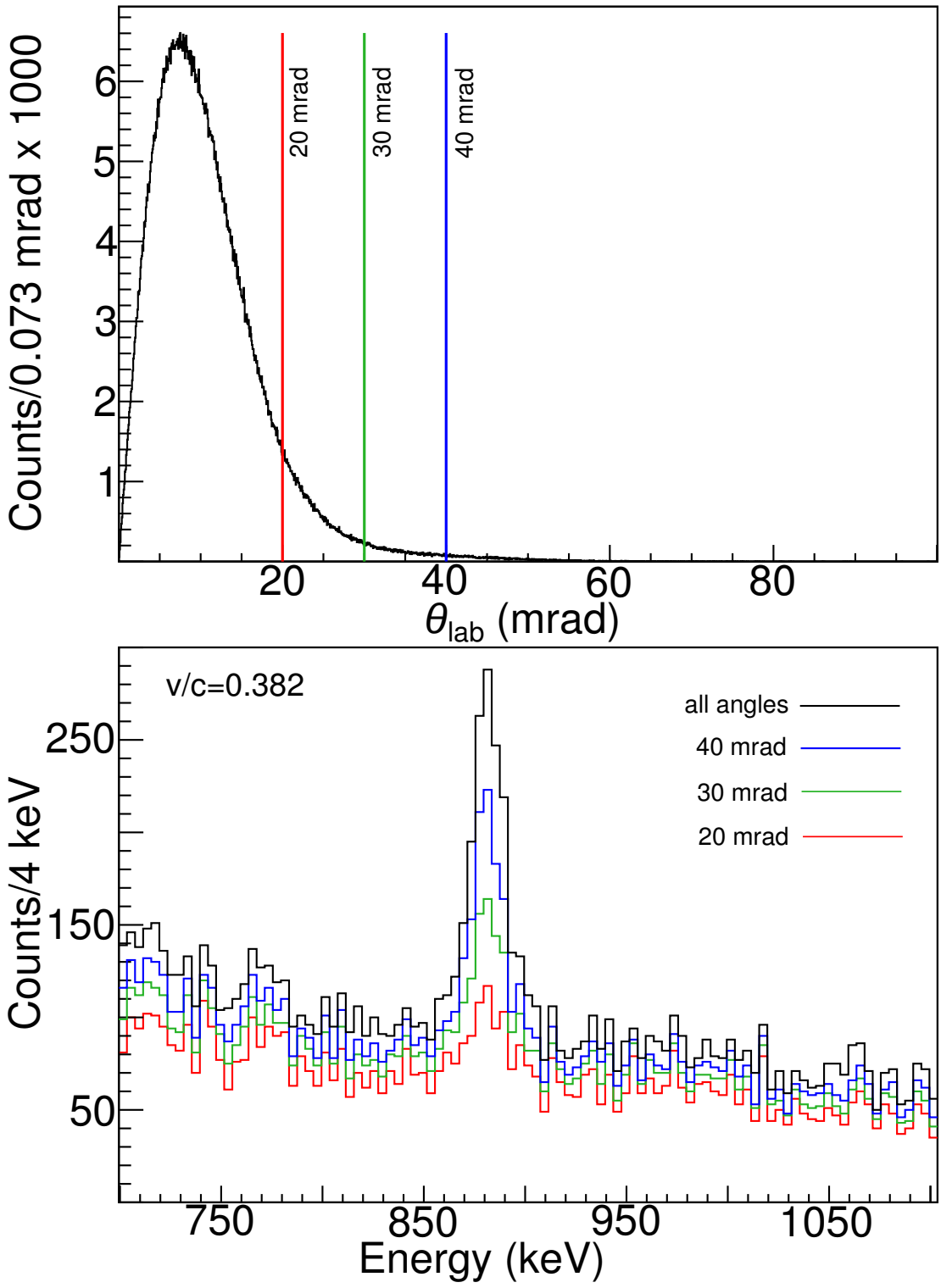

Figure 4.12: Scattering angle distribution (top panel) for ^{58}Cr particles. The vertical lines represent the maximum scattering angle corresponding to a software cut. The corresponding γ-ray spectra (bottom panel) show γ rays from ^{58}Cr particles with scattering angles less than the scattering angle cut.

Beam/target	b_{min} (fm)	$\theta_{\text{cm}}^{\text{max}}$ (mrad)	$\theta_{\text{lab}}^{\text{max}}$ (mrad)
^{58}Cr/^{197}Au	14.1	55.4	42.2
^{60}Cr/^{197}Au	14.2	53.8	40.6
^{62}Cr/^{209}Bi	14.4	54.9	41.7

Table 4.4: b_{min}, $\theta_{\text{cm}}^{\text{max}}$, $\theta_{\text{lab}}^{\text{max}}$ for ^{58,60,62}Cr used in this experiment.

The Doppler-corrected γ-ray spectra with the θ^{max} gates applied for ^{58,60,62}Cr are shown in Figures 4.13, 4.14, and 4.15. In each case the de-excitation γ ray from Coulomb excitation is clearly seen. One notable feature is the asymmetric shape of the ^{62}Cr peak, which exhibits a pronounced low-energy tail. This is indicative of an excited-state lifetime on the order of $\sim$100 ps. As will be discussed in Section 4.3, the shape of the peak can be used to extract the lifetime of the excited state and provides an independent measure of the $B(E2)$ value.

4.2 GEANT Simulations

Monte-Carlo Simulations were used to extract the γ-ray yields from the measured spectra. The simulations were performed using GEANT4 [86] and incorporated the geometry and response of SeGA, energy loss of the beam particles as they passed through the target, the γ-ray angular distribution, and the excited-state lifetimes, as well as γ-ray attenuation in the target, beam pipe, and detector materials. A rendering of the simulated SeGA array is shown in Figure 4.16. The simulated peaks were fit to the measured spectra using a χ^2 minimization to determine the number of γ rays emitted following Coulomb excitation. The target dimensions were 5 cm $\times$ 5 cm $\times$ 130 μm for the gold target used for the Coulomb excitation of ^{58,60}Cr and 5 cm $\times$ 5 cm $\times$ 250 μm for the bismuth target used for the Coulomb

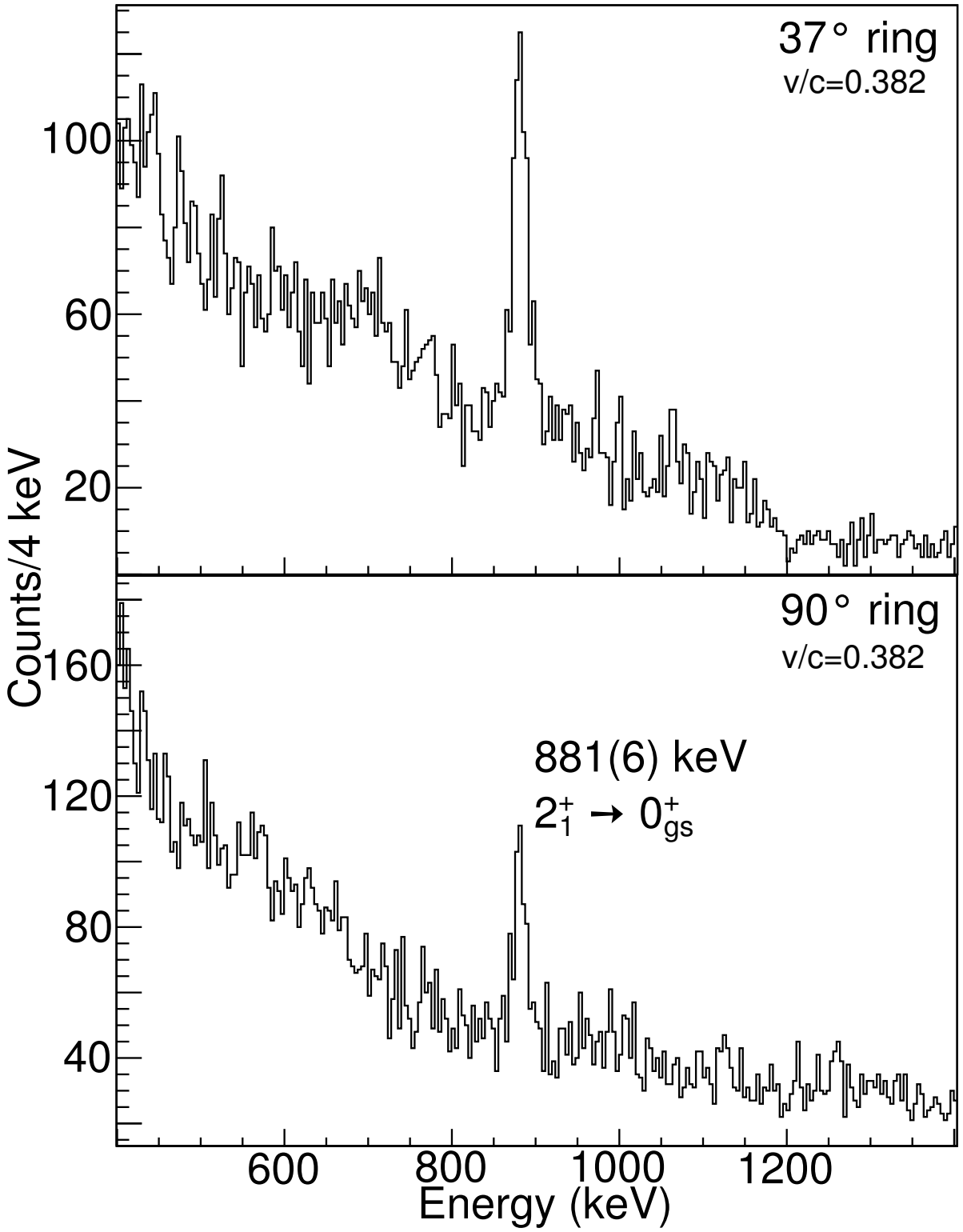

Figure 4.13: γ rays detected in coincidence with ^{58}Cr projectiles which were scattered at an angle less than $\theta^{\max}$. The dexcitation of the 881(6)-keV 2_1^+ state to the 0_{gs}^+ ground state is observed in both rings.

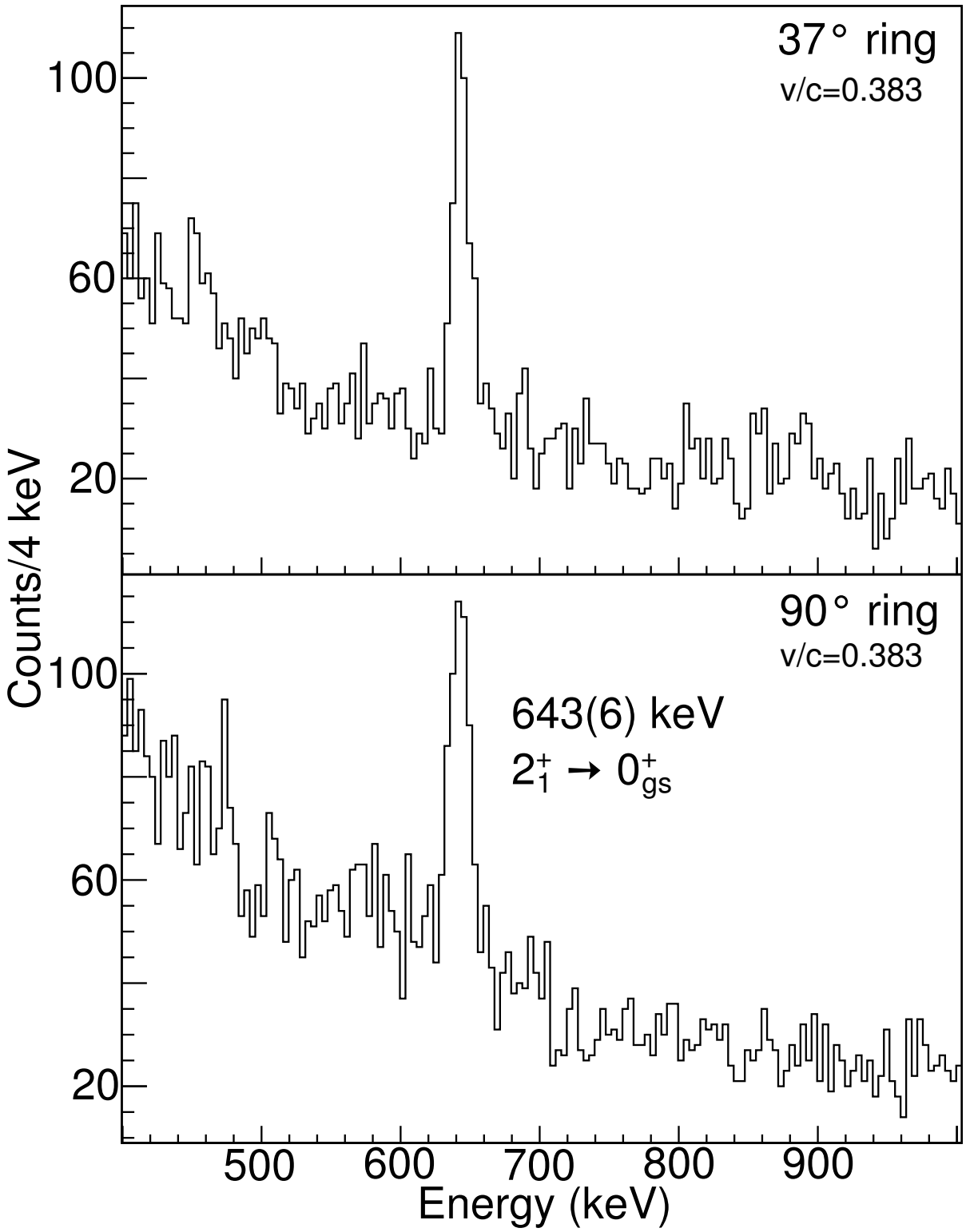

Figure 4.14: γ rays detected in coincidence with ^{60}Cr projectiles which were scattered at an angle less than $\theta^{\max}$. The dexcitation of the 643(6)-keV 2_1^+ state to the 0_{gs}^+ ground state is observed in both rings.

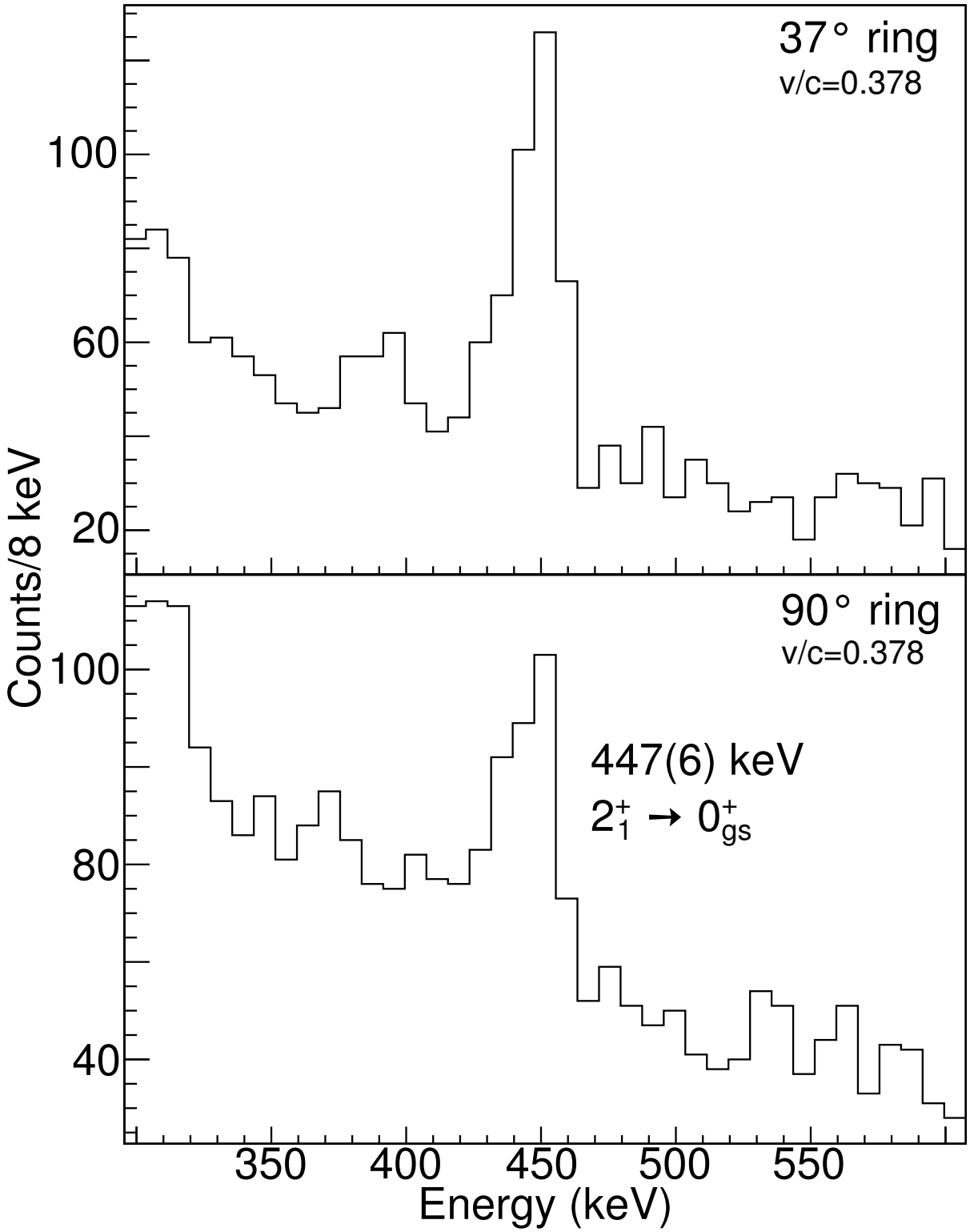

Figure 4.15: γ rays detected in coincidence with ^{62}Cr projectiles which were scattered at an angle less than $\theta^{\max}$. The dexcitation of the 447(6)-keV 2_1^+ state to the 0_{gs}^+ ground state is observed in both rings. It is notable that the peak exhibits a pronounced left tail. This is indicative of an excited-state lifetime of order 100 ps.

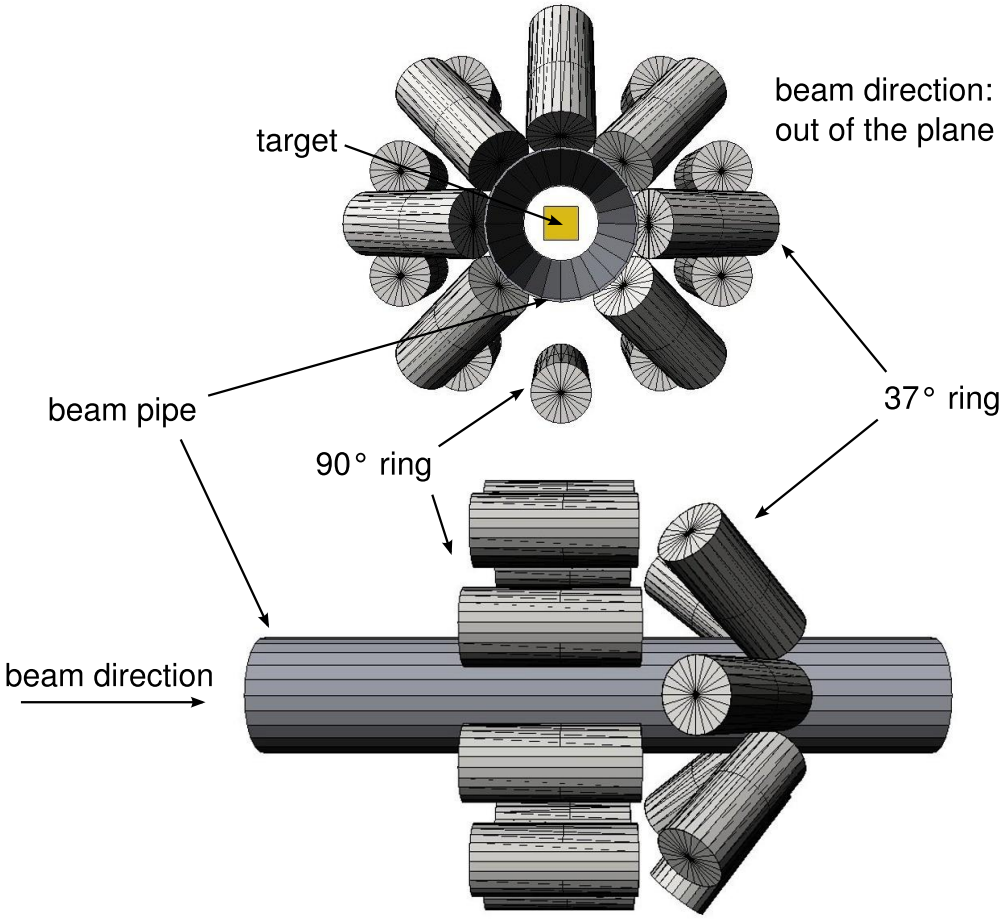

Figure 4.16: A three-dimensional rendering of the simulated SeGA array used in the analysis. For clarity, only the positions of the SeGA germanium crystal housing are shown. The detector cryostats and SeGA frame are not shown, but were included in the simulation.

excitation of ^{62}Cr. The thickness of the aluminium beam pipe was 2.54 mm with an outer diameter of 7.62 cm.

4.2.1 Simulation of Sources

To benchmark the simulated detector efficiency with respect to the measured efficiency for SeGA, a simulation of an ^{152}Eu source was performed and compared to the measured γ-ray spectrum. The peaks of the ^{152}Eu spectrum were simulated individually and summed into a

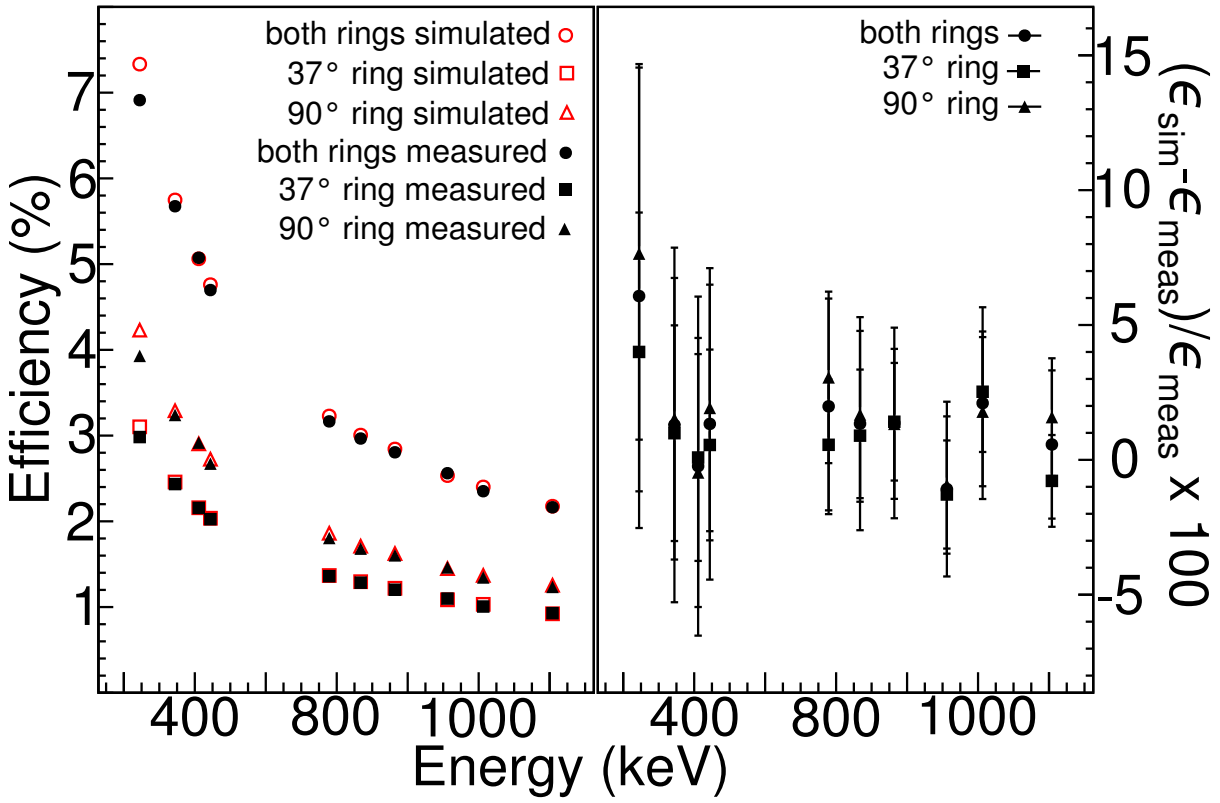

Figure 4.17: Comparison of simulated and measured absolute efficiencies of SeGA in the experimental situation.

single spectrum, taking into account the known branching ratios. The peaks were then fit in the same way as the measured spectra. The resulting efficiencies are compared in Figure 4.17. The average percent difference between the simulated and measured efficiency was $\delta^{37^\circ}_{\mathrm{GEANT}} = 0.9\%$ for the 37° ring and $\delta^{90^\circ}_{\mathrm{GEANT}} = 1.9\%$ for the 90° ring.

4.2.2 Simulations of SeGA's in-beam Response

To simulate the in-beam response of the setup, a beam particle of the desired A and Z is generated and fired into the target. The beam particle loses energy as it traverses the target and the excitation occurs at a random point in the target. This is appropriate as the Coulomb-excitation cross-section does not change significantly at the present level of energy loss. The excited particle then decays by γ-ray emission with a time distribution determined

by the excited-state lifetime. The γ ray is emitted taking into account the Lorentz boost and γ-ray angular distribution in Coulomb excitation. The simulation then records the energy deposited in SeGA by the γ ray, as well as the detector and segment the energy was deposited in. The simulated γ-ray data were then sorted into spectra using the same algorithm as the actual data. The angle of the segment registering the highest energy deposit was taken to calculate the angle used for Doppler reconstruction.

The simulations were tuned so that the outgoing beam parameters of the simulation reproduced those measured in the experiment, as shown in Figure 4.18.

For each case of ^{58,60,62}Cr, several scattering angle cuts were made and different simulations were performed to take into account the different angular distributions calculated for the different impact parameter ranges. The angular distributions for ^{58}Cr + ^{197}Au Coulomb excitation for different scattering angle cuts are shown in Figures 4.19 and 4.20 with an isotropic distribution for comparison. Figure 4.19 shows the angular distributions for the 547-keV $7/2^+ \rightarrow 3/2^+$ deexcitation originating from the Coulomb excited ^{197}Au target.

Figure 4.20 shows the Lorentz-boosted Coulomb-excitation angular distribution of the 881-keV $2^+ \rightarrow 0^+$ transition resulting from Coulomb excitation of ^{58}Cr nuclei by ^{197}Au target.

4.2.2.1 Fits of Lab-frame Spectra

In addition to simulating the in-beam peak shapes of γ-ray transitions from the chromium, the ^{197}Au 547-keV $7/2^+ \rightarrow 3/2^+$ transition from Coulomb excitation of the target was simulated, as well as the 511-, 583-, 609-, 1173-, 1332-, and 1460-keV background peaks. To take into account the background present in the spectrum and fit the ^{197}Au peak, the

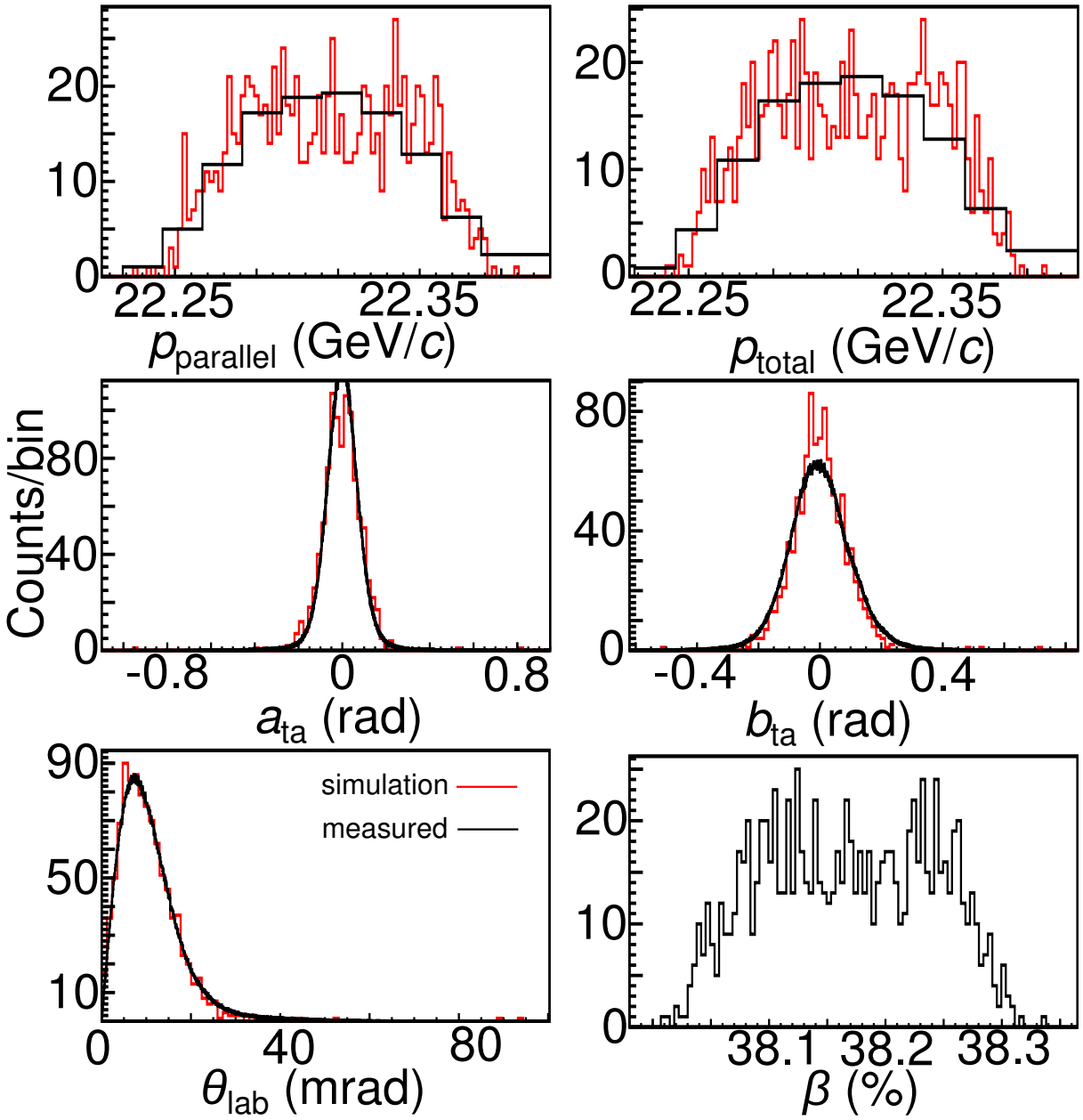

Figure 4.18: Comparison of simulated and measured parallel and total momentum distributions, a_{ta}, b_{ta}, and θ_{lab}, and the distribution of $\beta = v/c$ values for beam particles exiting the target.

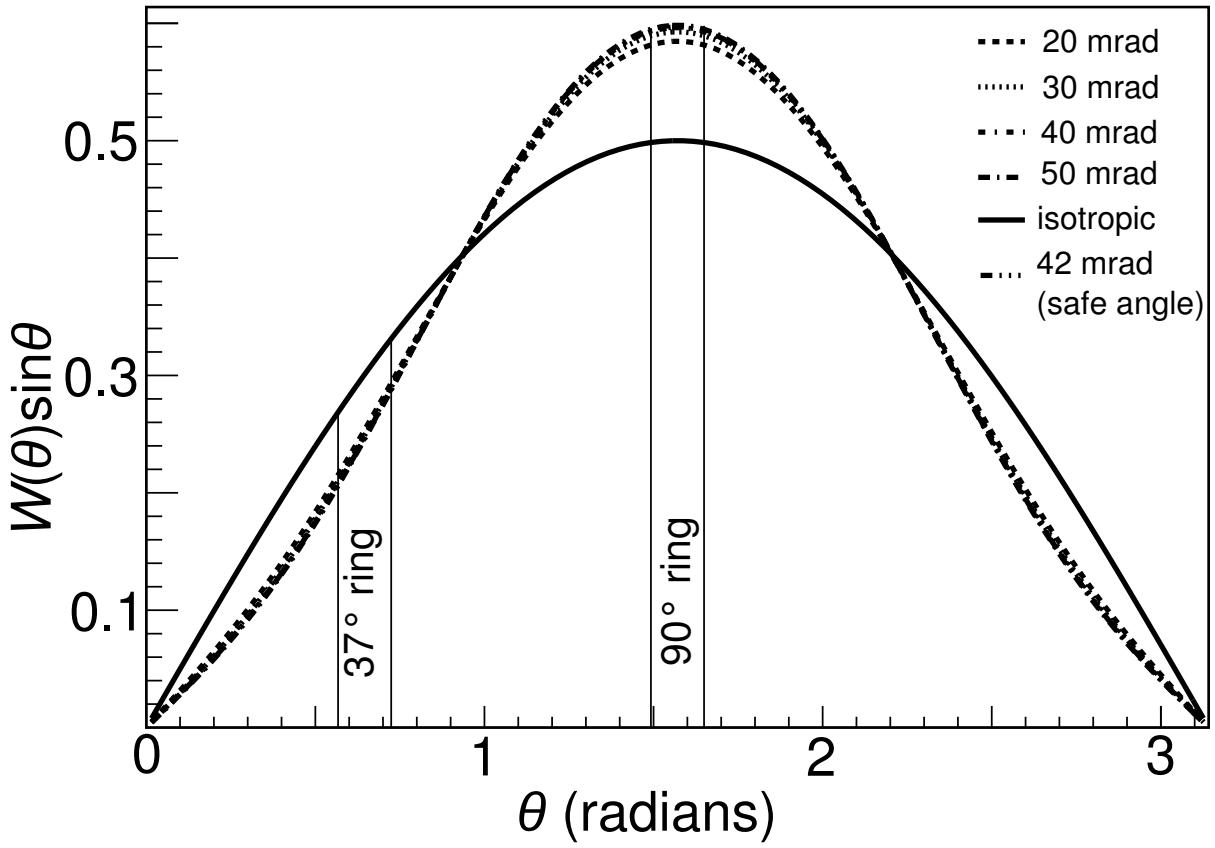

Figure 4.19: Coulomb-excitation angular distributions calculated for the 547-keV $7/2^+ \rightarrow 3/2^+$ transition resulting from Coulomb excitation of ^{197}Au target nuclei by ^{58}Cr projectiles, with a β value of 0.392 for various maximum laboratory scattering angles. An isotropic distribution is shown for comparison.

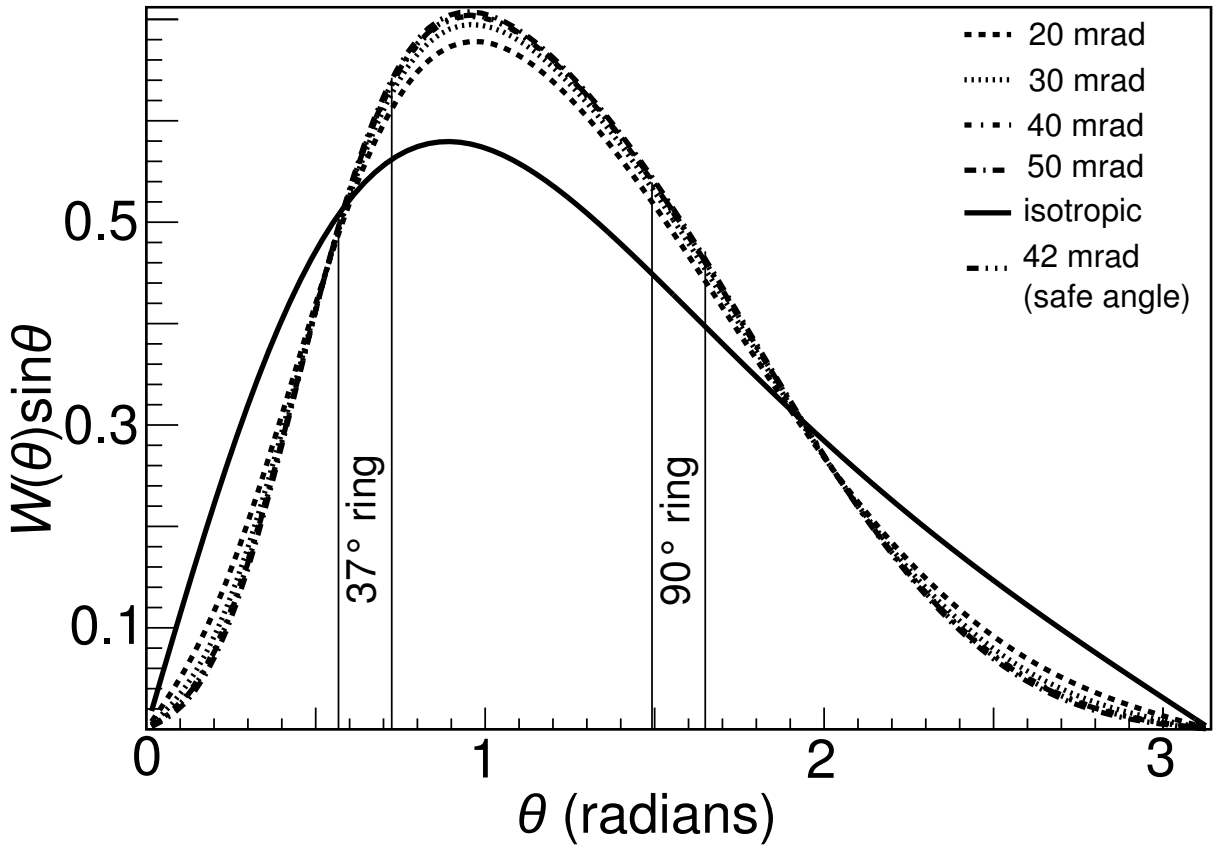

Figure 4.20: Lorentz-boosted Coulomb-excitation angular distributions calculated for the 881-keV $2^+ \rightarrow 0^+$ transition resulting from Coulomb excitation of ^{58}Cr projectiles by a ^{197}Au target, with a β value of 0.392 for various maximum laboratory scattering angles. Lorentz-boosted isotropic distribution is shown for comparison.

non-Doppler-corrected spectrum was fitted with a function of the form:

$$f(E_\gamma) = \sum_i p_i \mathrm{sim}_i + p_{\mathrm{Au}}\mathrm{sim}_{\mathrm{Au}} + p_{\mathrm{Cr}}\mathrm{sim}^{\beta}_{\mathrm{Cr}} + a + bE_\gamma + cE^2_\gamma, \tag{4.10}$$

where the p_x are fit scaling parameters, sim_x are simulated peaks, a, b, and c are parameters. The subscripts i refer to the specific background peak being simulated in the fit, Au and Cr are the simulated gold and chromium peaks, respectively, and the β superscript signifies that the simulation is Doppler-boosted in the laboratory frame. The particular simulations included in the fit depends on the particular case and the range of the spectrum being fit. Figure 4.21 shows a fit of γ rays measured in coincidence with ^{58}Cr particles over a range of E_γ from 500 to 700 keV.

Figure 4.22 shows a different portion of the same spectrum shown in Figure 4.21. In this case the ^{58}Cr peak is Doppler shifted underneath of the 1173-keV line, complicating the fit. After Doppler correcting the ^{58}Cr peak, the background lines will be spread out beneath the Coulomb-excitation peak, contaminating the measurement. To attempt to correct for this, the background lines which overlap the Doppler-shifted ^{58}Cr peak are fitted and were included in the fits of the ^{58}Cr peak.

Figure 4.23 shows fits of γ rays measured in coincidence with ^{60}Cr nuclei with scattering angle less than θ_{max}. Again, the location of the Doppler-shifted ^{60}Cr peak and background lines overlap.

Figure 4.24 shows γ rays measured in coincidence with ^{62}Cr particles scattered at angles less than θ_{max}. There is no 547-keV line in the spectrum because a ^{209}Bi target was used instead of the ^{197}Au target. In this case the ^{62}Cr peak is Doppler shifted under the 583- and 609-keV peaks.

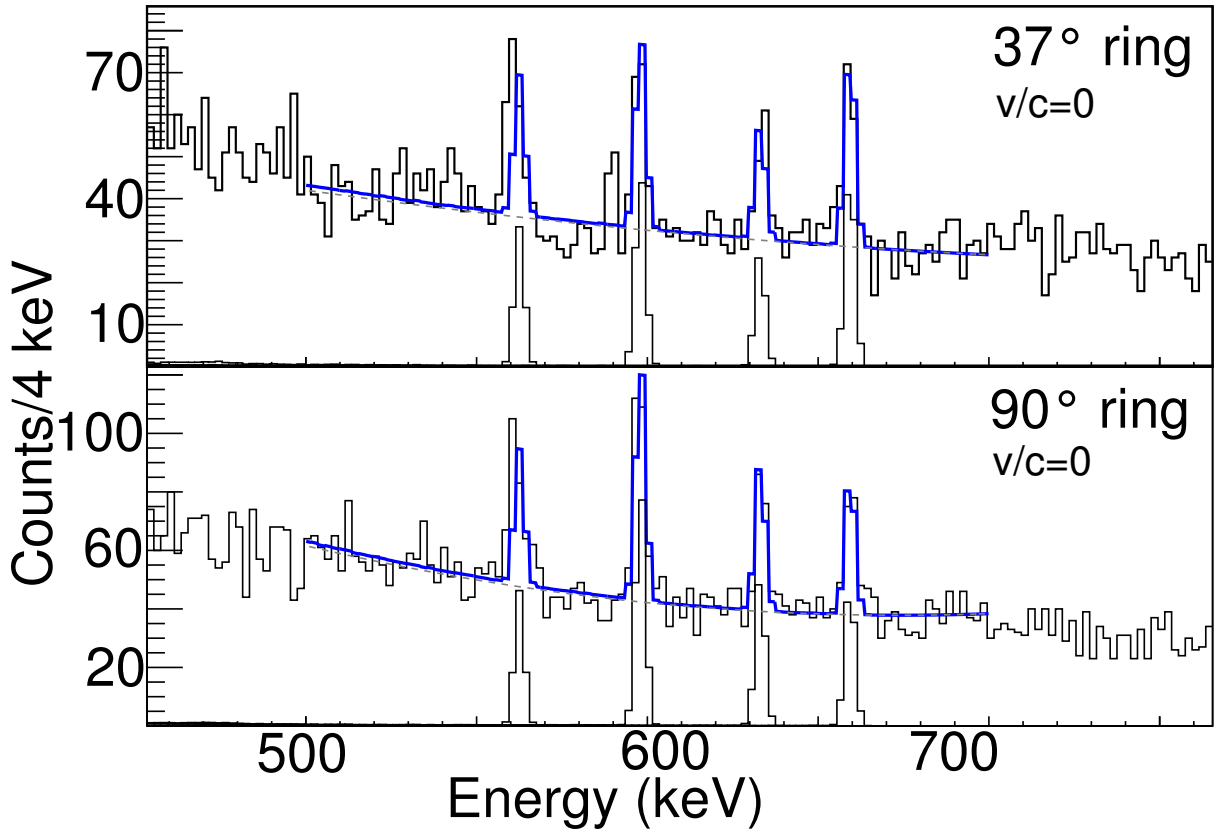

Figure 4.21: Fits of the γ-ray spectra measured in coincidence with ^{58}Cr particles with scattering angle less than $\theta_{\max}$. Data is shown in black and the fit is the blue curve. A quadratic background is shown as a dashed line. The 511-, 583-, and 609-keV background lines discussed in Section 4.1.4 and Figure 4.10 are included in the fit along with the 547-keV γ ray from Coulomb excitation of the gold target.

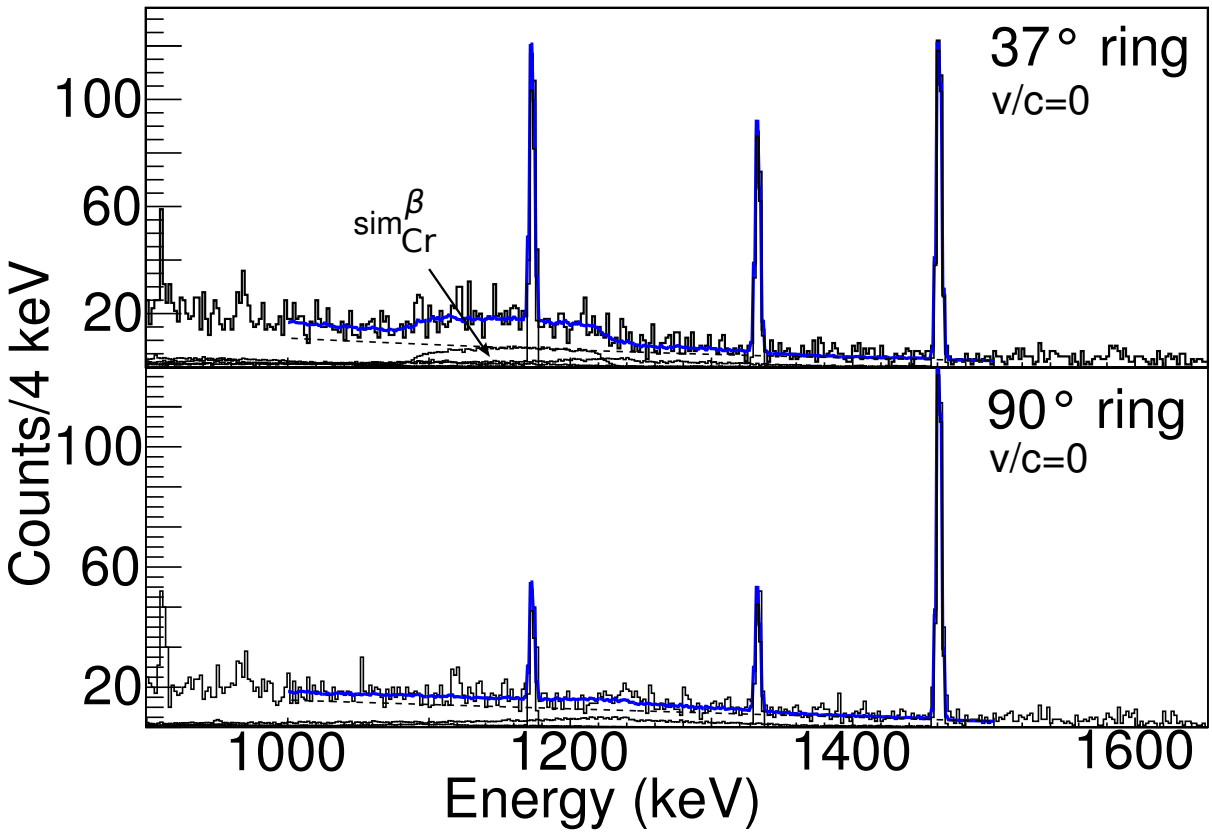

Figure 4.22: Fits of the γ-ray spectra measured in coincidence with ^{58}Cr particles with scattering angles less than $\theta_{\max}$. Data is shown in black and the fit is in blue. A quadratic background is shown as a dashed line. The 1173-, 1332-, 1460-keV background lines discussed in Section 4.1.4 and Figure 4.9 are included in the fit along with the Doppler shifted ^{58}Cr peak, labeled sim$^{\beta}_{\mathrm{Cr}}$, is visible as the broad structure under the 1173-keV background peak in the 37° ring.

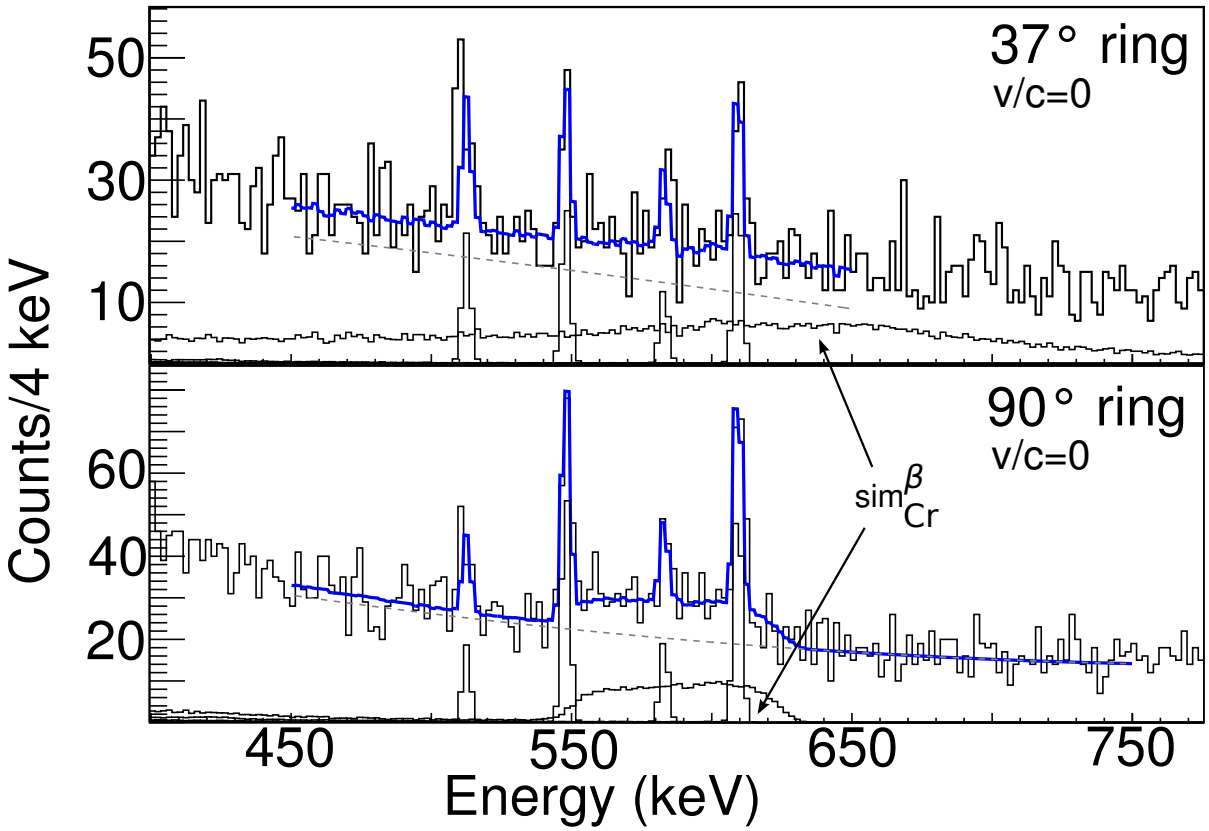

Figure 4.23: Fits of the γ-ray spectra measured in coincidence with ^{60}Cr particles with scattering angles less than $\theta_{\max}$. Data is shown in black and the fit is in blue. A quadratic background is shown as a dashed line. The 511-, 583-, and 609-keV background lines discussed in Section 4.1.4 and Figure 4.10 are included in the fit along with the 547-keV γ ray from Coulomb excitation of the gold target along with the Doppler shifted ^{60}Cr peak is visible as the broad structure under the 547-, 583-, and 609-keV peaks.

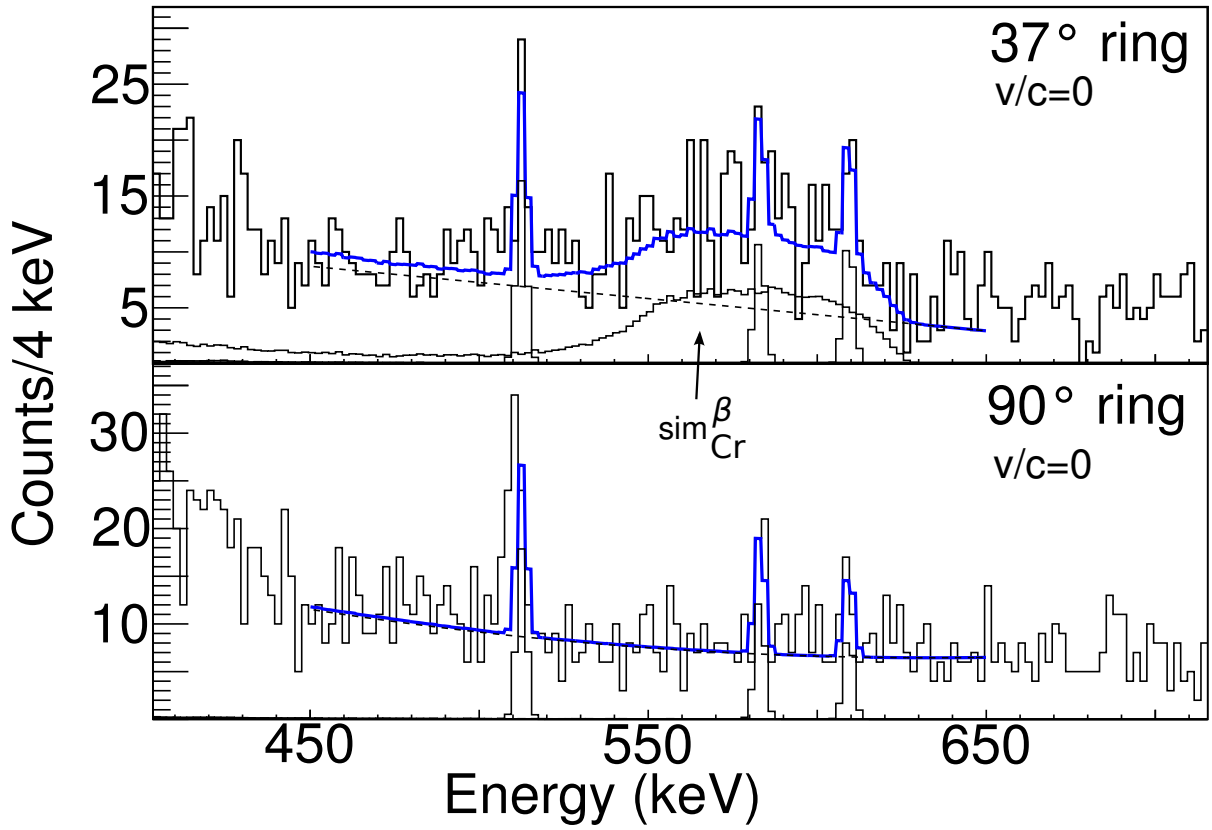

Figure 4.24: Fits of the γ-ray spectra measured in coincidence with ^{62}Cr particles with scattering angles less than $\theta_{\max}$. Data is shown in black and the fit is in blue. A quadratic background is shown as a dashed line. The 511-, 583-, and 609-keV background lines discussed in Section 4.1.4 and Figure 4.10 are included in the fit along with the Doppler shifted ^{62}Cr peak is visible as the broad structure under the 583- and 609-keV peaks.

4.2.2.2 Fits of Projectile-frame Spectra

Once the non-Doppler-corrected spectra were fit, the Doppler-corrected spectra could be fit using the function

$$f(E_\gamma) = \sum_i p_i \mathrm{sim}_i^0 + p_{\mathrm{Cr}} \mathrm{sim}_{\mathrm{Cr}} + a\mathrm{e}^{-b(E_\gamma - c)} + d\mathrm{e}^{-e(E_\gamma - f)}, \tag{4.11}$$

where the p_x are fit scaling parameters, sim_x are simulated peaks, a, b, c, d, e, and f are parameters used to fit a double exponential for the background. The subscripts i refer to the specific background peak being simulated in the fit, Cr is the simulated chromium peak, and the 0 superscript signifies that the simulation of background lines that were at rest in the lab frame, but have been Doppler corrected. The particular simulations included in the fit depends on the particular case and the range of the spectrum being fit. The scale factors of the background peaks that were fit in the rest frame were fixed to the same values for the fits in the projectile frame.

Figures 4.25, 4.26, and 4.27 show Doppler-corrected γ-ray spectra detected in coincidence with ^{58,60,62}Cr particles with scattering angles less than θ_{max}, along with the fit of the simulations to the data.

Results from the fits will be presented in Section 4.3 below.

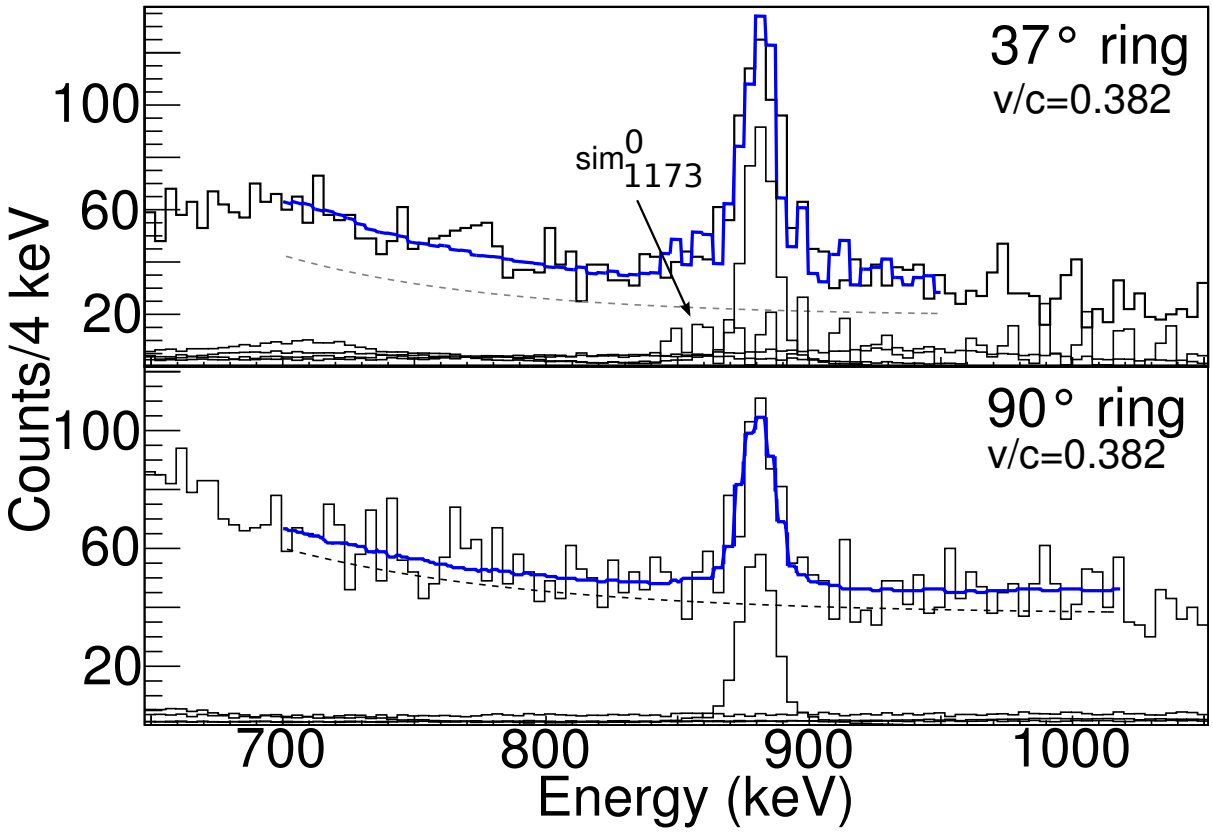

Figure 4.25: Doppler-corrected γ-ray spectra detected in coincidence with ^{58}Cr particles with scattering angles less than $\theta_{\max}$. The measured spectrum is shown in black and the fit is drawn in blue. Also visible are the Doppler-corrected background lines from the lab frame.

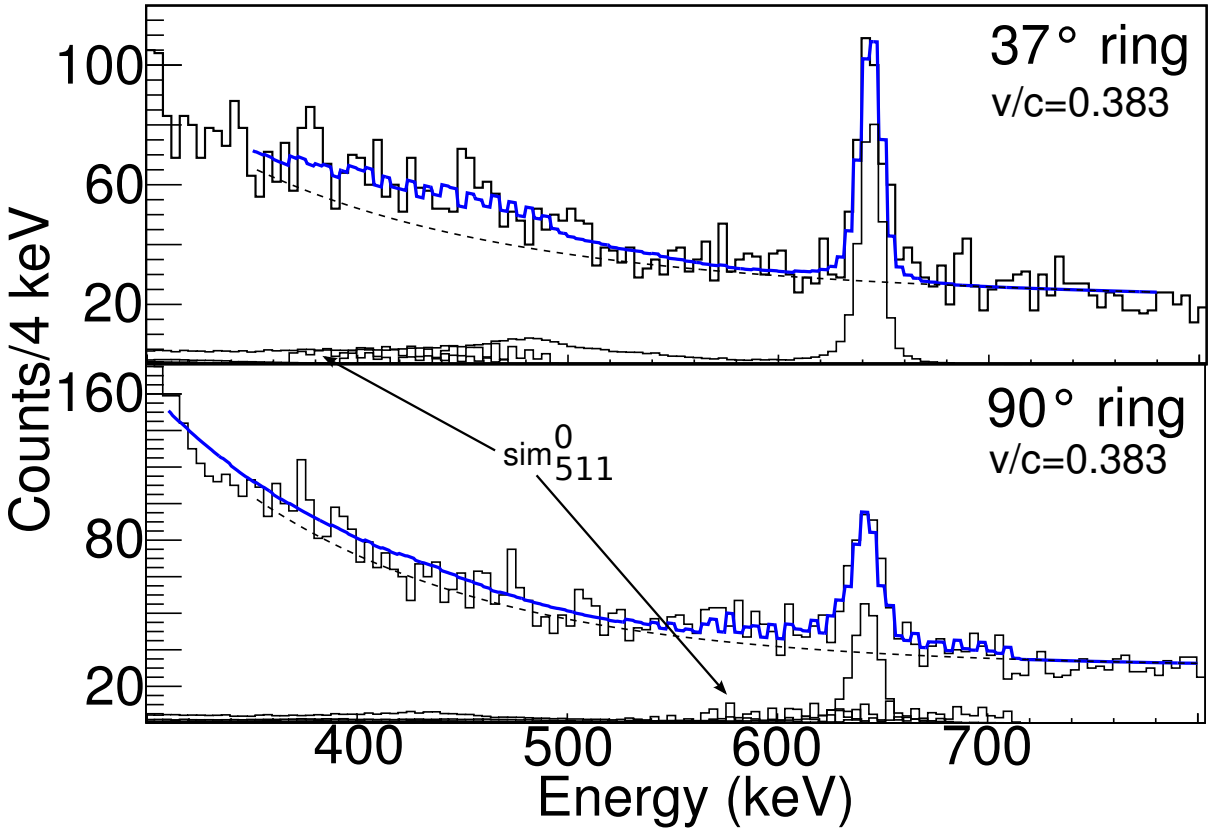

Figure 4.26: Doppler-corrected γ-ray spectra detected in coincidence with ^{60}Cr particles with scattering angles less than $\theta_{\max}$. The measured spectrum is shown in black and the fit is drawn in blue. Also visible are the Doppler-corrected background lines from the lab frame.

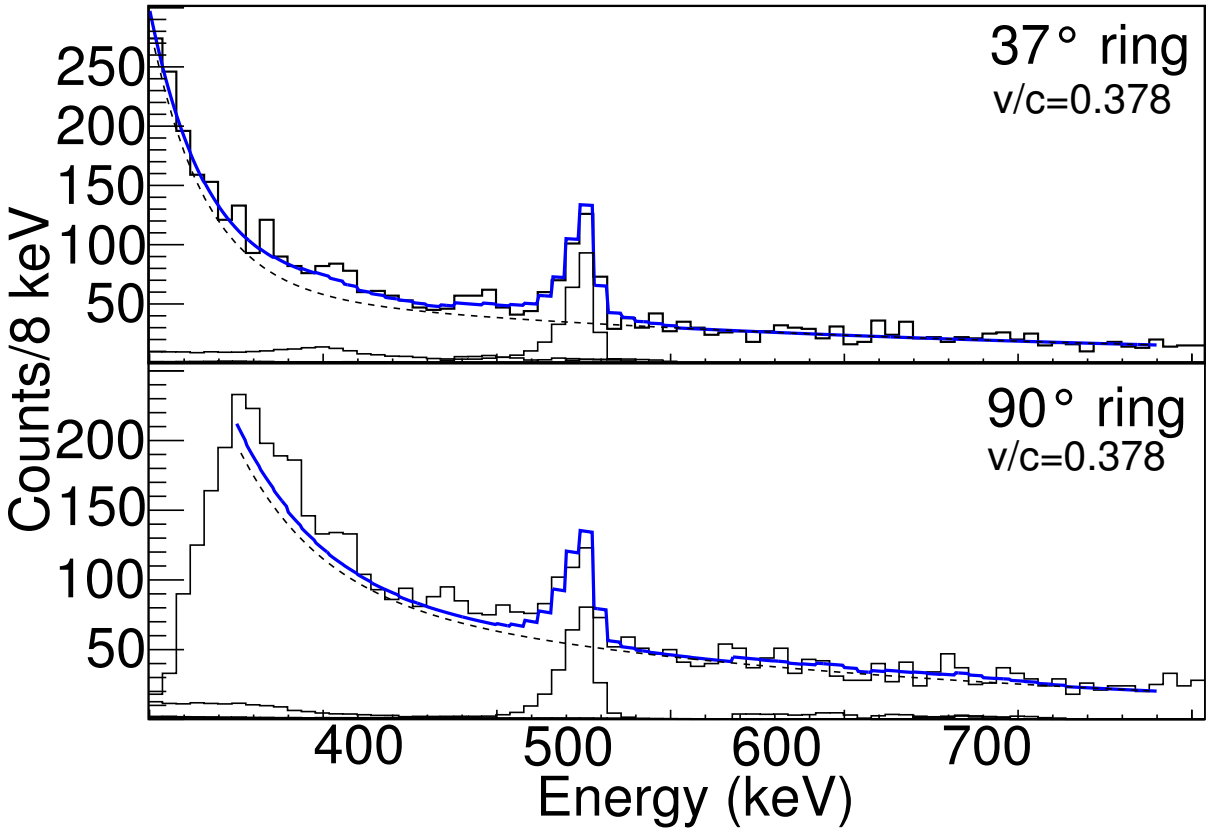

Figure 4.27: Doppler-corrected γ-ray spectra detected in coincidence with ^{62}Cr particles with scattering angles less than $\theta_{\max}$. The measured spectrum is shown in black and the fit is drawn in blue. Also visible are the Doppler-corrected background lines from the lab frame.

4.3 Results and Discussion

4.3.1 Cross Sections

The measured Coulomb-excitation cross section is

$$\sigma_{\text{Coulex}} = \frac{N_\gamma}{N_{\text{beam}} N_{\text{target}} \epsilon}. \tag{4.12}$$

where N_γ is the number of γ rays in the Coulomb-excitation peak, N_{beam} is the number of beam particles, N_{target} is the number of target atoms per unit area, and ϵ is the γ-ray detection efficiency. N_{target} is

$$N_{\text{target}} = \frac{\rho N_{\text{A}}}{A}, \tag{4.13}$$

where ρ is the density of the target in g/cm^2, N_{A} is Avagadro's number ($N_{\text{A}} = 6.022 \times 10^{23}$ particles/mole) and A is the atomic mass of the target in g/mole.

N_{beam} is the number of beam particles of the desired species passing through the target. This number is taken from the S800 trigger register, which counts the number of times the data acquisition is triggered, N_{trigger}. This number needs to be corrected for the *livetime* of the data acquisition system for detecting singles, $\text{LT}_{\text{singles}}$, efficiency of the particle detectors, and *downscaler*, DS. When a particle triggers the system, it takes some time for the detector and data acquisition process the signal and recover. This creates a *deadtime* in the system during which another particle will not be detected. The singles livetime is found by dividing the number of total S800 triggers for all particles by the S800 scaler, which is not affected by the deadtime. The downscaler is applied to the data acquisition to reduce the number of S800 singles events recorded by the factor DS, while all coincidences are taken. The data acquisition was triggered whenever a downscaled S800 single or a particle-γ coincidence

occurred. The efficiency of the object scintillator and CRDCs were >99.9% relative to the ion chamber, which is assumed to be 100% efficient. With these considerations, N_{beam} is

$$N_{\mathrm{beam}} = \frac{N_{\mathrm{trigger}}\mathrm{DS}}{\mathrm{LT}_{\mathrm{singles}}}. \tag{4.14}$$

N_γ is the number of γ rays in the Coulomb-excitation peak. This number needs to be corrected for the efficiency of the γ-ray detection and the livetime for detecting a particle and a γ ray in coincidence, $\mathrm{LT}_{\mathrm{coinc}}$. The coincidence livetime is calculated in a similar manner to the singles livetime: the S800 coincidence trigger is divided by the coincidence scaler. Taking in these factors, the number of Coulomb-excitation γ rays, N_{Coulex} is

$$N_{\mathrm{Coulex}} = \frac{N_\gamma}{\epsilon \mathrm{LT}_{\mathrm{coinc}}}, \tag{4.15}$$

where ϵ is the efficiency of SeGA at the γ-ray energy of interest and is discussed in Section 4.1.3.2.

N_{Coulex} can also be determined from the scale factors from the fits of simulations to data. The scale factors p_{Cr} and p_{Au} from the fits presented in Section 4.2 were used to extract N_{Coulex}:

$$N_{\mathrm{Coulex}} = \frac{p_x N_{\mathrm{sim}}}{\mathrm{LT}_{\mathrm{coinc}}}, \tag{4.16}$$

where x is either 'Cr' or 'Au', N_{sim} is the number of simulated events.

There were several advantages to using the simulation approach including the ability to account for the excited-state lifetime, γ-ray angular distribution, and γ-ray attenuation in the target and surrounding infrastructure. The effects of the excited-state lifetime on the γ-ray spectrum are discussed in Section 4.3.2.2.

Projectile	Target	$LT_{singles/coinc}$	DS	p_x	N_{target}	N_{beam}
^{58}Cr	^{197}Au	0.998/0.972	100	0.0158(15)	7.7×10^{20}	1.2×10^{8}
^{60}Cr	^{197}Au	0.998/0.972	100	0.0113(77)	7.7×10^{20}	7.0×10^{7}
^{62}Cr	^{209}Bi	0.999/0.983	100	0.00613(48)	7.0×10^{20}	2.6×10^{7}

Table 4.5: Quantities used to calculate experimental cross-sections. p_x are the scale factors for simulations with 1000000 events fit to spectra with safe-angle cuts applied.

The Coulomb-excitation cross sections as a function of θ_{max} are presented in Figures 4.28, 4.29, 4.30, 4.31 and 4.32 below. The uncertainties in the cross sections are statistical uncertainties involved in counting the beam particles, dimensions of the targets, simulation efficiency, uncertainty in the source activity, and uncertainty in the scaling parameter from the fit.

As a function of θ_{max}, the cross section increases essentially linearly, as shown in Figure 4.33, and should be independent of the SeGA ring; however, in each case, one of the rings was not able to be used. This will be discussed further in Section 4.3.2.

4.3.2 $B(E2)$ Values and $|M_n/M_p|$ Values

4.3.2.1 $B(E2)$ values from Coulomb excitation

$B(E2)$ values were calculated from the cross sections presented in Section 4.3.1 using Equation 2.21, which is implemented in the Mathematica program described in [41]. The $B(E2)$ values calculated as a function of θ_{max} are presented in Figures 4.34, 4.35, 4.36, 4.37, and 4.38.

The $B(E2)$ values should be independent of the SeGA ring and θ_{max}, until $\theta_{max} = \theta_{max}^{safe}$. However, it was observed that, except for the case of the gold target excited by ^{58}Cr, one ring in each case could not be used. This was due to background contamination from either the

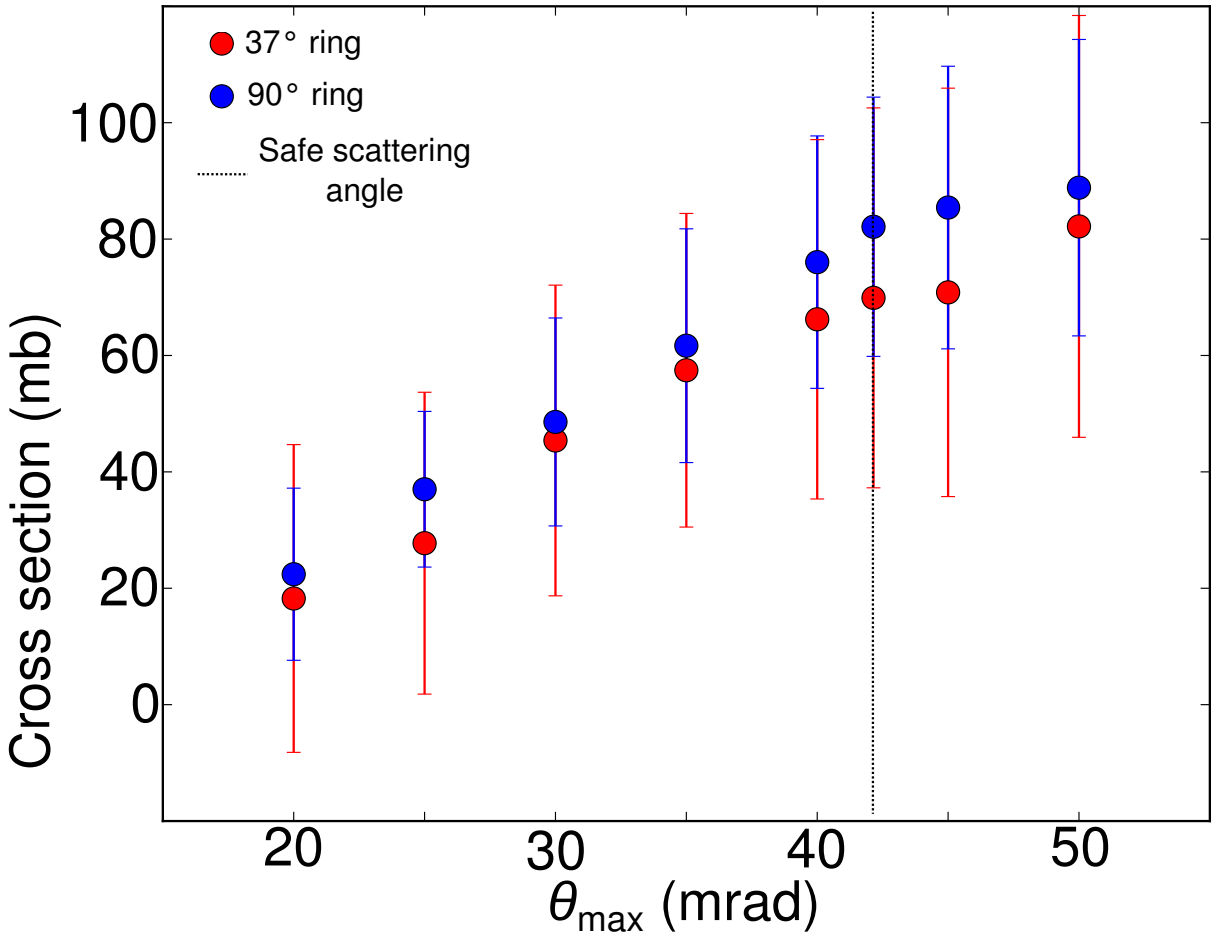

Figure 4.28: Cross sections versus $\theta^{\text{lab}}_{\text{max}}$ for Coulomb excitation of the $7/2^+$ state of the ^{197}Au target by the ^{58}Cr beam. $\theta^{\text{lab}}_{\text{max}}$ for safe Coulomb excitation was 42.15 mrad in this case.

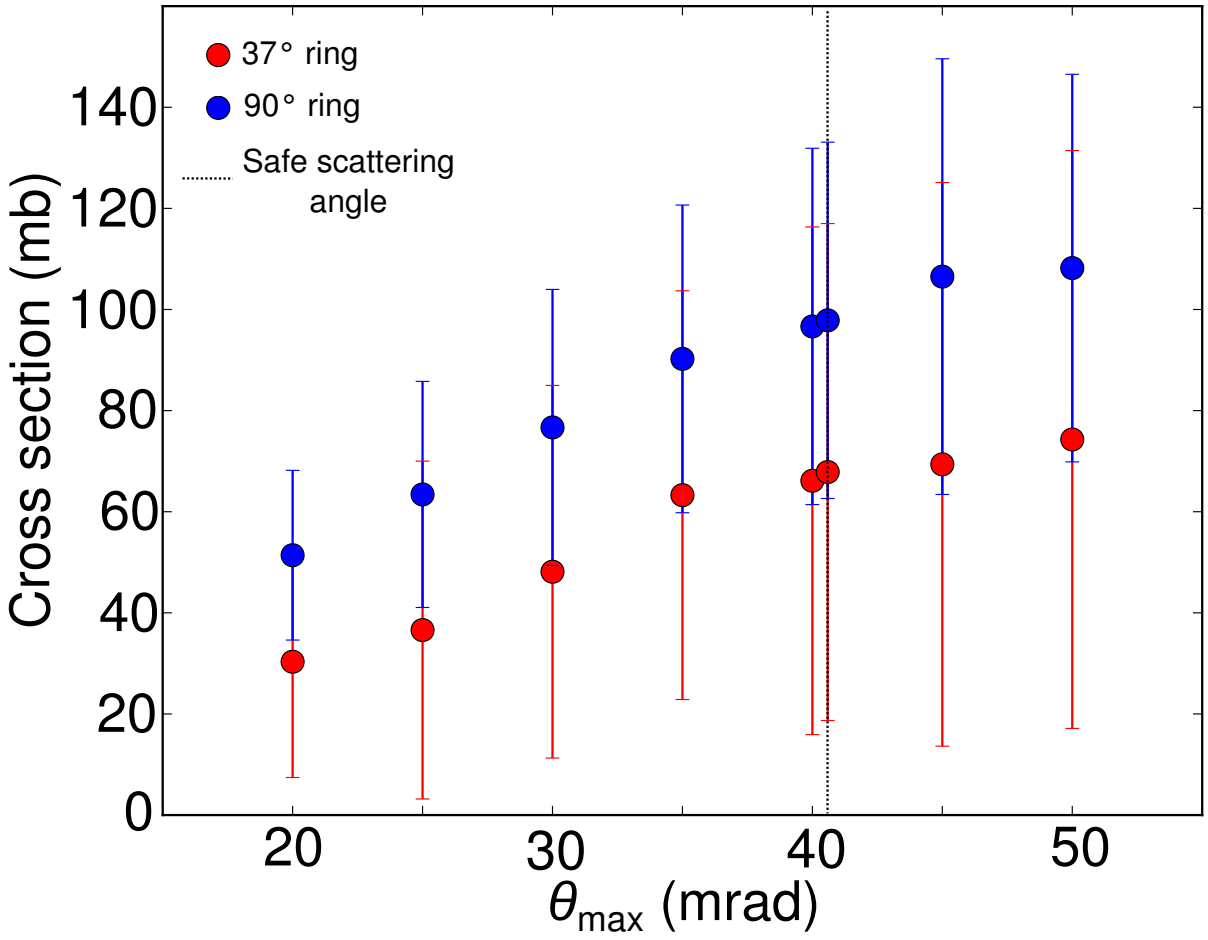

Figure 4.29: Cross sections versus $\theta^{\text{lab}}_{\text{max}}$ for Coulomb excitation of the $7/2^+$ state of the ^{197}Au target by the ^{60}Cr beam. $\theta^{\text{lab}}_{\text{max}}$ for safe Coulomb excitation was 40.59 mrad in this case.

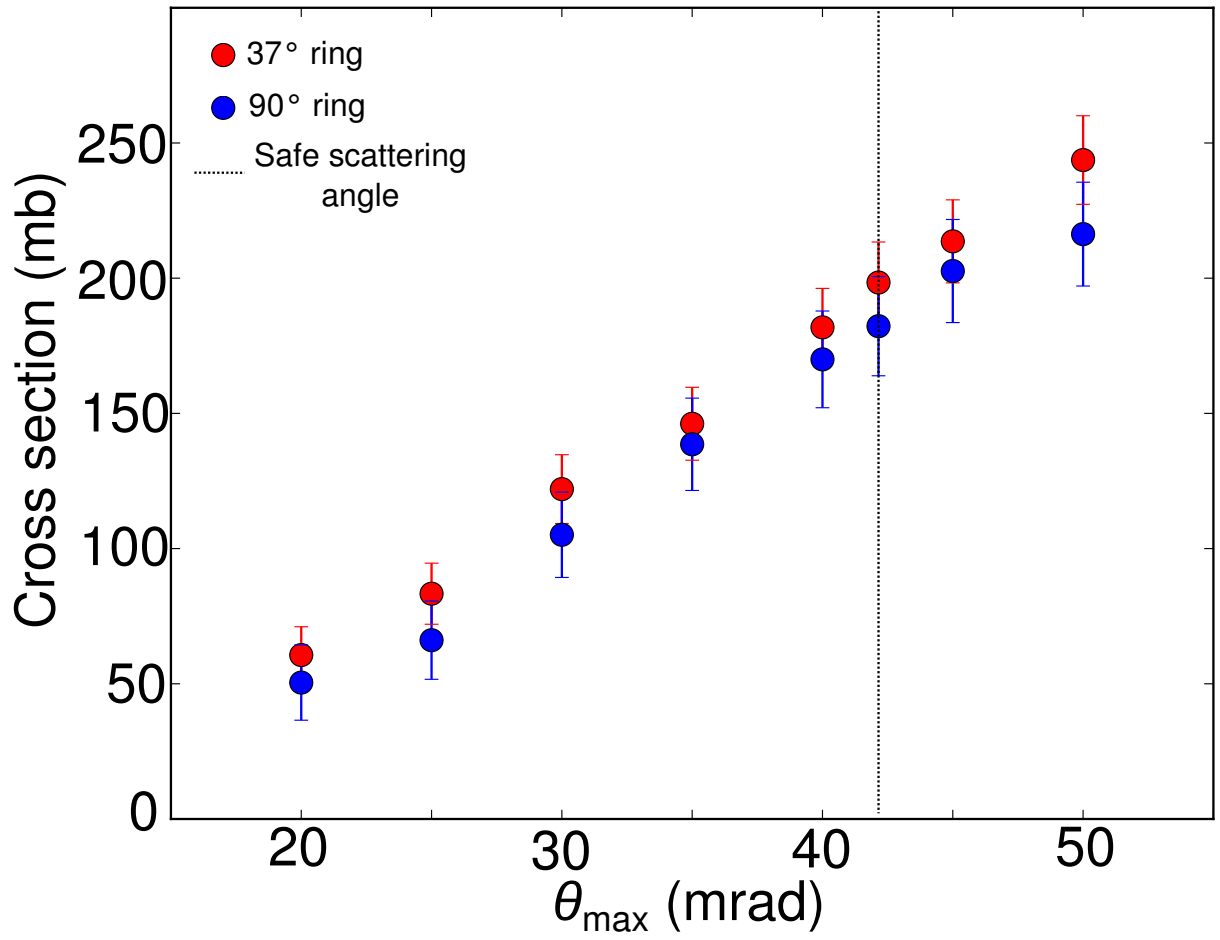

Figure 4.30: Cross sections versus $\theta^{\mathrm{lab}}_{\mathrm{max}}$ for Coulomb excitation of the 2^+ state of the ^{58}Cr beam by the ^{197}Au target. $\theta^{\mathrm{lab}}_{\mathrm{max}}$ for safe Coulomb excitation was 42.15 mrad in this case.

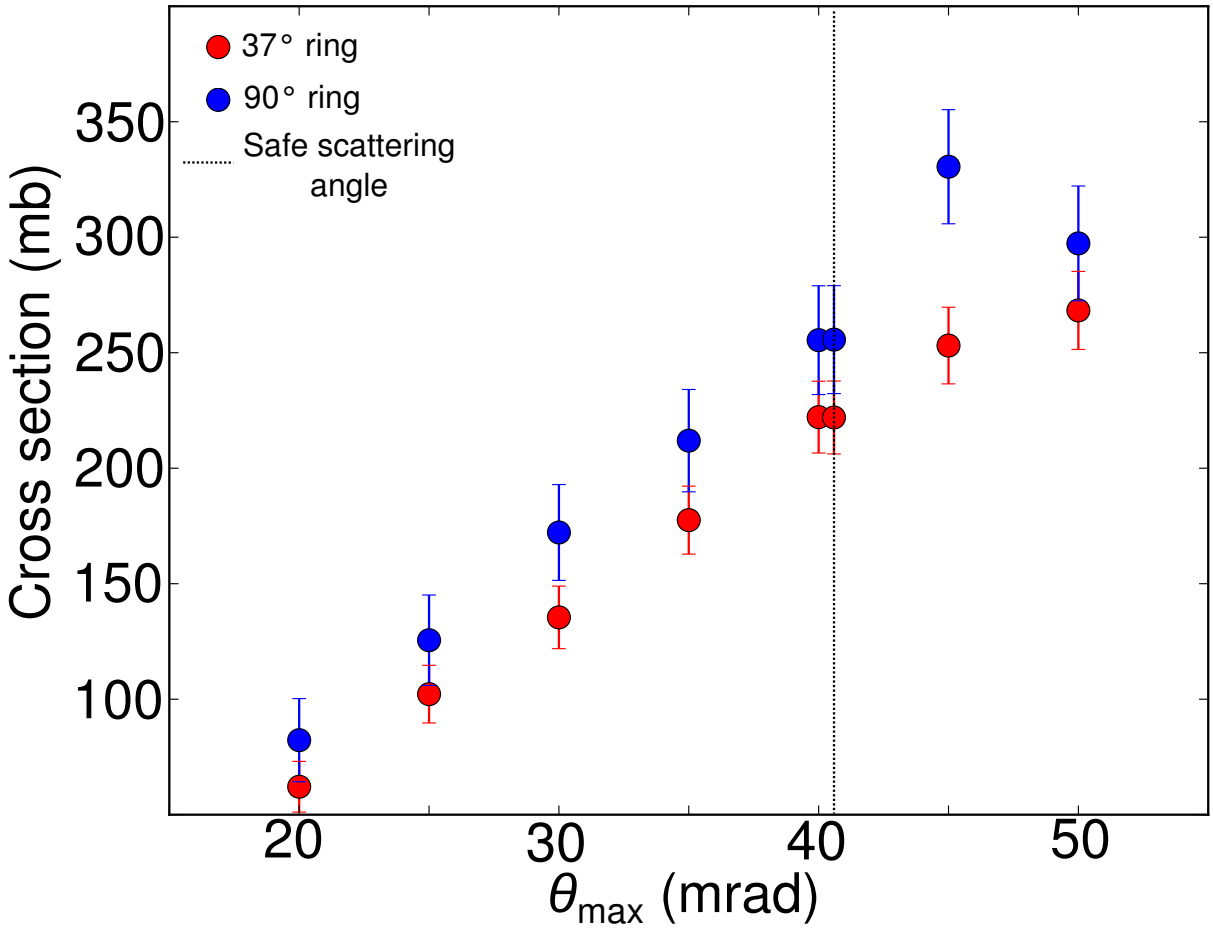

Figure 4.31: Cross sections versus $\theta_{\mathrm{max}}^{\mathrm{lab}}$ for Coulomb excitation of the 2^+ state of the ^{60}Cr beam by the ^{197}Au target. $\theta_{\mathrm{max}}^{\mathrm{lab}}$ for safe Coulomb excitation was 40.59 mrad in this case.

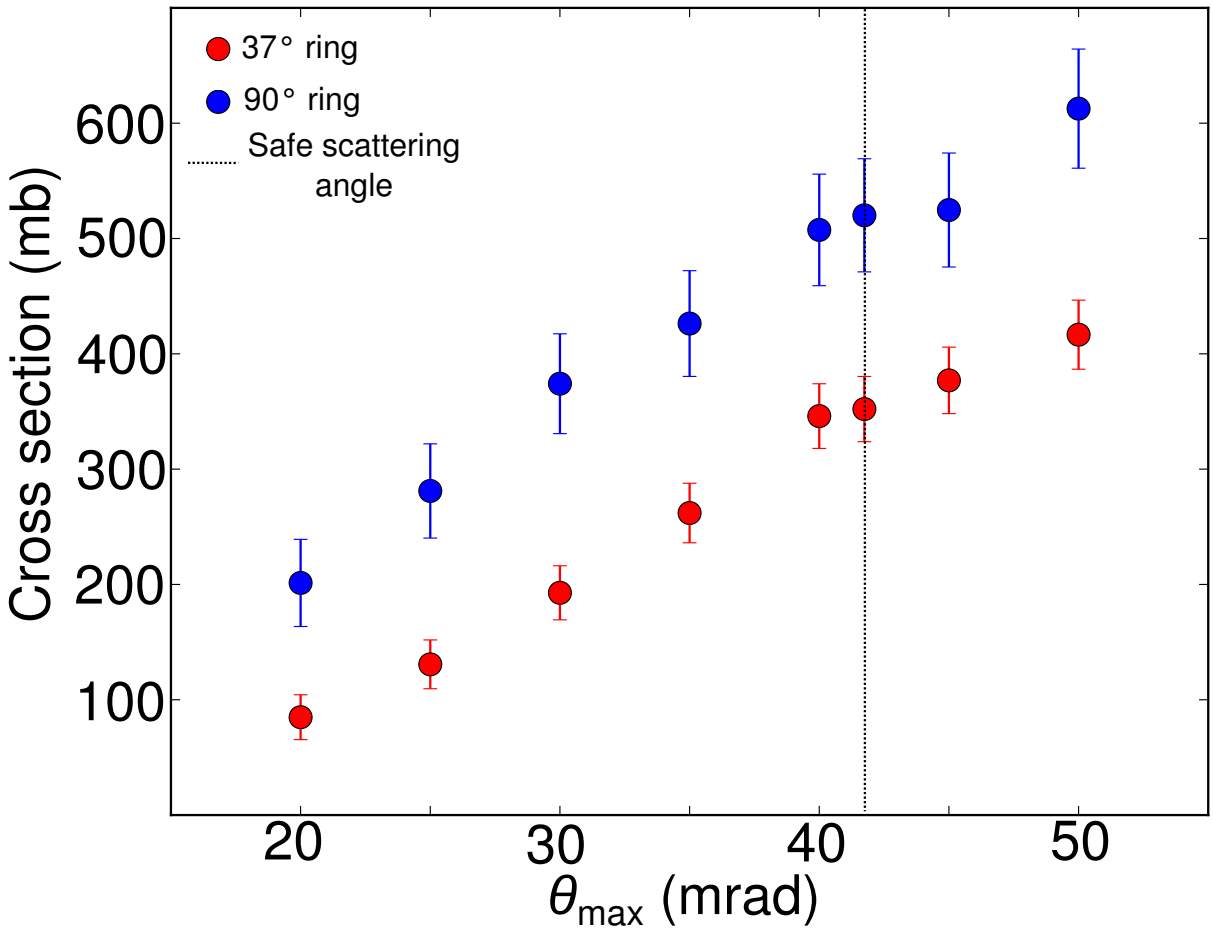

Figure 4.32: Cross sections versus $\theta^{\text{lab}}_{\text{max}}$ for Coulomb excitation of the 2^+ state of the ^{62}Cr beam by the ^{209}Bi target. $\theta^{\text{lab}}_{\text{max}}$ for safe Coulomb excitation was 41.74 mrad in this case.

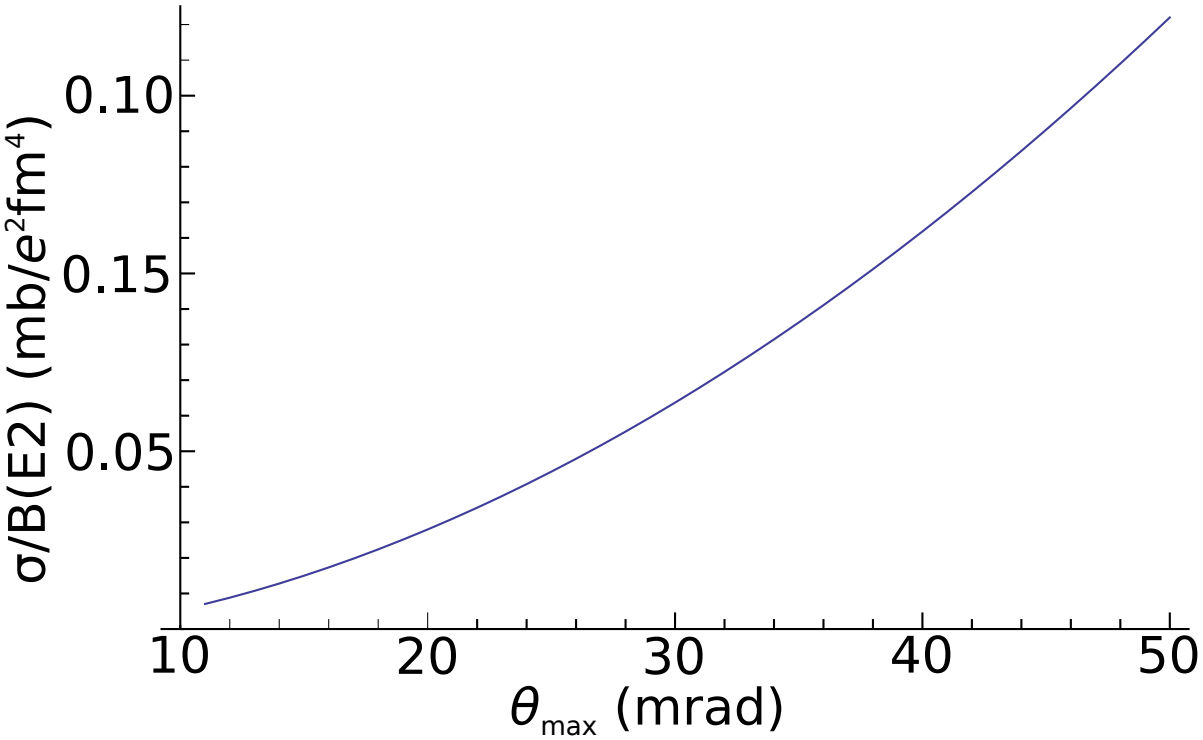

Figure 4.33: Integrated Coulomb-excitation cross section per unit $B(E2)$ versus $\theta_{\max}$ calculated for ^{58}Cr. Between 20 and 50 mrad the behavior is essentially linear.

Doppler-shifted Coulomb excitation peak or the Doppler-corrected room or beam-induced background. This contamination can be seen in Figures 4.25, 4.26 4.22, 4.23, and 4.24. In an attempt to account for these background lines, they were simulated and included in the fits of the in-beam spectra, using the scale factors obtained from the fits of the lab-frame spectra; however, this was unsuccessful. For the case of ^{62}Cr, the effect of the background on the spectra was minimized because the target offset for Doppler reconstruction needed to be taken to be further downstream due to the longer lifetime of the excited state. This caused the corrected background lines to form smoother bumps that are more manageable to the fits instead of the jagged ones corresponding to each SeGA slice that are present in the ^{58,60}Cr cases. In the case of ^{62}Cr, the low level of statistics in the peak of the 90° ring prevented reliable fits of the data. Figure 4.39 shows the poor statistics at small scattering-angle cuts.

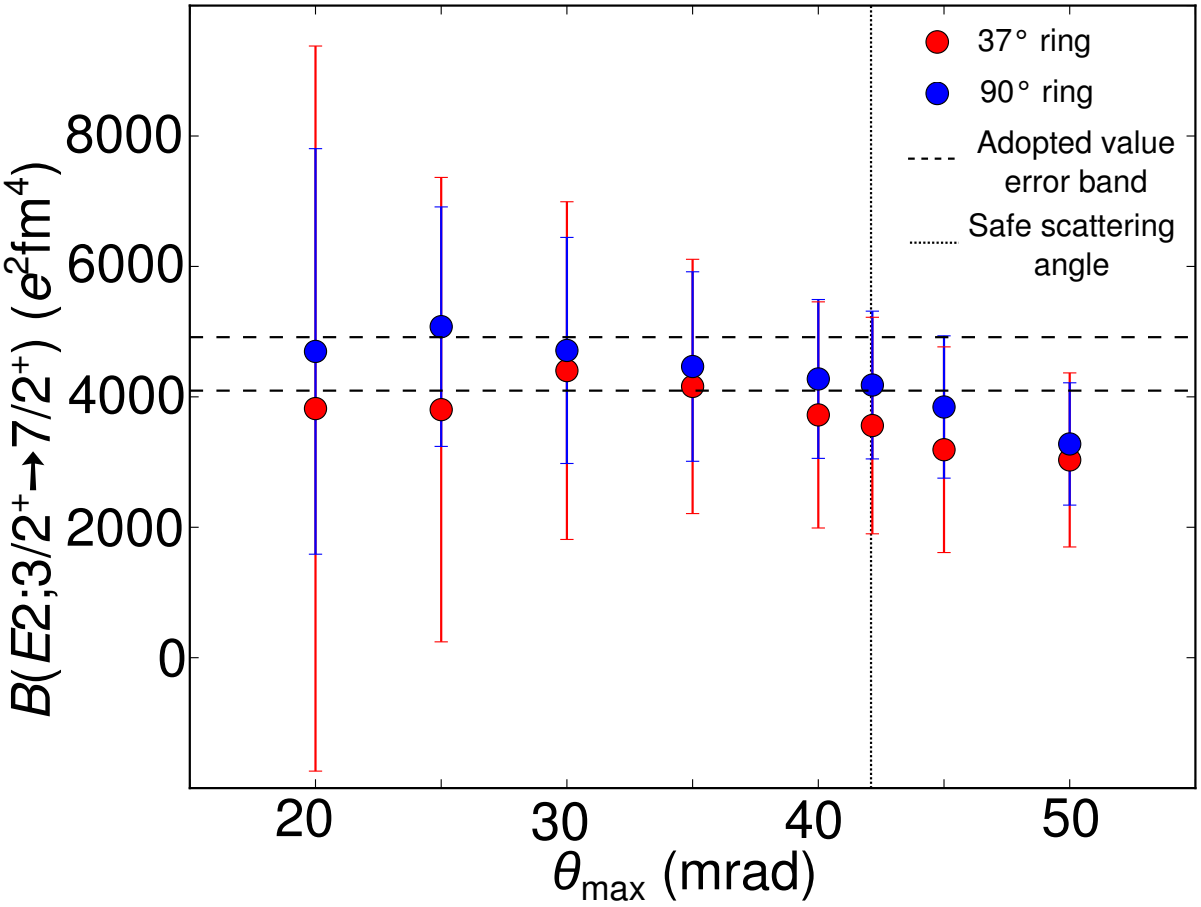

Figure 4.34: $B(E2; 3/2^+ \rightarrow 7/2^+)$ values versus $\theta^{\rm lab}_{\rm max}$ for Coulomb excitation of the ^{197}Au target by the ^{58}Cr beam. $\theta^{\rm lab}_{\rm max}$ for safe Coulomb excitation was 42.15 mrad in this case.

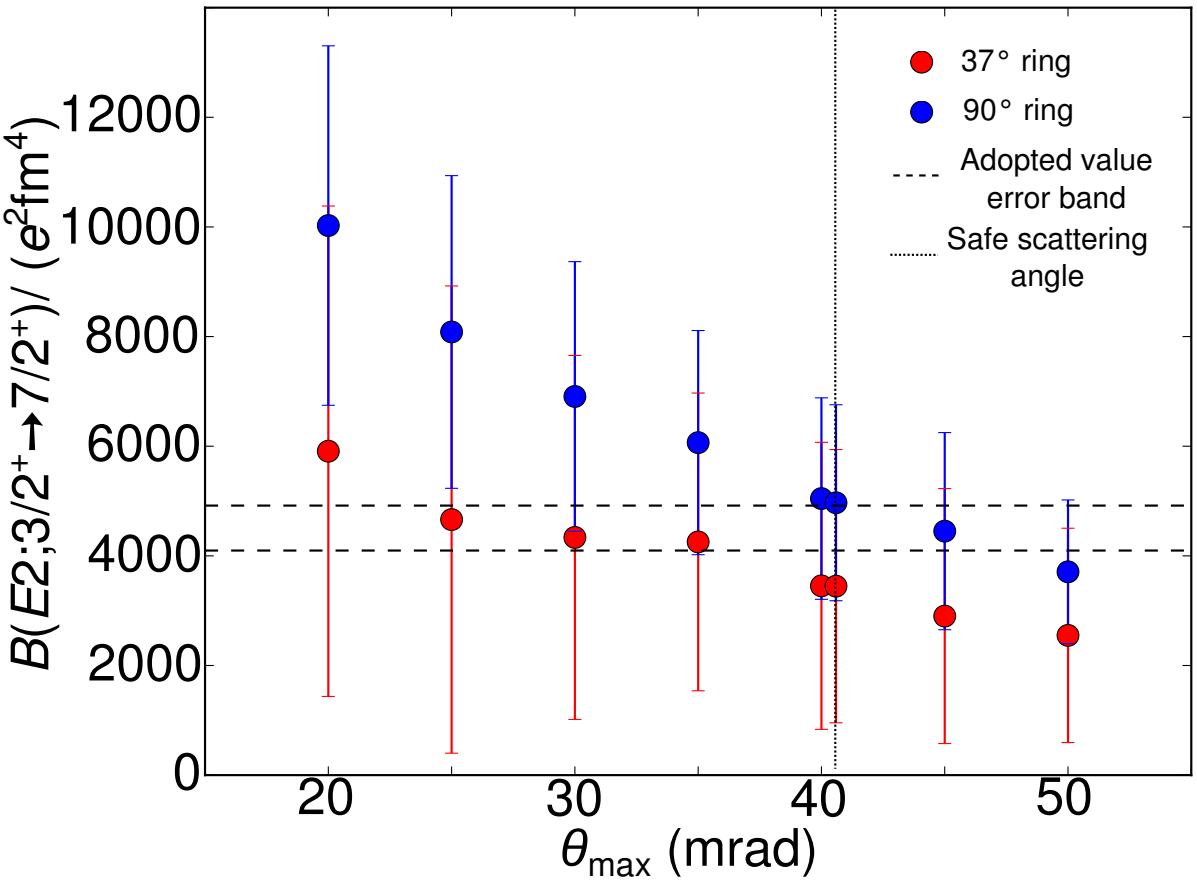

Figure 4.35: $B(E2; 3/2^+ \rightarrow 7/2^+)$ values versus $\theta^{\rm lab}_{\rm max}$ for Coulomb excitation of the ^{197}Au target by the ^{60}Cr beam. $\theta^{\rm lab}_{\rm max}$ for safe Coulomb excitation was 40.59 mrad in this case.

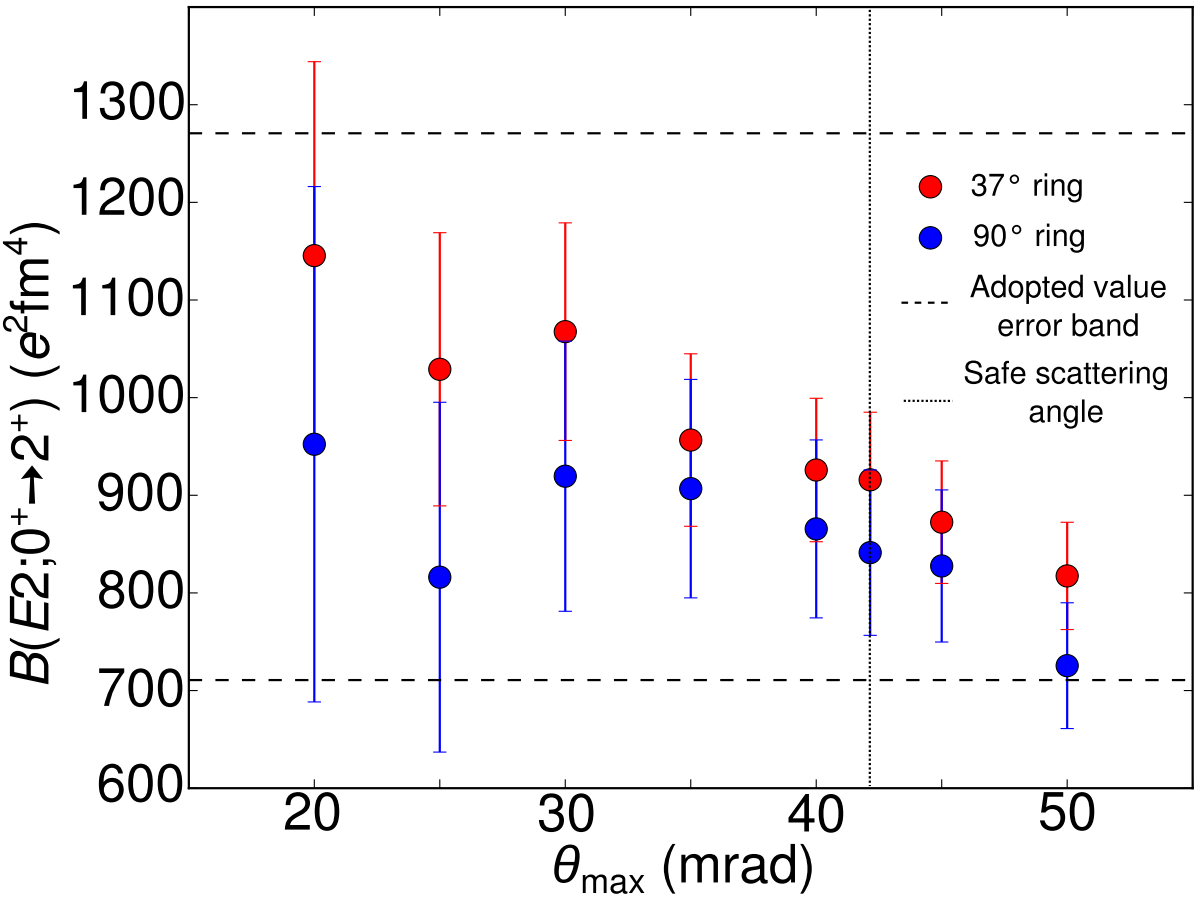

Figure 4.36: $B(E2; 0^+ \rightarrow 2^+)$ values versus $\theta^{\text{lab}}_{\text{max}}$ for Coulomb excitation of the ^{58}Cr beam by the ^{197}Au target. $\theta^{\text{lab}}_{\text{max}}$ for safe Coulomb excitation was 42.15 mrad in this case.

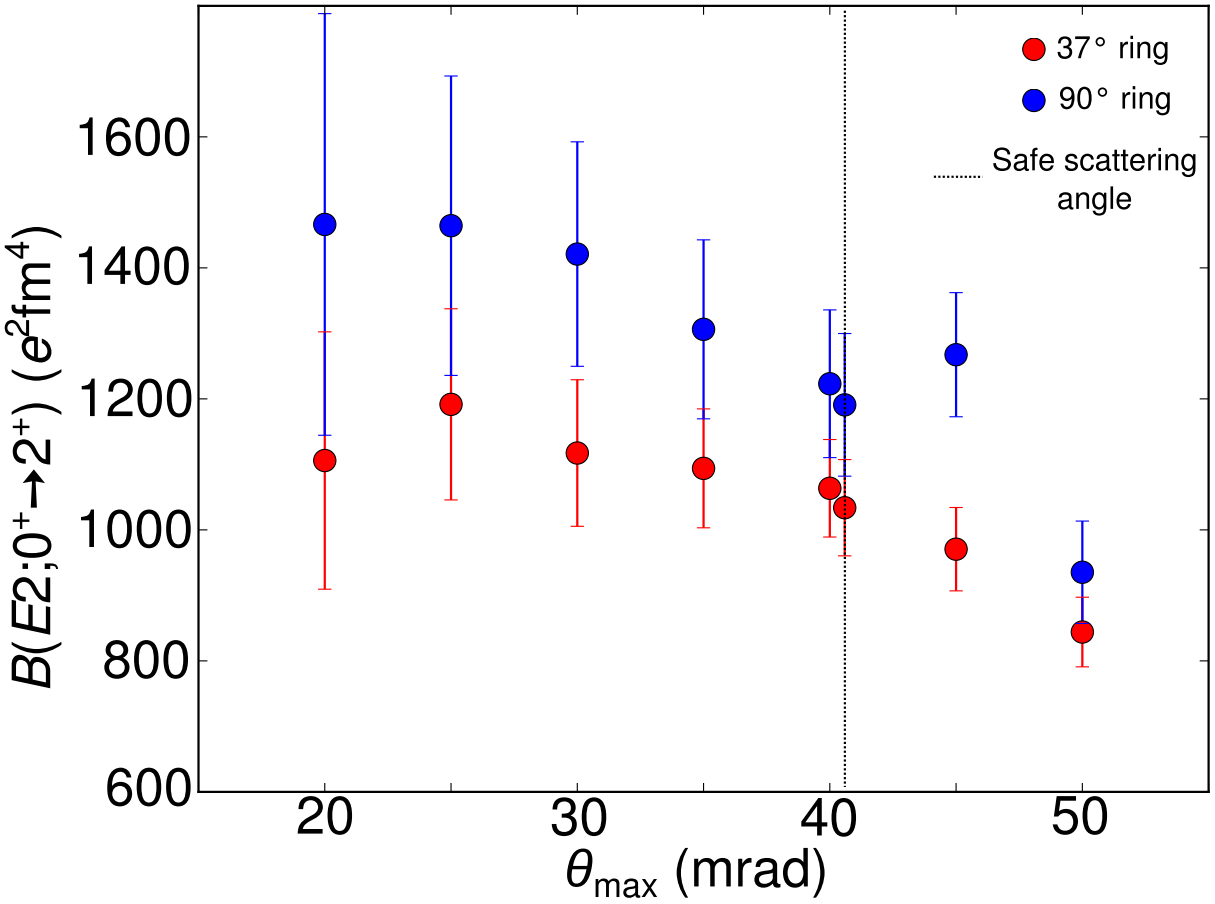

Figure 4.37: $B(E2; 0^+ \rightarrow 2^+)$ values versus $\theta^{\rm lab}_{\rm max}$ for Coulomb excitation of the ^{60}Cr beam by the ^{197}Au target. $\theta^{\rm lab}_{\rm max}$ for safe Coulomb excitation was 40.59 mrad in this case.

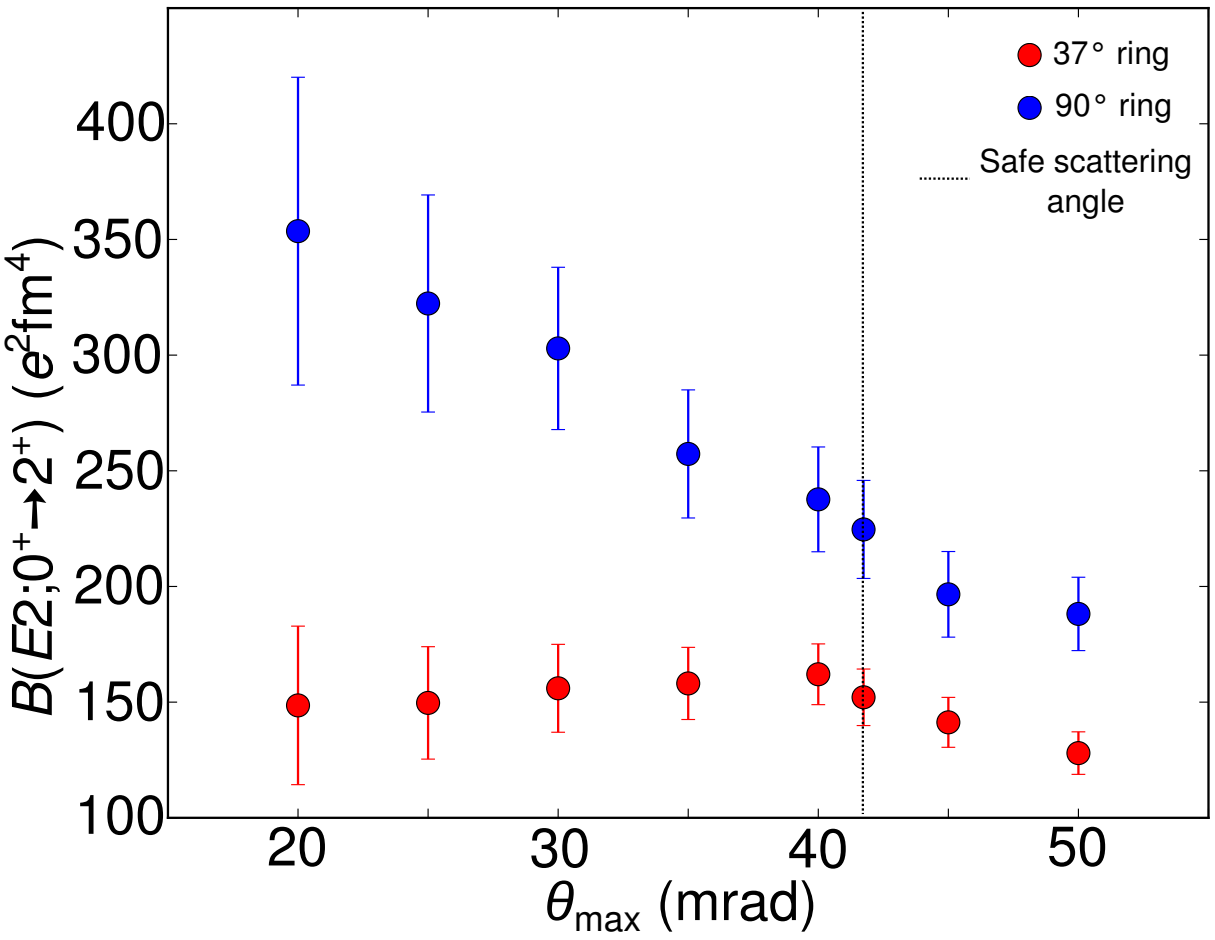

Figure 4.38: $B(E2; 0^+ \rightarrow 2^+)$ values versus $\theta^{\rm lab}_{\rm max}$ for Coulomb excitation of the ^{62}Cr beam by the ^{209}Bi target. $\theta^{\rm lab}_{\rm max}$ for safe Coulomb excitation was 41.74 mrad in this case.

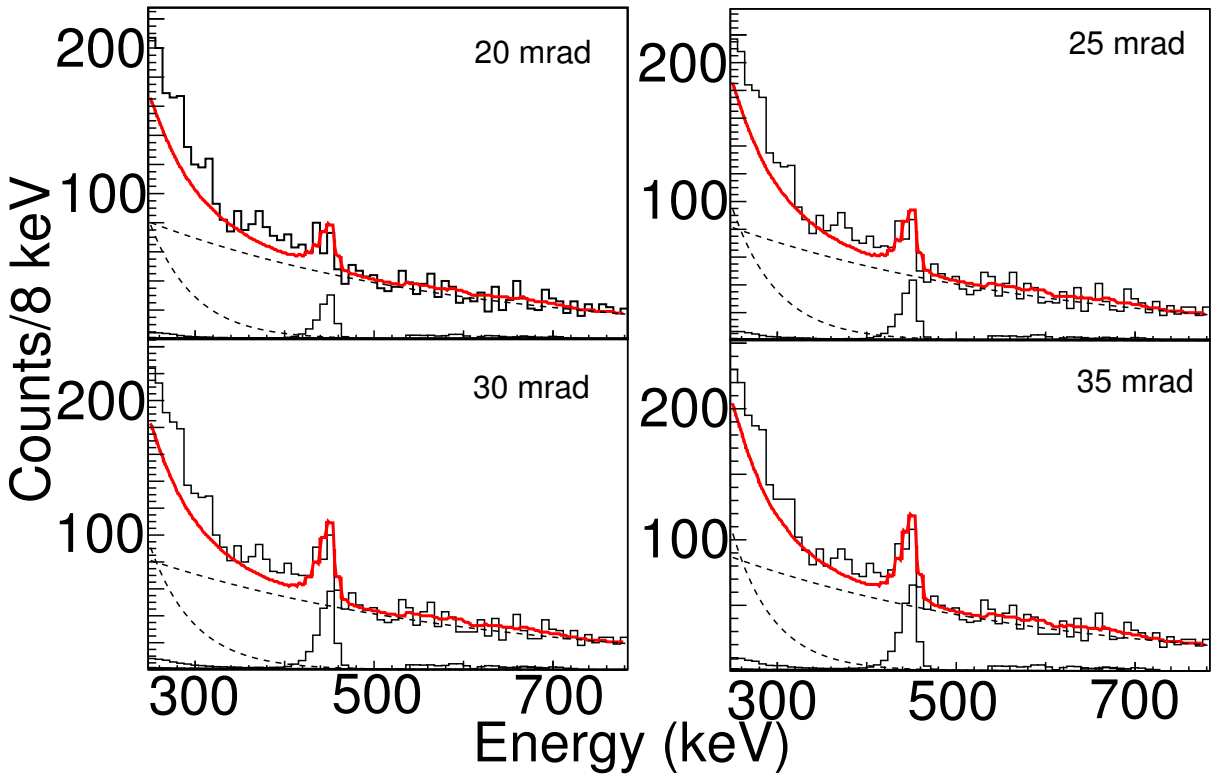

Figure 4.39: The 90° ring in the ^{62}Cr measurement suffered from poor statistics at small scattering-angle cuts. Data from this ring was not used.

Beam	$B(E2;0_1^+ \rightarrow 2_1^+)$ ($e^2\text{fm}^4$) Cr	$B(E2;3/2_1^+ \rightarrow 7/2_1^+)$ ($e^2\text{fm}^4$) ^{197}Au	$\lvert M_n/M_p \rvert$ (N/Z)
^{58}Cr	860(125) 990(280) [78]	4002(610) 4494(410) [89]	
^{60}Cr	1105(145)	3678(910) 4494(410) [89]	0.87(19)
^{62}Cr	1625(220) 1605^{+302}_{-246} [a]		0.89(17)

[a] From the lifetime deduced from the lineshape analysis and with the adopted value of $E(2^+)$=446(1) keV [90] (see Section 4.3.2.2).

Table 4.6: Measured $B(E2)$ values for projectile and target excitations and $|M_n/M_p|$ ratios relative to N/Z.

For the reasons described above, only the 37° ring was used for ^{58,62}Cr and only the 90° ring was used for ^{60}Cr. The results of the Coulomb excitation are presented in Table 4.6.

4.3.2.2 ^{62}Cr Lineshape Analysis

The shape of the ^{62}Cr peak exhibits a pronounced tail on the low-energy side. The tail is caused by the long lifetime, τ, of the excited state. The excited beam particle will decay at some point downstream of where it became excited. If the lifetime is long enough, the particle will travel far enough downstream before it decays to affect the Doppler reconstruction of the γ-ray peak. For example, a particle with velocity $0.3c$ will travel $\sim$ 1 cm in 100 ps. The Doppler reconstruction calculates the angle of emission of the γ ray from the center of the target and segment that registered the largest energy deposit. If the γ ray is emitted

downstream of the target, the actual angle of emission is larger. As a result, the γ-ray energy is underestimated in the Doppler reconstruction, which is visible as a low energy tail like the one seen in Figure 4.15. To exploit this effect and determine the excited-state lifetime, a series of simulations were performed with excited-state lifetimes varying from 70 to 250 ps. The resulting peakshapes were then fit to the measured spectrum using a χ^2 minimization. The resulting best-fit lifetime is shown in Figure 4.40, along with the χ^2 as a function of the simulated level lifetime. The lifetime was determined to be 144^{+27}_{-22}ps. The lifetime of the excited state is related to the $B(E2)$ value by

$$B(E2;\downarrow) = \frac{816}{E_\gamma^5 \tau} e^2\mathrm{fm}^4\mathrm{MeV}^5\mathrm{ps}, \tag{4.17}$$

resulting in a $B(E2;\uparrow)$ value of 1605^{+302}_{-246} $e^2\mathrm{fm}^4$, in agreement with the cross section method (See Table 4.6). This lifetime result lends confidence to the cross section result since consistent $B(E2)$ values were obtained using different methods.

4.3.3 Comparison with Theory and Conclusions

The $B(E2)$ values determined in this work are plotted versus neutron number in Figure 4.41 along with $B(E2)$ and $E(2_1^+)$ values for even-even Ni, Fe and Cr isotopes. At $N = 28$, all isotopes display the large $E(2_1^+)$ energy and the small transition probability characteristics of a shell closure in even-even nuclei. However, only Ni, with a full $\pi 0f_{7/2}$ orbital, shows these indicators at $N = 40$. The decreasing energy values and increasing transition probabilities in the Fe and Cr chains are taken as direct experimental evidence for the onset of collectivity in the region below ^{68}Ni.

Shell-model calculations were performed using the LNPS shell model effective interaction

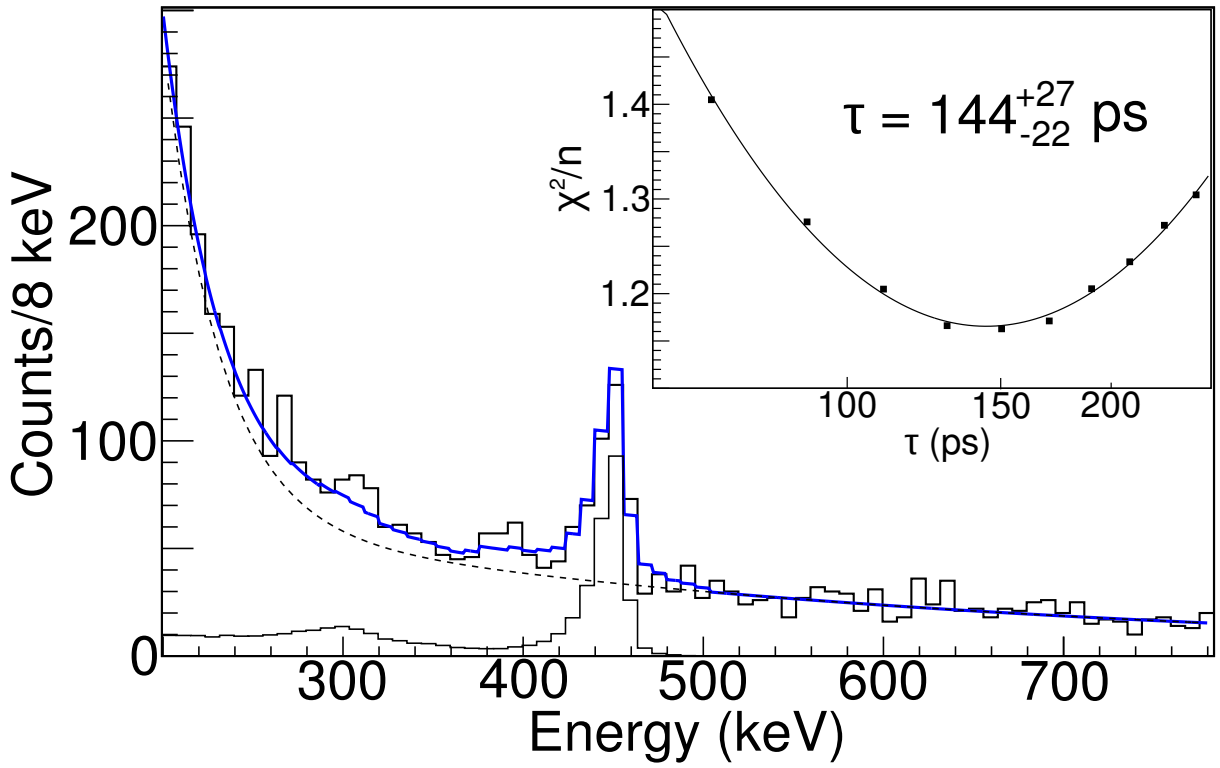

Figure 4.40: Event-by-event Doppler corrected γ-ray spectrum measured in coincidence with ^{62}Cr particles. The low-energy tail is apparent. Overlaid in blue is a fit of the simulated γ-ray response of SeGA for an excited-state lifetime of 144 ps. The background used in the fit is shown as a dashed line. The inset shows the reduced χ^2 of the fit as a function of simulated excited-state lifetime (see text for details).

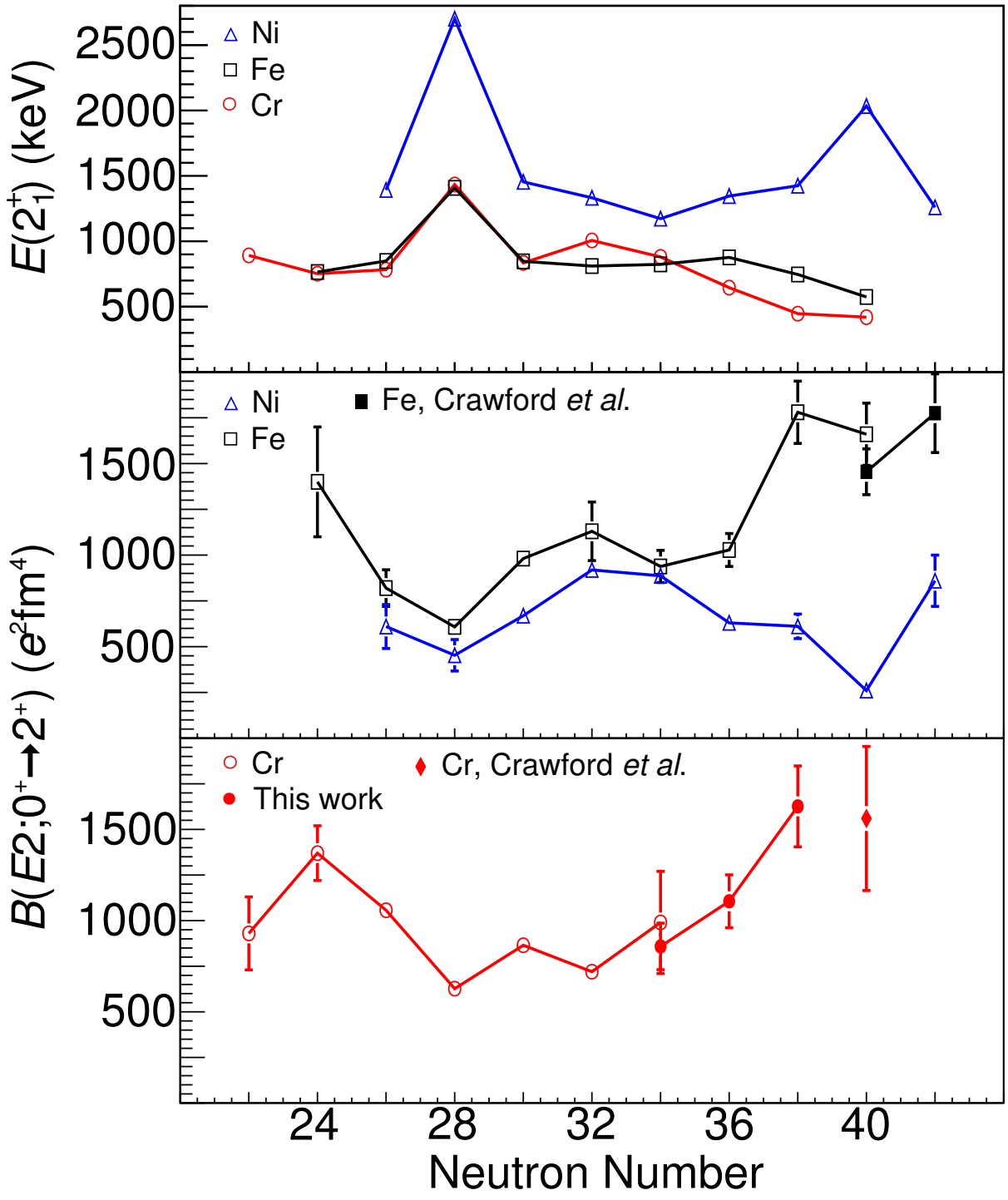

Figure 4.41: Systematics of $E(2_1^+)$ energies (top panel) and $B(E2)$ values for Ni, Fe (middle panel) and Cr (bottom panel) isotopes. Values obtained in the current work are plotted as filled circles. Other data are taken from [91, 92, 37].

in a model-space consisting of the full fp shell for protons and the $1p_{3/2}$, $1p_{1/2}$, $0f_{5/2}$, $0g_{9/2}$, and $1d_{5/2}$ orbitals for neutrons [40]. For comparison, two additional sets of calculations were carried out using the well-established GXPF1A effective interaction [22, 23] and LNPS restricted to the fp shell for both protons and neutrons. The results with the GXPF1A and restricted LNPS, hereafter denoted LNPS-fp, calculations were found to be nearly identical. In order to provide a consistent comparison between the fp and $fpg_{9/2}d_{5/2}$ valence spaces, we will refer to the LNPS-fp and LNPS interactions in the following.

The calculations are confronted with the experimental $B(E2; 0^+ \rightarrow 2^+)$ values in Figure 4.42. The $B(E2)$ probabilities for ^{58,60,62}Cr in Figure 4.42(a) originate from this work and those quoted for ^{62,64,66}Fe (Figure 4.42(b)) were taken from Reference [76]. The trend of the theoretical $B(E2)$ values calculated using the LNPS amplitudes with the standard effective charges, $e_p = 1.5$, $e_n = 0.5$, correspond to the dashed line with open circles in Figure 4.42(a). They agree with the trend exhibited by the Cr data, but the magnitude is over-predicted by 40-50%. For the iron data, the LNPS calculations with standard effective charges (dashed line with open circles in Figure 4.42(b)) agree at $N = 38$, but again over-predict the $B(E2)$ values at $N = 36$ and $N = 40$. Using slightly reduced effective charges of $e_p = 1.4$ and $e_n = 0.4$ improves the overall agreement for both isotopic chains, although the calculations fail to describe the enhancement at $N = 38$ in the evolution of the $B(E2)$ values in the Fe chain. At the time of this experiment and data analysis, the $B(E2)$ value of the key nucleus ^{64}Cr was not known, but with these modified effective charges, the $B(E2)$ value of ^{64}Cr was predicted to be $B(E2; 0^+ \rightarrow 2^+)$=1770 e^2fm^4. This prediction was recently confirmed by Crawford *et al.* via intermediate-energy Coulomb excitation [37]. As expected, a clear difference can be seen between the LNPS-fp and LNPS results. With increasing neutron number, excitations across the $N = 40$ gap become increasingly important. These excitations account for the

onset of collectivity observed above $N = 36$ in the Cr isotopes, with large, nearly identical $B(E2)$ values predicted for ^{62}Cr and ^{64}Cr. In contrast, the LNPS-fp calculations follow the opposite trend, with $B(E2)$ values declining with increasing neutron number, reflecting the absence of the crucial $\nu 0g_{9/2}$ and $\nu 1d_{5/2}$ orbitals from the model space.

In the cases of ^{60,62}Cr, where data on (p, p') scattering were available from experiments at RIKEN [79], $|M_n/M_p|/(N/Z)$ ratios were calculated following the method of Riley *et al.* [93], which is described in Section 1.3.2. The resulting $|M_n/M_p|$ ratios are presented in Table 4.6 The $|M_n/M_p|/(N/Z)$ values for ^{60,62}Cr are also compared with the calculations in Figure 4.42(c).

The measured $|M_n/M_p|$ values for both are around 0.9 (N/Z), indicating that the low-lying excitations follow the simple picture of protons and neutrons having the same deformation lengths with only a slight proton dominance relative to the simple hydrodynamical limit of N/Z. The LNPS calculations in the $fpgd$ space are consistent with these extracted ratios. In contrast, the LNPS-fp calculations predict a decreasing ratio towards $N = 40$, reflecting the occurrence of an $N = 40$ shell gap and highlighting again the inadequacy of the limited neutron model space in this Hamiltonian. All these observations are consistent with previous work that has demonstrated that the fp model-space alone is inadequate to fully describe the low-lying structure in Cr isotopes heavier than ^{58}Cr because of the ever increasing role of the $0g_{9/2}$ and $1d_{5/2}$ neutron orbitals [69, 77, 74, 81, 94]. In the LNPS effective interaction, the probability of neutron excitations to the $\nu 0g_{9/2}$ and $\nu 1d_{5/2}$ orbitals increases, going from $2p-2h$ excitations in ^{60}Cr to configurations dominated by $4p-4h$ excitations in ^{64}Cr, with sizable contributions of $6p-6h$ [40].

Effective charges enter sensitively in the calculation of the theoretical transition strengths since $B(E2) = (e_p A_p + e_n A_n)^2/(2J_i + 1)$, where A_p and A_n are the proton and neutron

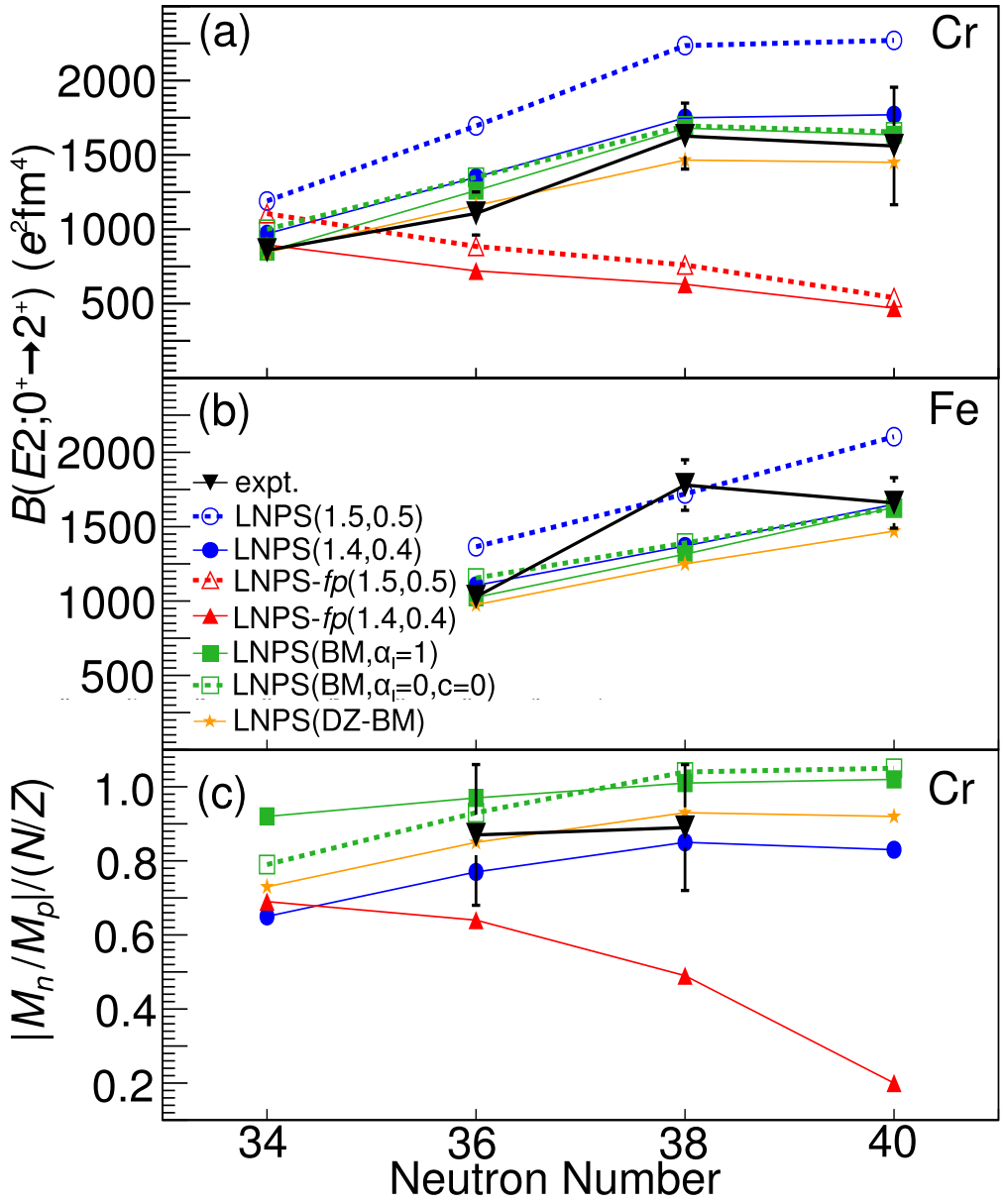

Figure 4.42: Comparison of measured $B(E2)$ transition strengths for Cr (a) and Fe isotopes (b), and ratios of $|M_n/M_p|$ relative to N/Z (c) with shell-model calculations. Shell-model calculations were performed using the LNPS [40] effective interaction in both the full model-space, which included the $0g_{9/2}$ and $1d_{5/2}$ orbitals for neutrons, (labeled LNPS), and a model-space limited to the pf shell only (labeled LNPS-fp). The different choices of effective charges are indicated (see text for details). The experimental $B(E2)$ value for ^{64}Cr is from [37].

shell-model amplitudes. The choices for e_p and e_n assumed for the discussion above are isoscalar and taken as constant across the isotopic chain. Effective charges compensate for missing excitations outside of the restricted shell model space and it is not clear that the assumption of constant effective charges is valid throughout the entire model space. Bohr and Mottelson proposed N- and Z-dependent (isovector) effective $E2$ polarization charges that approximate the coupling to quadrupole modes outside of the model spaces of the effective interactions [24, 95]. In the following, we use the Bohr-Mottelson (BM) formulation of the effective charges for the $B(E2) \sim M_p^2$ values as well as for the ratio of the proton and neutron transition matrix elements: $M_p = A_p(1 + \delta e_p) + A_n \delta e_n$ and $M_n = A_n(1 + \delta e'_n) + A_p \delta e'_p$, $\delta e_{p/n}$ and $\delta e'_{p/n}$ are the polarization charges following Bohr and Mottelson ($a = 1$, $b = -0.32$, $c = 0.32$ and $d = -0.65$) :

$$\delta e_{n/p} = a\frac{Z}{A} \pm c + \alpha_I[b\frac{N-Z}{A} \pm d\frac{Z}{A}\frac{N-Z}{A}] \quad (4.18)$$

$$\delta e'_{p/n} = a\frac{N}{A} \pm c - \alpha_I[b\frac{N-Z}{A} \pm d\frac{N}{A}\frac{N-Z}{A}]. \quad (4.19)$$

These expressions use an additional parameter, α_I, that scales the $(N - Z)$-dependent part so that $\alpha_I = 1$ gives the full BM values and $\alpha_I = 0, c = 0$ reduces it to the isoscalar part. Figure 4.42 shows the $B(E2)$ values and $|M_n/M_p|$ ratios calculated from the shell model using the BM effective charges for $\alpha_I = 1$ and $\alpha_I = 0, c = 0$. The calculations with the isovector $\mathrm{BM}_{\alpha_I=1}$ polarization charges reproduce the Cr $B(E2)$ values within the experimental uncertainties with only small differences at $N = 34$ and 36 with respect to the isoscalar, $\alpha_I = 0, c = 0$, case. For the Fe isotopes, the differences between $\alpha_I = 0, c = 0$ and $\alpha_I = 1$ are even smaller and the results closely follow the calculations with constant effective charges $(e_p, e_n) = (1.4, 0.4)$. Significant differences become apparent for the $|M_n/M_p|$ ratios

where the isoscalar and isovector BM polarization charges lead to differences of 15% for ^{58}Cr, where proton scattering data are unfortunately not available to deduce this quantity from experiment. While the differences between $(e_p, e_n) = (1.4, 0.4)$, BM$_{\alpha_I=1}$ and BM$_{\alpha_I=0}$ are very small for the $B(E2)$ values, $|M_n/M_p|$ reveals significant potential to discriminate between the three different choices, with ^{58}Cr being most sensitive to the isovector part of the BM formulation and $(e_p, e_n) = (1.4, 0.4)$ values resulting consistently in significantly lower ratios across the isotopic chain.

As a next step we try to constrain the effective charges more microscopically and start with the $\delta e_{p/n}$ values proposed from dedicated shell-model studies [27, 96] and evolve them as a function of $(N - Z)$ using the BM presctiption. Dufour and Zuker (DZ) [27] obtain $(e_p, e_n) = (1.31, 0.46)$ in agreement with (1.36(5),0.45(5)) deduced for the USD Hamiltonians [96]. Assuming that these values are good starting points at $N \sim Z$, we replace $aZ/A \pm c$ and $aN/A \pm c$ by constants so that $\delta e_p = \delta e'_n = 0.31$ and $\delta e_n = \delta e'_p = 0.46$ at $N = Z$. With this strategy and $\alpha_I = 0.8$ in Eq.(1) and (2) and b and d from BM, the Cr and Fe $B(E2)$ values as well as the available $|M_n/M_p|$ ratios are described well. They are labeled LNPS (DZ-BM) in Figure 4.42. The same calculation performed using the USD effective charges as $N = Z$ starting points, instead of DZ gives results that agree within 5% or less with DZ (not shown). Again, although the $B(E2)$ values differ very little within the different scenarios discussed here for the effective charges, the $|M_n/M_p|$ ratios emerge as a quantity that can discriminate between the various approaches. In any event, the LNPS shell-model calculations of the $B(E2)$ values are very robust and rather consistently predict $B(E2; 0^+ \rightarrow 2^+) \sim 1600$ e^2fm^4 for the $N = 40$ key nucleus ^{64}Cr within 10%. Since the publication of [64], the $B(E2)$ value for ^{64}Cr has been measured [37] and the $B(E2; 0^+ \rightarrow 2^+)$ value of 1561(396) e^2fm^4 is consistent with the calculations presented here.

In summary, intermediate-energy Coulomb excitation of ^{58,60,62}Cr was performed and $B(E2;0^+ \rightarrow 2^+)$ values were deduced from the measured cross sections. For ^{62}Cr, the $B(E2)$ excitation probability was also determined independently from a lifetime measurement that used a γ-ray line-shape analysis. Large-scale shell-model calculations with the LNPS effective interaction in a model space that includes the $0g_{9/2}$ and $1d_{5/2}$ orbitals for neutrons describe the trend of the data, but overestimate the magnitude of the quadrupole transition strengths when using the standard effective charges. Different choices of modified effective charges have been used to describe the onset of collectivity in the chromium isotopes approaching $N = 40$, with the robust prediction emerging for the $B(E2;0^+ \rightarrow 2^+)$ value for the important nucleus ^{64}Cr having been confirmed in [37]. Non-standard sets of effective charges were shown to provide an improved description of the known $B(E2)$ values in the Fe nuclei. The ratio of the neutron and proton transition matrix elements $|M_n/M_p|$, that can be deduced from combined proton scattering and Coulomb excitation data, reveals the potential to discriminate between different sets of effective charges in this model space.

Chapter 5

γ-ray Spectroscopy of ^{63}Mn

The magic numbers for protons and neutrons - well-known near stability - have been observed to change in the exotic regime [13, 65]. One driving force behind this evolution is the proton-neutron tensor interaction [38]. In the region below ^{68}Ni, the N=40 subshell gap has been of particular interest. An N=40 gap was suggested based on the large 2^+ energy and small $B(E2)$ value of ^{68}Ni [36]; however, removing protons from ^{68}Ni quickly reveals collectivity in the iron and chromium isotopes [37, 64, 76].

Between iron and chromium lie the (Z = 25) manganese isotopes. The neutron-rich, odd-even isotopes ^{59,61,63}Mn were studied via multi-nucleon transfer by Valiente-Dobón *et al.* [97] and ^{61}Mn via β decay by Crawford *et al.* [98]. Aside from the $7/2^- \rightarrow 5/2^-$ transition to the ground state, relatively little is known about the structure of ^{63}Mn. A handful of unplaced transitions were seen in β decay by Gaudefroy *et al.* [99], but poor statistics and a large branching ratio directly to the ground state prevented the construction of a level scheme. Various shell-model calculations using the GXPF1A [22, 23] and *fpg* [36] effective interactions reproduce the energy of the $7/2^-$ state in ^{63}Mn to a reasonable degree, for example, in [97, 98]. Beyond this, there are larger differences in the level densities below 1 MeV, particularly in [98]. Experimental information on the transition probabilities in ^{63}Mn has not been available to this point. The results on the in-beam γ-ray spectroscopy of ^{63}Mn reported on here, combined with state-of-the-art shell-model calculations [40], provide further

evidence for the influence of the $0g_{9/2}$ and $1d_{5/2}$ neutron orbitals in this region.

5.1 Experiment

The beam production and experimental setup for the spectroscopy of ^{63}Mn was identical to the setup for the Coulomb excitation of ^{58,60,62}Cr described in Chapters and , so only a brief description will be given here. A primary beam of ^{76}Ge was accelerated at the NSCL Coupled Cyclotron Facility [47] to induce projectile fragmentation at 130 MeV/nucleon on a 493-mg/cm^{2}Be target. The resulting cocktail beam was purified in the A1900 fragment separator [48] with a 240-mg/cm^2 Al wedge to produce a secondary beam containing ^{63}Mn. The secondary beam was delivered to a 370-mg/cm^2 ^{9}Be target located at the target position of the S800 magnetic spectrograph [57] with an energy of 84 MeV/nucleon and a momentum acceptance of 2.5%.

Surrounding the target was the Segmented Germanium Array (SeGA) [62] in the "classic" configuration of 17 32-fold segmented high-purity germanium detectors for detecting γ rays. 10 detectors were mounted in a ring at 90° relative to the beam axis and in the plane of the target. The remaining 7 detectors were mounted in a ring at 37° relative to the beam axis as shown in Figure 3.7. After passing through the target, the projectile-like reaction residues continued into the S800 focal plane [60] where they were identified and tracked on an event-by-event basis. The S800 was set to accept inelastically scattered reaction residues, but contributions to ^{63}Mn due to knockout from other components of the cocktail beam could not be excluded. This was due to lack of an incoming particle identification and strong contamination from ^{65}Fe that could produce ^{63}Mn within the acceptance of the spectrograph. More detailed descriptions of the beam production and experimental equipment can be found

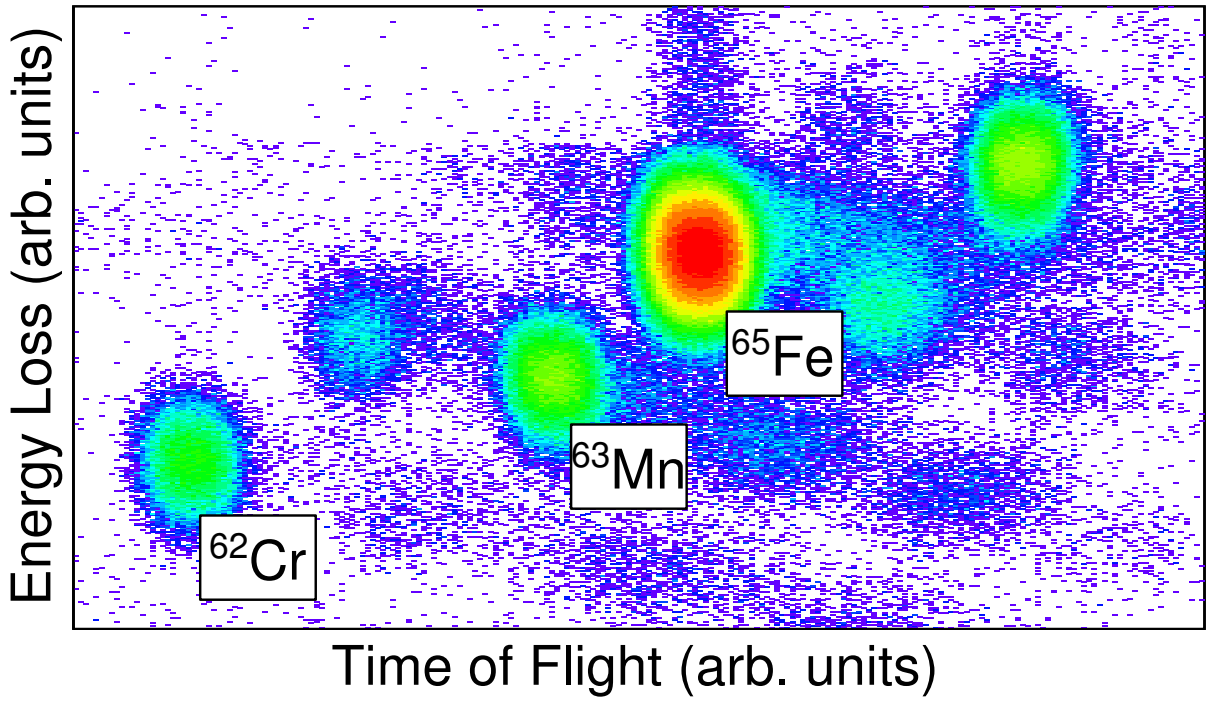

Figure 5.1: Particle identification matrix for the setting used for the γ-ray spectroscopy of ^{63}Mn.

in Chapter .

5.2 Data Analysis

Since the setup of this experiment was the same as the Coulomb-excitation of ^{58,60,62}Cr, the calibration and correction procedures for this experiment was also the same as described in Chapter . The particle-identification matrix for ^{63}Mn is shown in Figure 5.1. The time-of-flight is taken between the object and E1 scintillators and the energy loss is measured with the S800 ionization chamber.

An event-by-event Doppler correction was performed on the γ-ray data. The Doppler-corrected γ-ray spectrum is shown in Figure 5.2. Prominent in the spectrum are two γ-ray transitions, one at 248 keV and another at 635 keV, and a weaker transition at 375(5) keV.

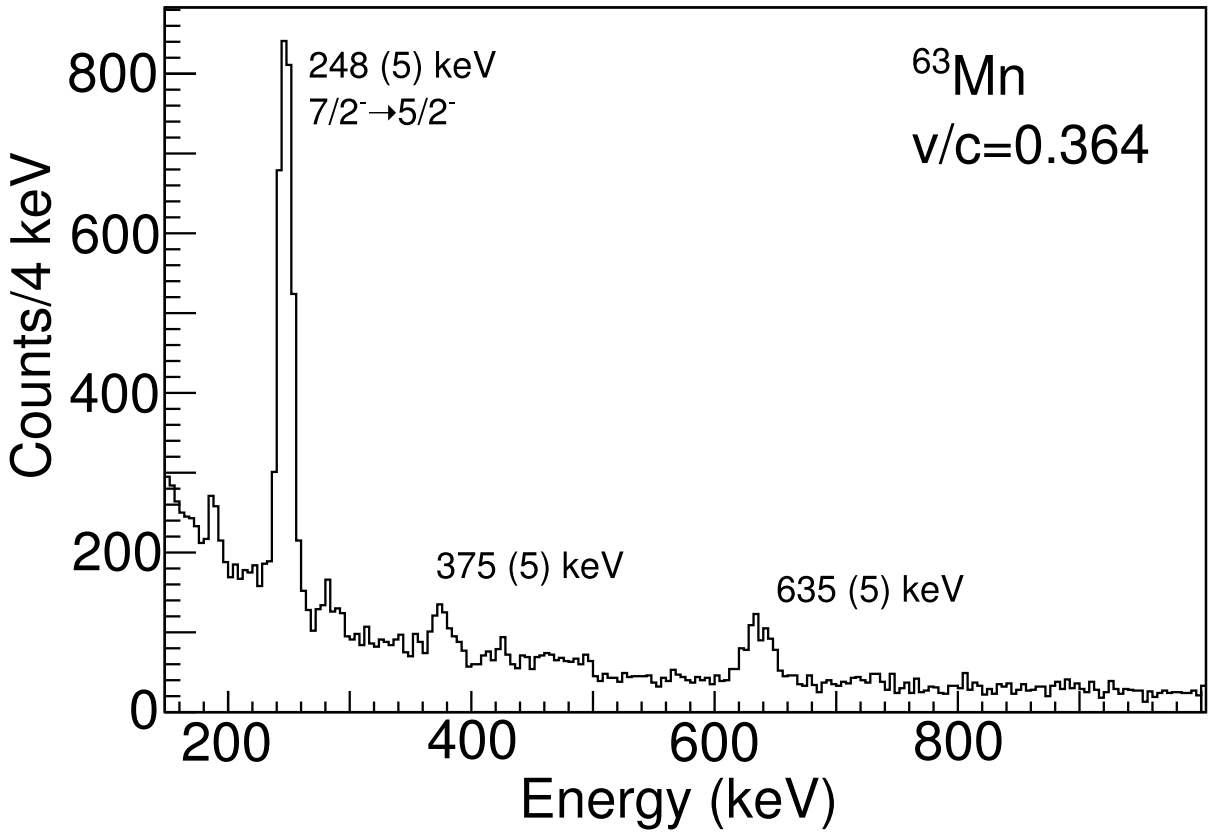

Figure 5.2: Event-by-event Doppler-reconstructed γ-ray spectrum detected by SeGA in coincidence with ^{63}Mn particles.

The 248-keV transition was previously attributed to the $7/2^- \rightarrow 5/2^-_{\text{g.s.}}$ transition [97]. The spin and parity assignments for the $5/2^-$ ground state and $7/2^-$ state are based on the systematics of the lighter Mn isotopes [98, 100, 101] and reinforced by shell-model calculations (see Figure 5.8). The 635- and 375-keV transitions have not been reported in ^{63}Mn before.

γ rays detected within a certain time interval (in this case 600 ns) are said to be in coincidence with one another. Coincident γ rays were stored in a two-dimensional coincidence matrix. Software gates were then placed around peaks in the projection of the coincidence matrix as shown in Figure 5.3. Background gates were placed in a peak-free region of the spectrum on the high-energy side of each peak to avoid the Compton background of the peaks.

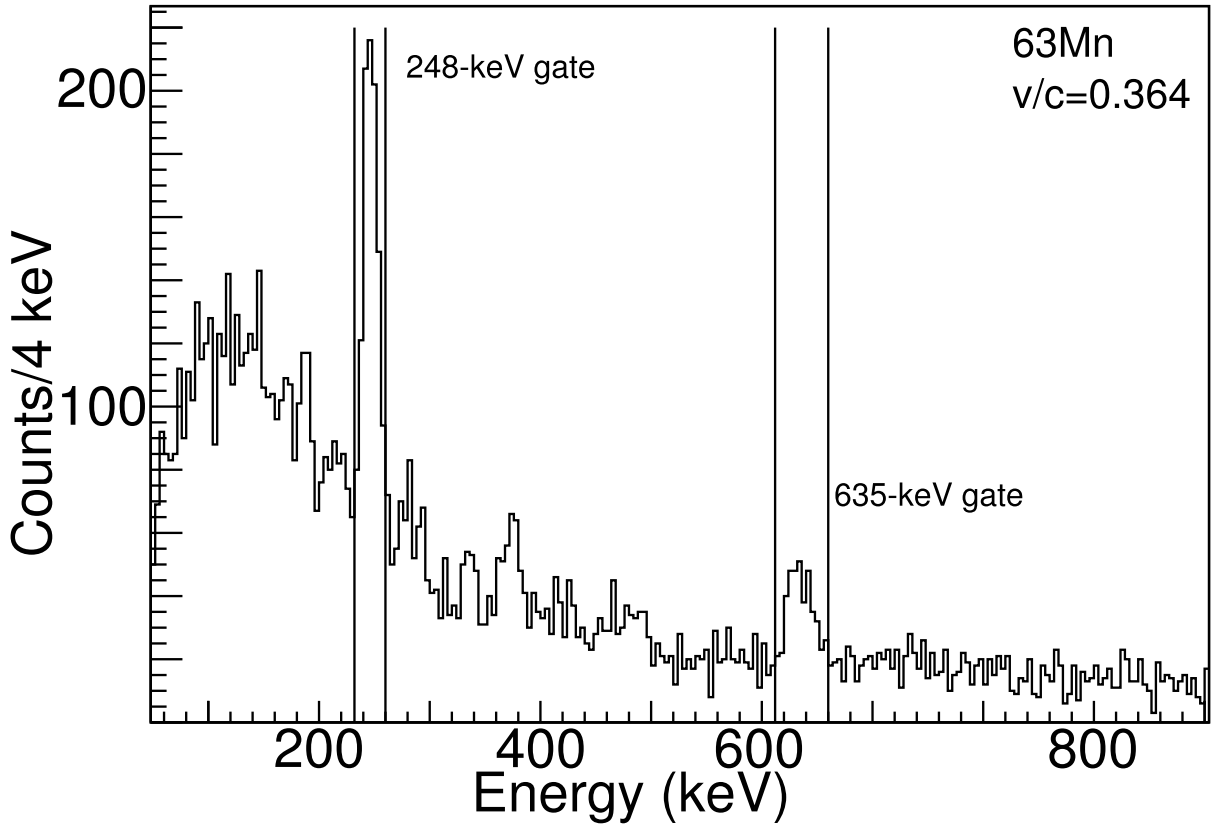

Figure 5.3: Projection of the two-dimensional $\gamma - \gamma$ coincidence matrix used to identify coincidences in the ^{63}Mn spectrum. The software gates are indicated.

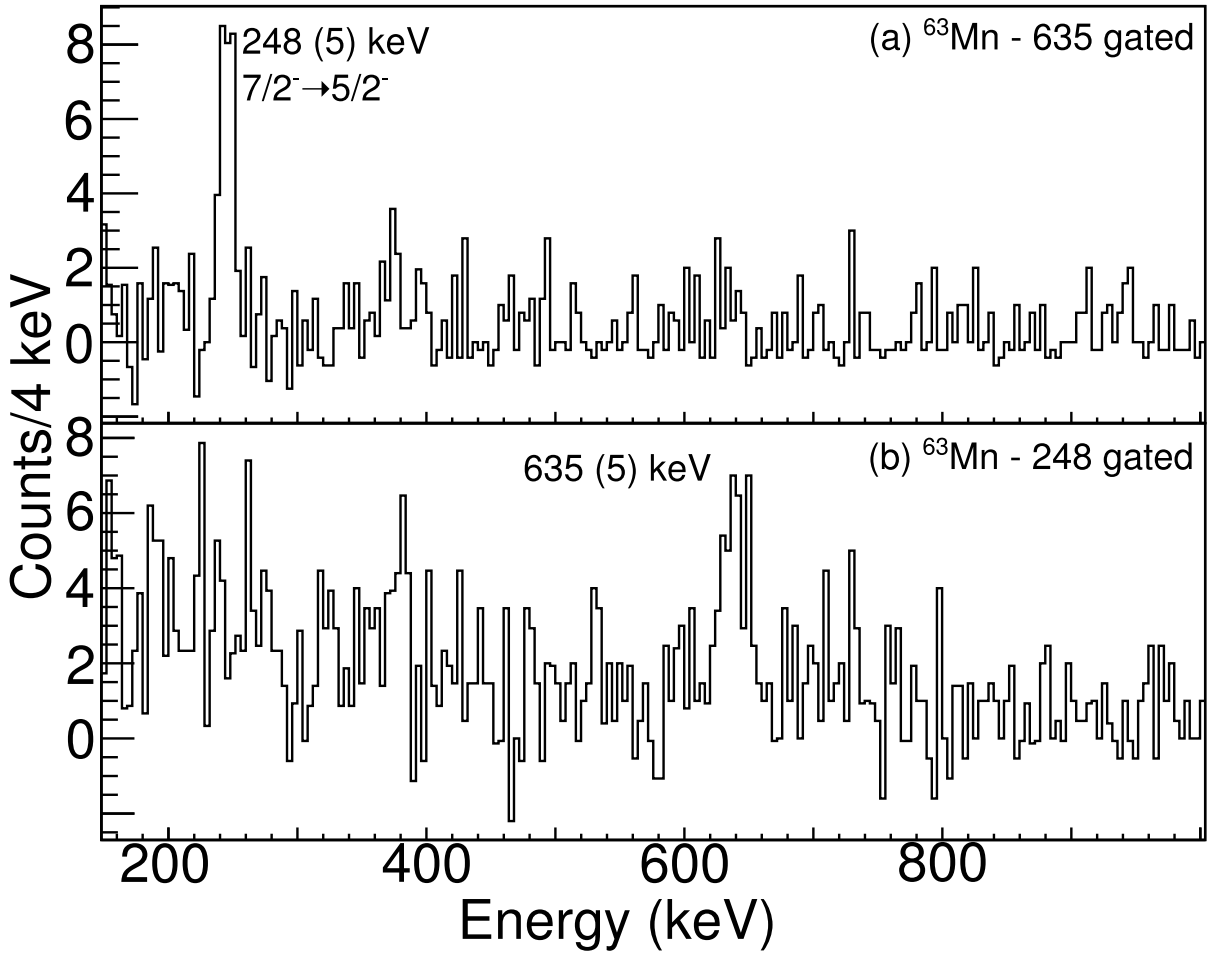

Figure 5.4: $\gamma - \gamma$ coincidence spectra detected in SeGA in coincidence with ^{63}Mn particles in the S800 focal plane. The top panel is gated on the 635-keV transition, and the bottom panel is gated on the 248-keV transition.

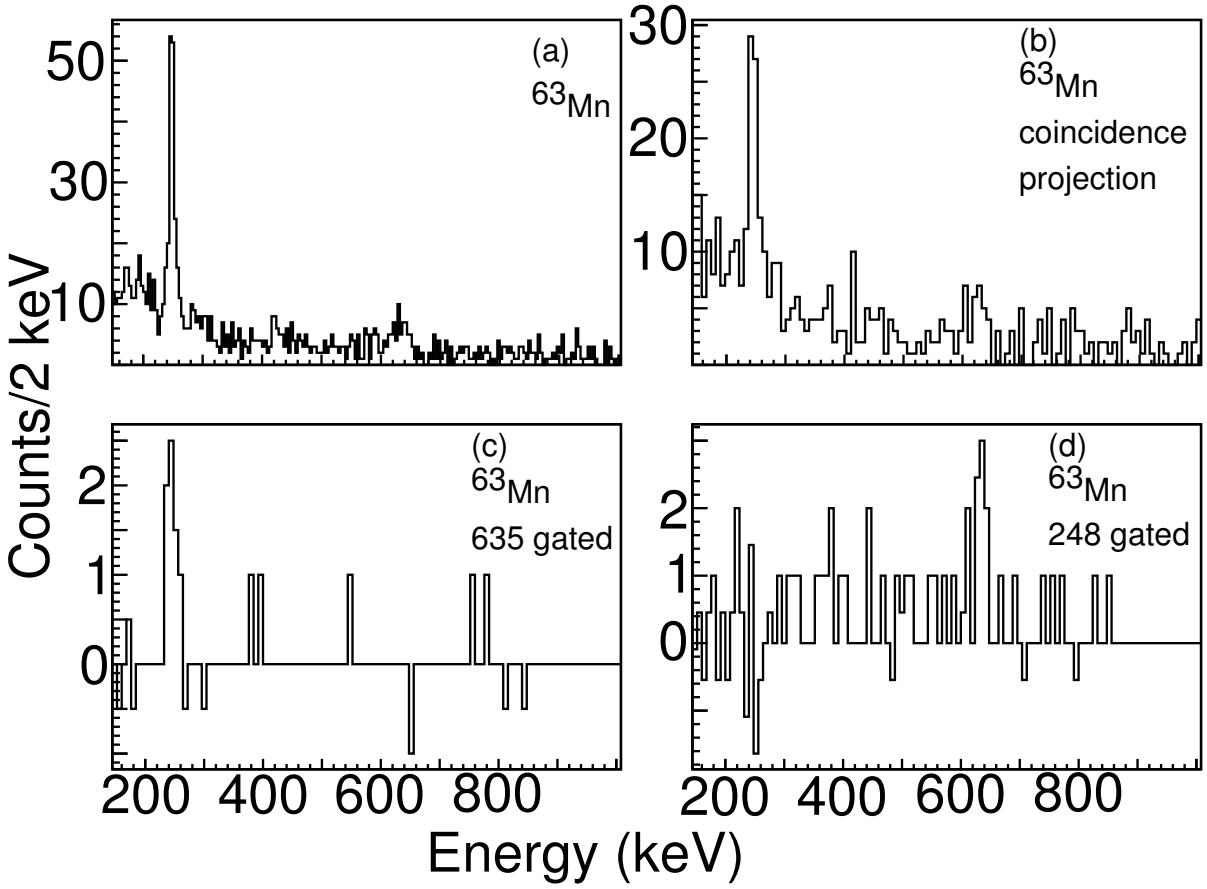

Figure 5.5: γ rays detected in GRETINA in coincidence with ^{63}Mn particles in the S800 focal plane (a), the projection of the coincidence matrix (b), with gate on the 635- and 248-keV transitions (c) and (d), respectively.

The spectra resulting from the $\gamma - \gamma$ coincidence gating are shown in Figure 5.4. In the spectrum resulting from the gate on the 248-keV transition, the 635-keV transition is evident and vice versa. This is evidence that the transitions are in coincidence. Since the 248-keV transition is known to proceed to the ground state, the 635-keV transition is placed on top of the 248-keV level and given a tentative spin-parity assignment of $9/2^-$. The spin-parity assignment is made based on analogy to the level schemes of the lighter Mn isotopes from [97], which are reproduced in Figure 5.8. Also visible in each of the gated spectra is the 375-keV transition, suggesting that this transition feeds the 635-keV transition.

As further confirmation of the coincidence, ^{63}Mn was also produced in a separate ex-

periment via one-neutron knockout from ^{64}Mn. De-excitation γ rays were detected in the GRETINA array [102], and the same two transitions were observed and found to be in coincidence (see Figure 5.5).

5.2.1 Excited-state Lifetime Effects

Figure 5.6 shows the effect of the excited-state lifetimes of the $9/2^-$ and $7/2^-$ states on the γ-ray spectrum. Both the top and bottom panel in Figure 5.6 show event-by-event Doppler-corrected γ-ray spectra measured in coincidence with ^{63}Mn for the 90° and 37° rings of SeGA. In the top panel β=0.340 was used for the event-by-event Doppler reconstruction and in the bottom panel $\beta = 0.364$ was used. Two lifetime effects are apparent: the 248- and 635-keV peaks are aligned for different β values, and the resolution of the 635-keV peak is broad.

The projectile nucleus loses energy continuously as it traverses the target, as described by the Bethe equation (Equation 3.4). If an excited-state lifetime is short enough for the decay to predominantly occur within the target, the γ-ray peak resolution will be dominated by the $\Delta\beta$ term of Equation 3.8. With a thick target, the uncertainty in β is large because the range in β is anything from the β value it had when entering the target to the β value it has upon exiting the target after maximum energy loss. The result is a broader γ-ray line shape like the one seen for the 635-keV transition in Figure 5.6.

In the case where an excited-state lifetime exceeds the time it takes the projectile to traverse the target, the uncertainty in β will be less than the short-lifetime case, as the nucleus decays predominantly behind the target, and will be limited to the incoming energy distribution convoluted with the velocity straggling in the target. This results in a sharper peak as seen at 248 keV in Figure 5.6.

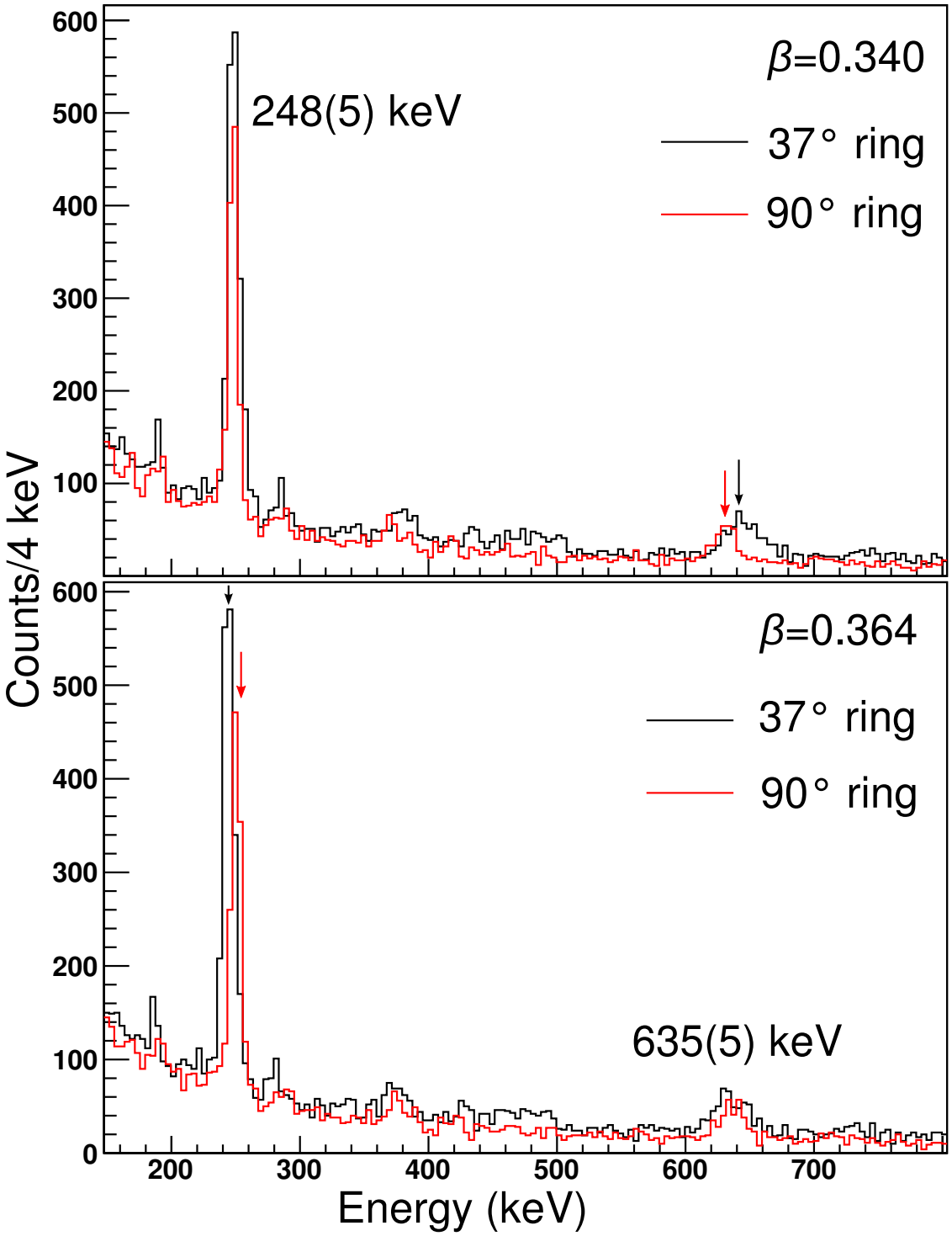

Figure 5.6: ^{63}Mn γ-ray spectra for the two rings of SeGA. In the top panel, β=0.340 was used for the event-by-event Doppler reconstruction of the γ rays emitted in flight with $v/c = 0.340$, while in the bottom panel $\beta = 0.364$ was used. The positions of the peaks in each ring relative to the other is different in each case, illustrating an effect of the excited-state lifetime.

$J_i^\pi \rightarrow J_f^\pi$	E_γ (keV)	τ_{37° (ps)	τ_{90° (ps)	τ (ps)
$7/2^- \rightarrow 5/2^-$	248	$9.7^{+0.7}_{-0.7}$	$10.9^{+1.7}_{-1.4}$	10(2)
$9/2^- \rightarrow 7/2^-$	635	< 3	< 3	< 3

Table 5.1: Results from the simulations of excited-state lifetimes for the two transitions in the ^{63}Mn spectrum.

Another lifetime-related effect is the position of the peaks in the spectrum. The short-lived states will decay on average when the projectile is moving faster, so a larger β value is needed to align the two rings of SeGA, while the longer-lived state will decay after the projectile has lost more energy in the target. This is demonstrated in Figure 5.6. The β value required to align the 635-keV peaks is larger than the β value needed to align the 248-keV peaks.

These effects can be exploited to determine the excited-state lifetimes for the two states in the spectrum. The simulation described in Section 4.2 was used to simulate the peak shapes of the two transitions. The excited-state lifetimes for both states were varied independently and fit to the data in a χ^2-minimization procedure separately for each ring. The χ^2 as a function of simulated lifetime was then fit to determine the lifetime that minimized the χ^2. The best-fit simulations and χ^2 versus lifetime are shown in Figure 5.7, and the results are summarized in Table 5.1.

5.3 Results and Discussion

The observation of a coincidence between the 635-keV and 248-keV transitions leads to the level scheme proposed in Figure 5.8. For comparison, the level schemes proposed for ^{59,61}Mn by Valiente-Dobón *et al.* in [97] are reproduced in Figure 5.8 as well. All spin-parity assignments in Figure 5.8 are tentative and based on systematics of the lighter Mn isotopes,

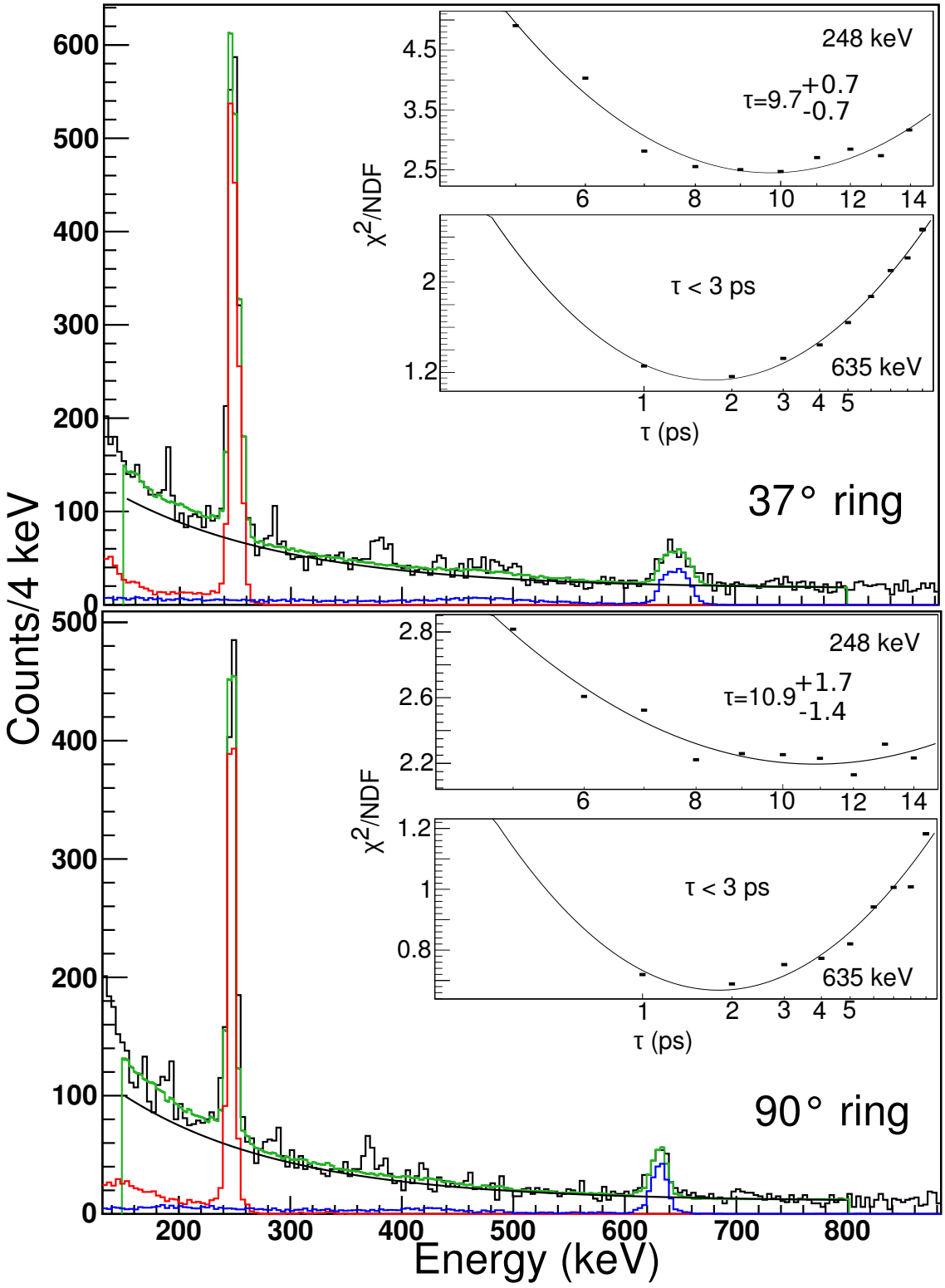

Figure 5.7: Fits of simulated γ-ray transitions to measured γ-ray spectra used to determine the excited state lifetimes of the 248- and 635-keV transitions in ^{63}Mn. Inset are the fits of χ^2 versus simulated lifetime used to find the best-fit lifetime.

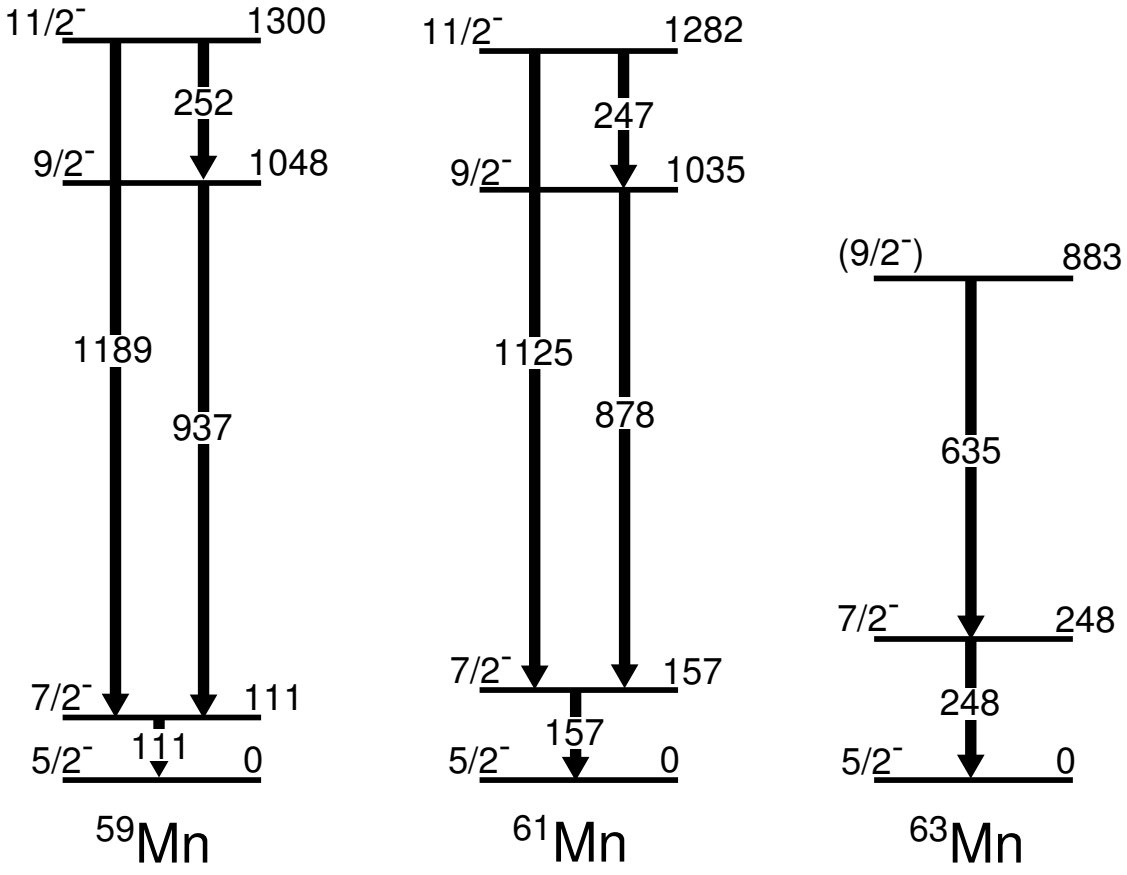

Figure 5.8: Comparison of proposed level schemes for ^{59,61,63}Mn for levels below 1.5 MeV. The level schemes for ^{59,61}Mn are taken from [97]. Spin-parity assignments are tentative, based on systematics and shell-model calculations.

as well as shell-model calculations. The similarities in structure between the isotopes are obvious. In each case there is a $7/2^-$ state at low energy, then a larger gap to a $9/2^-$ state, and in the cases of ^{59,61}Mn an $11/2^-$ state above that. In ^{59}Mn a $15/2^-$ state is suggested at nearly 3 MeV in [97] but is not shown in Figure 5.8.

The 375-keV transition is not placed in the level scheme. Based on the $\gamma - \gamma$ coincidence analysis, the 375-keV transition could be placed on top of the 635-keV transition, and comparison with the lighter odd-even Mn isotopes would tentatively suggest an $11/2^-$ assignment. However, the β value needed to align the 375-keV peak in the rings of SeGA in Doppler reconstruction implies that the lifetime of this state is short - similar to the lifetime of the $9/2^-$ state that decays via the 635-keV transition. Given the low energy of the transition, if the spin of this state were 11/2, one would expect a longer lifetime due to the energy denominator in Equation 1.24. An $E1$ multipolarity could be suggested due to the short lifetime, but this would require the 375-keV transition depopulate a positive parity state, $11/2^+$, $9/2^+$ or $7/2^+$. The shell-model calculations discussed here are of limited use in this case, as they are limited to negative-parity states with $J \leq 9/2$. Given the similarity of the (fast) lifetimes and the fact that the 375-keV transition feeds the 635-keV transition weakly, with an intensity of 37% relative to the 635-keV transition, the feeding has negligible effect on the determination of the lifetime of the $9/2^-$ state.

The proposed level scheme for ^{63}Mn is compared to shell-model calculations in Figure 5.9. The spins given are $2J$ and all states are of negative parity. Only yrast levels up to $9/2^-$ are shown. Several calculations were performed using different interactions and model /spaces: The LNPS effective interaction [40] used the full fp shell for protons and the $1p_{3/2}$, $1p_{1/2}$, $0f_{5/2}$, $0g_{9/2}$, and $1d_{5/2}$ orbitals for neutrons. Hereafter, this model space will be referred to as the $fpgd$ model space. LNPS-fp is LNPS restricted to the full fp shell for both protons

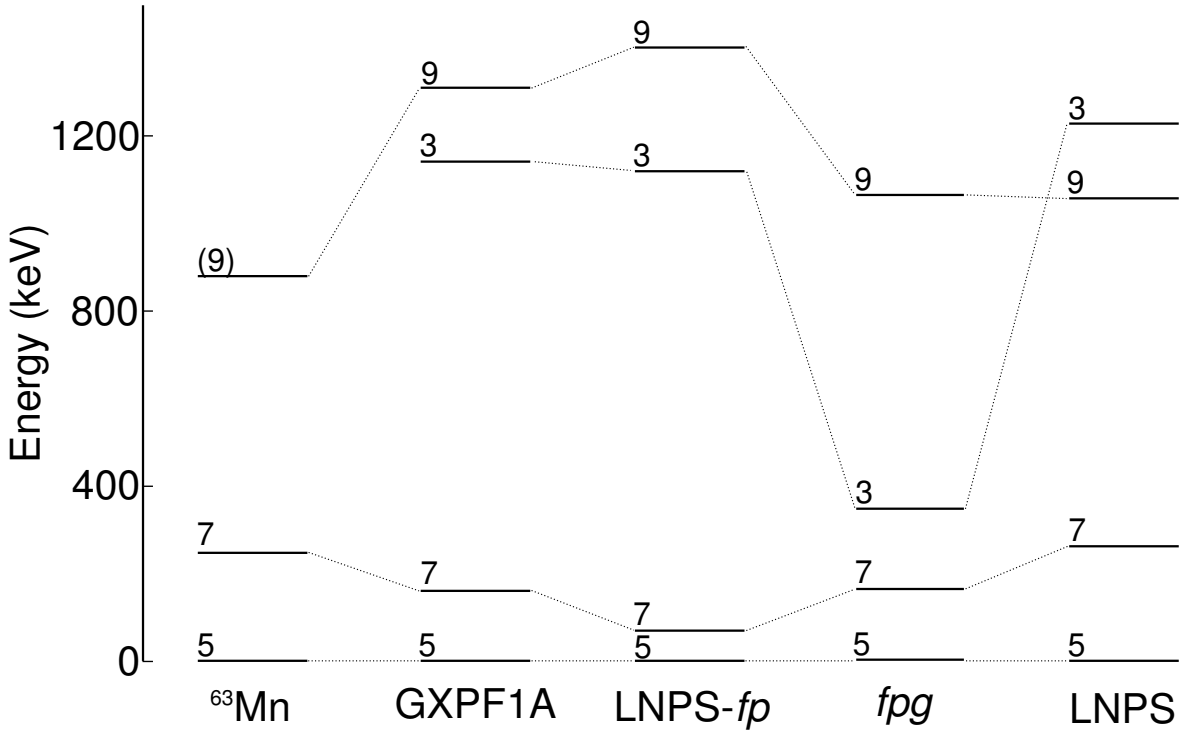

Figure 5.9: Comparison of the proposed level scheme with shell-model calculations, see text for details. Only yrast levels up to $J^\pi = 9/2^-$ are shown. Experimental spin-parity assignments are tentative and based on systematics of the lighter Mn isotopes and the shell-model calculations. Spins are given as $2J$ and all levels shown are of negative parity.

and neutrons. The fpg model space [36] is the $fpgd$ modelspace without the $1d_{5/2}$ neutron orbital active. Calculations using the well-known GXPF1A effective interaction [22, 23] using the fp shell for both protons and neutrons were also included for comparison.

It has been shown that the fp model space is not sufficient to describe neutron-rich fp-shell nuclei in the vicinity of $N = 40$ [74]. In light of this, the LNPS-fp and GXPF1A results reproduce the general low-energy structure of ^{63}Mn surprisingly well, while inclusion of the $0g_{9/2}$ orbital, as is done in the fpg effective interaction, brings the $9/2^-$ level down in energy and closer to the experimental result. Particularly curious is the behavior of the $3/2^-$ level in the calculations. In the calculations using only the fp model space (*i.e.* LNPS-fp and GXPF1A), the $3/2^-$ state sits around 1 MeV. The inclusion of the $1g_{9/2}$ neutron orbital brings the $3/2^-$ state down to 300 keV. The state-of-the-art LNPS interaction, which includes both the $0g_{9/2}$ and $1d_{5/2}$ neutron orbitals, brings the $3/2^-$ state back above 1 MeV. A $3/2^-$ state has not been identified in ^{63}Mn, so no experimental guidance can be given, but in ^{61}Mn, two states with possible $3/2^-$ assignment were seen above 1 MeV [98]. The structure of the $3/2^-$ state is at present being investigated by one of out theory collaborators (S. M. Lenzi).

In order to compare the data to the calculations in more depth, the transition probabilities were investigated. The $7/2^- \rightarrow 5/2^-$ and $9/2^- \rightarrow 7/2^-$ transitions are both mixed $E2/M1$ transitions. Using the experimental energies, shell-model transition probabilities, and Equations 1.20 and 1.24 from Section 1.1, we can calculate the multipole mixing ratios and excited-state lifetimes to compare to the lifetimes determined in Section 5.2.1. The calculated $B(E2)$ values used effective charges of $e_p = 1.31$ and $e_n = 0.46$ of [27], and the $B(M1)$ strengths were calculated using effective g-factors, $g_p^s = 4.189$, $g_n^s = -2.869$, $g_p^\ell = 1.1$, $g_n^\ell = -0.1$.

The calculated lifetimes are compared to the experimentally determined ones in Table

Interaction	$J_i^\pi \rightarrow J_f^\pi$	Exp. Energy (MeV)	$B(E2)_{\rm sm}$ ($e^2{\rm fm}^4$)	$B(M1)_{\rm sm}$ (μ_N^2)	δ	$\tau_{\rm sm}$ (ps)	$\tau_{\rm exp.}$ (ps)
LNPS [40]	$7/2^- \rightarrow 5/2^-$	0.248(5)	467	0.12	0.13	30	10(2)
	$9/2^- \rightarrow 7/2^-$	0.635(5)	321	0.26	0.19	0.8	< 3
fpg [36]	$7/2^- \rightarrow 5/2^-$	0.248(5)	386	0.01	0.34	228	10(2)
	$9/2^- \rightarrow 7/2^-$	0.635(5)	54	0.01	0.37	18	< 3
LNPS-fp	$7/2^- \rightarrow 5/2^-$	0.248(5)	22	0.05	0.04	67	10(2)
	$9/2^- \rightarrow 7/2^-$	0.635(5)	10	0.02	0.13	13	< 3

Table 5.2: Calculated transition probabilities and excited-state lifetimes using LNPS, fpg, and LNPS-fp effective interactions. Experimentally determined lifetimes are listed for comparison.

5.2. The LNPS lifetimes give the best agreement with the experiment. For the $7/2^- \rightarrow 5/2^-$ transition, the LNPS lifetime of 30 ps is not in agreement with the experimental value of 10(2) ps, but is only over-predicted by a factor of 3, rather than the factors of 20 and 7 seen with the fpg and LNPS-fp predictions. For the $7/2^- \rightarrow 5/2^-$ transition, the LNPS prediction of 0.8 ps is consistent with the upper limit of 3 ps determined experimentally. In contrast, the fpg and LNPS-fp lifetimes are at least one order of magnitude longer at 18 and 13 ps and are clearly incompatible with the experimental limit.

γ-ray spectroscopy was performed on ^{63}Mn and new transitions at 635 and 375 keV were observed. The 635-keV transition was placed in the level scheme based on a $\gamma - \gamma$ coincidence analysis. The transition was observed in coincidence with the 248-keV, $7/2^- \rightarrow 5/2^-$ transition to the ground state and was therefore placed on top of the $7/2^-$ state (see Figure 5.8). The 375-keV transition was not placed in the level scheme. There is, however, evidence that this transition is fast and in coincidence with both the 248- and 635-keV transitions. The

tentative spin-parity assignment of $9/2^-$ was made based on analogy to the lighter ^{59,61}Mn isotopes and shell-model calculations. Simulations were used to determine the lifetimes of the $7/2^-$ and $9/2^-$ states. Shell-model calculations were performed in the $fpgd$, fpg, and fp model spaces, and the shell-model transition probabilities and $E2/M1$ mixing ratios were used to calculate theoretical lifetimes for the excited states. Table 5.2 demonstrates the importance of the $\nu 0g_{9/2}$ and $\nu 1d_{5/2}$ orbitals in the model space, as the full $fpgd$ calculation give the best agreement with the experimental lifetimes, as well as good agreement with the excitation energies (Figure 5.9).

Chapter 6

Summary and Conclusion

In the preceding chapters several results were presented. Coulomb excitation measurements aimed at quantifying the collectivity of the neutron-rich chromium isotopes ^{58,60,62}Cr were performed. These measurements resulted in the first determination of the $B(E2; 0_1^+ \rightarrow 2_1^+)$ values for ^{60,62}Cr and quantified the trend of increasing quadrupole collectivity in the region below ^{68}Ni. For ^{62}Cr, a distinct γ-ray lineshape was observed resulting from an excited-state lifetime of several ten to hundreds of picoseconds. The level lifetime was determined based on fits of the simulated response of the γ-ray detection system under the experimental conditions. The $B(E2; 0_1^+ \rightarrow 2_1^+)$ value deduced from the lifetime was found to be in agreement with the $B(E2; 0_1^+ \rightarrow 2_1^+)$ value determined via intermediate-energy Coulomb excitation, lending further confidence to the result. For ^{60,62}Cr, the ratios of neutron to proton transition matrix elements, $|M_n/M_p|$, were determined by combining the $B(E2)$ values from this work with quadrupole deformation lengths determined via inelastic proton scattering [79].

The experimental results were compared to state-of-the-art shell-model calculations using the LNPS effective interaction [40]. The LNPS interaction uses the fp model space for protons and the $fpgd$ model space ($1p_{3/2}$, $0f_{5/2}$, $1p_{1/2}$, $0g_{9/2}$, and $1d_{5/2}$) for neutrons. The importance of the $0g_{9/2}$ and $1d_{5/2}$ neutron orbitals in the model space is emphasized by comparison to calculations in model spaces which do not include these orbitals, such as the fp model space. As the $N = 40$ sub-shell gap is weakened in chromium by the removal of

protons from ^{68}Ni, excitations across the $N = 40$ sub-shell gap become increasingly important to the low-lying nuclear structure [40, 74]. Calculations restricted to the fp model space do not allow any of these excitations, and thus cannot reproduce the experimental data.

Different formulations of the $E2$ effective charge were explored in the calculations of the $B(E2)$ and $|M_n/M_p|$ values. The standard values of $e_n = 0.5$ and $e_p = 1.5$ over-predicted the $B(E2)$ values, while the slightly reduced values of $e_n = 0.4$ and $e_p = 1.4$ produced better agreement. Slight variations on the N- and Z-dependent effective charge formulation of Bohr and Mottleson [24, 95] were also explored. While the particular choice of effective charge had little impact on the theoretical $B(E2)$ values, the theoretical $|M_n/M_p|$ values showed more variation, suggesting the possibility of $|M_n/M_p|$ as a way to discriminate among the different approaches. Independent of the choice of effective charges, the $B(E2)$ values of ^{62,64}Cr were predicted to be equal by LNPS [64]. The $B(E2)$ value of the key $N = 40$ nucleus ^{64}Cr was measured in a later experiment and found to be within 10% of the LNPS prediction [37].

In the γ-ray spectroscopy of ^{63}Mn, two new transitions were observed, along with a known transition. One of the new transitions was able to be placed in the level scheme, feeding the first excited state. The data gathered on ^{63}Mn was compared with shell-model calculations using the LNPS effective interaction in the full $fpgd$ model space as well as in the reduced fpg and fp model spaces. The lifetimes of the observed transitions were determined using a simulation of the γ-ray detector array. The experimental transition energies were combined with the shell model transition probabilities to determine the theoretical lifetimes of the observed transitions. It was shown that the calculations in the full $fpgd$ model space best reproduced the experimental lifetimes, again underscoring the importance of the $0g_{9/2}$ and $1d_{5/2}$ neutron orbitals.

The influence that the $0g_{9/2}$ and $1d_{5/2}$ neutron orbitals have on these isotopes is interesting

because they are separated from the pf shell by a harmonic oscillator shell closure, and therefore are of opposite parity to the pf shell. Excitations across the $N = 40$ gap become energetically favorable when the size of the gap is reduced due to the influence of the monopole component of the proton-neutron tensor force, which simultaneously lowers the $0g_{9/2}$ and $1d_{5/2}$ neutron orbitals while raising the $0f_{5/2}$ neutron orbitals through interactions with the $0f_{7/2}$ proton holes. The $0g_{9/2}$ and $1d_{5/2}$ orbitals are $\Delta j = 2$ partners belonging to a quasi-$SU(3)$ symmetry group, which is known to be deformation-driving [103]. For years, the parallels between the region below ^{68}Ni and the 'island of inversion' observed around ^{31}Na [28] led to predictions that another island of inversion exists around ^{64}Cr [40, 74], and as rare isotope facilities improve, experimental studies are contributing to our knowledge of this region.

Interesting information on the nuclear structure in this region will continue to be provided by experiments probing the single-particle structure of $N \approx 40$ nuclei, an example being a recent experiment conducted at NSCL in which single neutrons were removed from ^{64,66}Fe and ^{68}Ni in order to quantify the occupancy of the $0g_{9/2}$ and $1d_{5/2}$ neutron orbitals in these isotopes [104]. In the future, the limits of the island will be explored as more intense beams of neutron-rich isotopes will be provided by new facilities such as FRIB [105] and ever more sensitive detectors such as GRETINA [102].

APPENDIX

CAESAR Simulations

The CAESium-iodide ARray (CAESAR) was recently commissioned at NSCL [63]. CAESAR consists of 192 CsI(Na) scintillating crystals for γ-ray detection and is being used at NSCL to perform in-beam γ-ray spectroscopy of fast, exotic beams provided by the NSCL's coupled cyclotron facility [47]. CAESAR was designed to provide high γ-ray detection efficiency with moderate energy resolution while utilizing a nearest-neighbor addback routine. Because the geometry of CAESAR lacks symmetry, a simulation is needed to determine the efficiency of CAESAR in response to Lorentz-boosted γ rays emitted from nuclei traveling at $\sim 0.4c$. A simulation was developed and tested against the performance of CAESAR using efficiency and spectral response to radioactive sources as benchmarks before employing the simulation in analysis of in-beam data [106].

Publications using the simulation to date are [37, 107].

User's Guide for CAESAR Simulations

Installation

To use the simulation and sorting code, you will need GEANT4[1] and ROOT[2] installed. The simulation tarball is available from

`https://groups.nscl.msu.edu/gamma/wiki/doku.php?id=computers:computers`

extract it in the directory you want to work and compile using the commands

```
make clean
make
```

GEANT4 provides a configuration script to set the environment variables.

Running the Simulation

```
UCCAESAR run.mac
```

will start `UCCAESAR` and execute the commands in `run.mac`. See examples below.

Sorting

The program `caesarsort` is used to sort the output file into histograms. To compile,

```
make clean
make
```

Do `caesarsort -h` for usage instructions.

Spectrum naming: The naming convention used by `caesarsort` is as follows.

[1] `http://geant4.web.cern.ch/geant4/`
[2] `http://root.cern.ch/drupal/`

- `n0` means that each event in that spectrum did not have any neighboring detectors fire.
- `n1` means that exactly one of the neighboring detectors fired and add-back was done into the detector that registered the higher energy of the two.
- `n0n1` is `n0` and `n1` added together.
- `ng` means that more than two neighboring detectors fired so we don't know what to do (g for garbage).
- `cal` means not doppler corrected
- `dop` means doppler corrected.

Detector numbering: The most upstream ring is called ring A, most downstream is J. Within each ring, detectors are numbered starting from 1 with the upper left corner going clockwise if facing downstream.

Important text files: `caesarsort` reads these files at runtime. They must be in the same directory as the executable.

- `neighbors.txt` has the neighbor relationships between the detectors for addback. Don't edit this unless you really want to.
- `detectorPositions.txt` contains the positions of the detectors in space relative to the center of the array. This is another file you probably don't want to edit. This file is also read by the simulation program to set up the geometry.
- `omitDets.txt` list in here numbers of the detectors you want left out of your sort. You might want to do this if you have a flaky channel or two, for example. Use the command `-x` to activate.

- `threshParams.txt` Model the energy threshold of the CFD for each individual detector. First column is the mean of a gaussian, second column is FWHM
- `widthParams.txt` Parametrizes the energy resolution of each CAESAR detector as aE^b
- `Doppler.txt` Contains the β parameter for the doppler reconstruction.

Example Input Files

The following sections contain example macro files typically used to analyze an experiment. There are separate inputs for simulation of sources, in-beam experiments, target excitations, and ion tracking modes.

Source Simulations

Run source simulations to compare simulated and measured efficiency, determine resolution and threshold parameters.

```
# set up a simulation of a source
/Experiment/RunSource
/Experiment/Source/Set simple
# gamma-ray energy to simulate
/Experiment/Source/setEnergy 662. keV
# target material and thickness: 'G4_Galactic' is vacuum, i.e., no target
/Target/Material G4_Galactic
/Target/Thickness 0.1 mm
```

```
# position of target and source emission point
/Target/SetPosition_Z 2.55 cm
/Experiment/Source/setZ 2.55 cm
# filename to save the output and number of gammas to simulate
/Output/Filename Cs137.out
/run/beamOn 1000000
```

In-beam Simulations

To simulate a γ-ray spectroscopy run, use:

```
# set up a simulation of an in-beam experiment
/Experiment/Reaction/On
# target material
/Target/Material Au
# thickness of target
/Target/Thickness 332.5 um
# size of target
/Target/X_length 5.0 cm
/Target/Y_length 5.0 cm
# position of target relative to the center of caesar
# positive values are downstream of center
/Target/SetPosition_Z 2.55 cm
# define the beam, this example is 74Ni
/BeamIn/A 74
```

```
/BeamIn/Z 28

# energy (per nucleon) of the incoming beam

/BeamIn/KEu 94.5 MeV

# fractional momentum spread of the incoming beam

/BeamIn/Dpp 0.005

# nucleons removed in the reaction, this is inelastic scattering

/BeamOut/DA 0

/BeamOut/DZ 0

#  excited state energy to simulate

/BeamOut/ProjectileExcitation 1024. keV

#excited state lifetime

/BeamOut/tau 0 ps

# angular distribution coefficients for Coulomb excitation

/BeamOut/seta0 1.0

/BeamOut/seta2 0.0

/BeamOut/seta4 0.0

# outgoing beam angular distribution in the dispersive and non-dispersive

/BeamOut/AngDistSigmaA 0.012 rad

/BeamOut/AngDistSigmaB 0.012 rad

# print information about the simulation parameters

/BeamIn/Report

/BeamOut/Report

/Target/Report

/ExpHall/Report
```

```
/CAESAR_Array/Report

# file to save the output

/Output/Filename 74Ni.out

# number of events to simulate

/run/beamOn 1000000
```

Ion Tracking

Ion tracking mode is useful for checking the beam parameters, such as kinetic energy, transverse and parallel momentum distributions, velocity, position and angles at several points during the simulation. To set up the simulations are correct you have to do the following stpdf:

- Make one simulation with the command `/IonPrint/Track_Set` active in the `.mac` file (usually commented out) and 2000 particles.
- When you start the simulation make sure to have the output written into a `.log` file like this: `UCCAESAR test.mac > test.log`
- Do a second simulation with the print command commented out: `#/IonPrint/Track_Set` and use at least 100000 particles
- Sort the last simulation with `caesarsort` to create a root file
- Start root and Load `ions2.C` with `.L ions2.C`.
- Type in the command `Do("test.log","real_sim.root",A)`. The first input is the `.log` file you created with only 2000 particles, the second input is the sorted root file you created with at least 100000 particles And the third input is the mass number A of the simulated beam.

This creates a ROOT file out of the `.log` file and also plots some overview spectra to check the simulations. You only have to run this once, if the `.log.root` file already exits and you just want to plot the overview spectra then you can use `Plot("test.log","real_sim.root")`.

Target Excitations

To simulate excitations of the target, ^{197}Au, for example, use:

```
# set up a simulation of an in-beam experiment
/Experiment/Reaction/On
# target material
/Target/Material Au
# thickness of target
/Target/Thickness 332.5 um
# size of target
/Target/X_length 5.0 cm
/Target/Y_length 5.0 cm
# position of target relative to the center of caesar
# positive values are downstream of center
/Target/SetPosition_Z 2.55 cm
# Produce only target excitations
/BeamOut/TargetExcitationFraction 1
#  excited state energy to simulate
/BeamOut/TargetExcitation 547.5 keV
# angular distribution coefficients for Coulomb excitation
```

```
# of the target

/BeamOut/setTargeta0 1.0

/BeamOut/setTargeta2 0.0

/BeamOut/setTargeta4 0.0

# print information about the simulation parameters

/BeamIn/Report

/BeamOut/Report

/Target/Report

/ExpHall/Report

/CAESAR_Array/Report

# file to save the output

/Output/Filename target_excitation.out

# number of events to simulate

/run/beamOn 1000000
```

BIBLIOGRAPHY

BIBLIOGRAPHY

[1] Richard F. Casten. *Nuclear Structure from a Simple Perspective*. Oxford University Press, 1990.

[2] Peter J. Mohr, Barry N. Taylor, and David B. Newell. CODATA recommended values of the fundamental physical constants: 2010. *Rev. Mod. Phys.*, 84:1527–1605, Nov 2012.

[3] J. Beringer *et al.* Particle Data Group. *Physical Review D*, 84:010001, 2012.

[4] B. Alex Brown. Lecture Notes in Nuclear Structure Physics, 2010.

[5] Maria Goeppert Mayer. On closed shells in nuclei. ii. *Phys. Rev.*, 75:1969–1970, Jun 1949.

[6] Otto Haxel, J. Hans D. Jensen, and Hans E. Suess. On the "magic numbers" in nuclear structure. *Phys. Rev.*, 75:1766–1766, Jun 1949.

[7] B. H. Brown, B. A. and Wildenthal. Status of the nuclear shell model. *Annual Review of Nuclear and Particle Science*, 38(1):29–66, 1988.

[8] Petr Navrátil, Michael Thoresen, and Bruce R. Barrett. Microscopic origins of effective charges in the shell model. *Phys. Rev. C*, 55:R573–R576, Feb 1997.

[9] I. Uluer, C. A. Kalfas, W. D. Hamilton, R. A. Fox, D. D. Warner, M. Finger, and Do Kim Chung. Multipole mixing ratios of transitions in 156 Gd. *Journal of Physics G: Nuclear Physics*, 1(4):476, 1975.

[10] Norman Austern. *Direct Nuclear Reaction Theories*. Wiley-Interscience, 1970.

[11] Ian J. Thompson and Filomena M. Nunes. *Nuclear Reactions for Astrophysics: Principles, Calculation and Applications of Low-Energy Reactions*. Cambridge University Press, 2009.

[12] Aage Winther and Kurt Alder. Relativistic Coulomb excitation. *Nuclear Physics A*, 319(3):518 – 532, 1979.

[13] Alexandra Gade and Thomas Glasmacher. In-beam nuclear spectroscopy of bound states with fast exotic ion beams. *Progress in Particle and Nuclear Physics*, 60(1):161–224, 2008.

[14] J. M. Cook, T. Glasmacher, and A. Gade. Accuracy of $B(E2; 0_1^+ \rightarrow 2_1^+)$ transition rates from intermediate-energy Coulomb excitation experiments. *Phys. Rev. C*, 73:024315, Feb 2006.

[15] T. Glasmacher. Coulomb excitation at intermediate energies. *Annual Review of Nuclear and Particle Science*, 48(1):1–31, 1998.

[16] A. M. Bernstein, V. R. Brown, and V. A. Madsen. Neutron and proton transition matrix elements and inelastic hadron scattering. *Physics Letters B*, 103(4-5):255 – 258, 1981.

[17] A. M. Bernstein, V. R. Brown, and V. A. Madsen. Neutron and proton matrix elements for low-lying 2^+ transitions and the probe dependence of the nuclear deformation parameter. *Comments Nucl. Part. Phys.*, 11:203, 1983.

[18] F. D. Becchetti and G. W. Greenlees. Nucleon-Nucleus Optical-Model Parameters, $A > 40$, $E < 50$ MeV. *Phys. Rev.*, 182:1190–1209, Jun 1969.

[19] A.J. Koning and J.P. Delaroche. Local and global nucleon optical models from 1 keV to 200 MeV. *Nuclear Physics A*, 713(3-4):231 – 310, 2003.

[20] S. Cohen and D. Kurath. Effective interactions for the 1p shell. *Nuclear Physics*, 73(1):1 – 24, 1965.

[21] B. Alex Brown and W. A. Richter. New "USD" Hamiltonians for the *sd* shell. *Phys. Rev. C*, 74:034315, Sep 2006.

[22] M. Honma, T. Otsuka, B. A. Brown, and T. Mizusaki. Effective interaction for pf-shell nuclei. *Phys. Rev. C*, 65:061301(R), May 2002.

[23] M. Honma, T. Otsuka, B.A. Brown, and T. Mizusaki. Shell-model description of neutron-rich pf-shell nuclei with a new effective interaction gxpf 1. *The European Physical Journal A - Hadrons and Nuclei*, 25:499–502, 2005.

[24] Aage Bohr and Ben R. Mottelson. *Nuclear Structure: Nuclear Deformations*, volume two. World Scientific, 1998.

[25] H. Sagawa and B.A. Brown. E2 core polarization for *sd*-shell single-particle states calculated with a Skyrme-type interaction. *Nuclear Physics A*, 430(1):84 – 98, 1984.

[26] R. du Rietz, J. Ekman, D. Rudolph, C. Fahlander, A. Dewald, O. Möller, B. Saha, M. Axiotis, M. A. Bentley, C. Chandler, G. de Angelis, F. Della Vedova, A. Gadea, G. Hammond, S. M. Lenzi, N. Mărginean, D. R. Napoli, M. Nespolo, C. Rusu, and D. Tonev. Effective charges in the fp shell. *Phys. Rev. Lett.*, 93:222501, Nov 2004.

[27] Marianne Dufour and Andrés P. Zuker. Realistic collective nuclear Hamiltonian. *Phys. Rev. C*, 54:1641–1660, Oct 1996.

[28] E. K. Warburton, J. A. Becker, and B. A. Brown. Mass systematics for A=29-44 nuclei: The deformed $A\sim$32 region. *Phys. Rev. C*, 41:1147–1166, 1990.

[29] A. Gade, P. Adrich, D. Bazin, M. D. Bowen, B. A. Brown, C. M. Campbell, J. M. Cook, S. Ettenauer, T. Glasmacher, K. W. Kemper, S. McDaniel, A. Obertelli, T. Otsuka, A. Ratkiewicz, K. Siwek, J. R. Terry, J. A. Tostevin, Y. Utsuno, and D. Weisshaar. Spectroscopy of ^{36}Mg: Interplay of normal and intruder configurations at the neutron-rich boundary of the "island of inversion". *Phys. Rev. Lett.*, 99:072502, 2007.

[30] A. Gade, R. V. F. Janssens, D. Bazin, R. Broda, B. A. Brown, C. M. Campbell, M. P. Carpenter, J. M. Cook, A. N. Deacon, D.-C. Dinca, B. Fornal, S. J. Freeman, T. Glasmacher, P. G. Hansen, B. P. Kay, P. F. Mantica, W. F. Mueller, J. R. Terry, J. A. Tostevin, and S. Zhu. Cross-shell excitation in two-proton knockout: Structure of ^{52}Ca. *Phys. Rev. C*, 74:021302(R), Aug 2006.

[31] A. Huck, G. Klotz, A. Knipper, C. Miehé, C. Richard-Serre, G. Walter, A. Poves, H. L. Ravn, and G. Marguier. Beta decay of the new isotopes ^{52}K, ^{52}Ca, and ^{52}Sc; a test of the shell model far from stability. *Phys. Rev. C*, 31:2226–2237, Jun 1985.

[32] R. V. F Janssens, B. Fornal, P. F. Mantica, B. A Brown, R. Broda, P. Bhattacharyya, M. P. Carpenter, M. Cinausero, P. J. Daly, A. D. Davies, T. Glasmacher, Z. W. Grabowski, D. E. Groh, M. Honma, F. G. Kondev, W. Królas, T. Lauritsen, S. N. Liddick, S. Lunardi, N. Marginean, T. Mizusaki, D. J. Morrissey, A. C. Morton, W. F. Mueller, T. Otsuka, T. Pawlat, D. Seweryniak, H. Schatz, A. Stolz, S. L. Tabor, C. A. Ur, G. Viesti, I. Wiedenhöver, and J. Wrzesiński. Structure of ^{52,54}Ti and shell closures in neutron-rich nuclei above ^{48}Ca. *Physics Letters B*, 546(1-2):55 – 62, 2002.

[33] J. I. Prisciandaro, P. F. Mantica, B. A. Brown, D. W. Anthony, M. W. Cooper, A. Garcia, D. E. Groh, A. Komives, W. Kumarasiri, P. A. Lofy, A. M. Oros-Peusquens, S. L. Tabor, and M. Wiedeking. New evidence for a subshell gap at N=32. *Physics Letters B*, 510(1-4):17 – 23, 2001.

[34] D.-C. Dinca, R. V. F. Janssens, A. Gade, D. Bazin, R. Broda, B. A. Brown, C. M. Campbell, M. P. Carpenter, P. Chowdhury, J. M. Cook, A. N. Deacon, B. Fornal, S. J. Freeman, T. Glasmacher, M. Honma, F. G. Kondev, J.-L. Lecouey, S. N. Liddick, P. F. Mantica, W. F. Mueller, H. Olliver, T. Otsuka, J. R. Terry, B. A. Tomlin, and K. Yoneda. Reduced transition probabilities to the first 2^+ state in ^{52,54,56}Ti and development of shell closures at $N = 32, 34$. *Phys. Rev. C*, 71:041302(R), Apr 2005.

[35] C. J. Lister, M. Campbell, A. A. Chishti, W. Gelletly, L. Goettig, R. Moscrop, B. J. Varley, A. N. James, T. Morrison, H. G. Price, J. Simpson, K. Connel, and O. Skeppstedt. Gamma radiation from the N=Z nucleus $^{80}_{40}$Zr$_{40}$. *Phys. Rev. Lett.*, 59:1270–1273, Sep 1987.

[36] O. Sorlin, S. Leenhardt, C. Donzaud, J. Duprat, F. Azaiez, F. Nowacki, H. Grawe, Zs. Dombrádi, F. Amorini, A. Astier, D. Baiborodin, M. Belleguic, C. Borcea, C. Bourgeois, D. M. Cullen, Z. Dlouhy, E. Dragulescu, M. Górska, S. Grévy, D. Guillemaud-Mueller, G. Hagemann, B. Herskind, J. Kiener, R. Lemmon, M. Lewitowicz, S. M. Lukyanov, P. Mayet, F. de Oliveira Santos, D. Pantalica, Yu.-E. Penionzhkevich, F. Pougheon, A. Poves, N. Redon, M. G. Saint-Laurent, J. A. Scarpaci, G. Sletten, M. Stanoiu, O. Tarasov, and Ch. Theisen. $^{68}_{28}$Ni$_{40}$: Magicity versus Superfluidity. *Phys. Rev. Lett.*, 88:092501, Feb 2002.

[37] H. L. Crawford, R. M. Clark, P. Fallon, A. O. Macchiavelli, T. Baugher, D. Bazin, C. W. Beausang, J. S. Berryman, D. L. Bleuel, C. M. Campbell, M. Cromaz, G. de Angelis, A. Gade, R. O. Hughes, I. Y. Lee, S. M. Lenzi, F. Nowacki, S. Paschalis, M. Petri, A. Poves, A. Ratkiewicz, T. J. Ross, E. Sahin, D. Weisshaar, K. Wimmer, and R. Winkler. Quadrupole Collectivity in Neutron-Rich Fe and Cr Isotopes. *Phys. Rev. Lett.*, 110:242701, Jun 2013.

[38] Takaharu Otsuka, Toshio Suzuki, Rintaro Fujimoto, Hubert Grawe, and Yoshinori Akaishi. Evolution of nuclear shells due to the tensor force. *Phys. Rev. Lett.*, 95:232502, Nov 2005.

[39] Takaharu Otsuka, Rintaro Fujimoto, Yutaka Utsuno, B. Alex Brown, Michio Honma, and Takahiro Mizusaki. Magic numbers in exotic nuclei and spin-isospin properties of the *NN* interaction. *Phys. Rev. Lett.*, 87:082502, Aug 2001.

[40] S. M. Lenzi, F. Nowacki, A. Poves, and K. Sieja. Island of inversion around ^{64}Cr. *Phys. Rev. C*, 82:054301, Nov 2010.

[41] Heiko Scheit. *Low-Lying Collective Excitations in Neutron-Rich Even-Even Sulfur and Argon Isotopes Studied via Intermediate-Energy Coulomb Excitation and Proton Scattering.* PhD thesis, Michigan State University, 1998.

[42] W. W. Wilcke, J. R. Birkelund, H. J. Wollersheim, A. D. Hoover, J. R. Huizenga, W. U. Schröder, and L. E. Tubbs. Reaction parameters for heavy-ion collisions. *Atomic Data and Nuclear Data Tables*, 25(5-6):389 – 619, 1980.

[43] A. N. F. Aleixo and C. A. Bertulani. Coulomb excitation in intermediate-energy collisions. *Nuclear Physics A*, 505(2):448 – 470, 1989.

[44] Heather Zwahlen. *Angular distributions of gamma rays with intermediate-energy beams and spectroscopy of* ^{32}*Mg*. PhD thesis, Michigan State University, 2005.

[45] Heather Olliver, Thomas Glasmacher, and Andrew E. Stuchbery. Angular distributions of γ rays with intermediate-energy beams. *Phys. Rev. C*, 68:044312, Oct 2003.

[46] K. Alder, A. Bohr, T. Huus, B. Mottelson, and A. Winther. Study of nuclear structure by electromagnetic excitation with accelerated ions. *Rev. Mod. Phys.*, 28:432–542, Oct 1956.

[47] D. J. Morrissey. The coupled cyclotron project at the NSCL. *Nuclear Physics A*, 616(1-2):45 – 55, 1997. Radioactive Nuclear Beams.

[48] D. J. Morrissey, B. M. Sherrill, M. Steiner, A. Stolz, and I. Wiedenhoever. Commissioning the A1900 projectile fragment separator. *Nuclear Instruments and Methods in Physics Research Section B: Beam Interactions with Materials and Atoms*, 204(0):90 – 96, 2003. 14th International Conference on Electromagnetic Isotope Separators and Techniques Related to their Applications.

[49] S. Gammino, G. Ciavola, T. Antaya, and K. Harrison. Volume scaling and magnetic field scaling on SC-ECRIS at MSU-NSCL. *Review of Scientific Instruments*, 67(1):155–160, 1996.

[50] G. Machicoane, D. Cole, J. Ottarson, J. Stetson, and P. Zavodszky. ARTEMIS-B: A room-temperature test electron cyclotron resonance ion source for the National Superconducting Cyclotron Laboratory at Michigan State University. *Review of Scientific Instruments*, 77(3):03A322, 2006.

[51] P. A. Zavodszky, B. Arend, D. Cole, J. DeKamp, G. Machicoane, F. Marti, P. Miller, J. Moskalik, J. Ottarson, J. Vincent, and A. Zeller. Design of SuSI — Superconducting Source for Ions at NSCL/MSU — I. The Magnet System. *AIP Conference Proceedings*, 749(1):131–134, 2005.

[52] P. A. Zavodszky, B. Arend, D. Cole, J. DeKamp, G. Machicoane, F. Marti, P. Miller, J. Moskalik, J. Ottarson, J. Vincent, and A. Zeller. Design of SuSI - superconducting

source for ions at NSCL/MSU - II. The conventional parts. *Nuclear Instruments and Methods in Physics Research Section B: Beam Interactions with Materials and Atoms*, 241(1-4):959 – 964, 2005. The Application of Accelerators in Research and Industry Proceedings of the Eighteenth International Conference on the Application of Accelerators in Research and Industry (CAARI 2004) Eighteenth International Conference on the Application of Accelerators in Research and Industry.

[53] R. Pfaff, D. J. Morrissey, W. Benenson, M. Fauerbach, M. Hellström, C. F. Powell, B. M. Sherrill, M. Steiner, and J. A. Winger. Fragmentation of ^{78}Kr projectiles. *Phys. Rev. C*, 53:1753–1758, Apr 1996.

[54] T. Ginter. *A1900 Fragment Separator and High-Energy Beamline Service Level Description*, 2007. NSCL internal document, `nscl.msu.edu/files/A1900_sld_2007.pdf`.

[55] J. P. Dufour, R. Del Moral, H. Emmermann, F. Hubert, D. Jean, C. Poinot, M. S. Pravikoff, A. Fleury, H. Delagrange, and K.-H. Schmidt. Projectile fragments isotopic separation: Application to the LISE spectrometer at GANIL. *Nuclear Instruments and Methods in Physics Research Section A: Accelerators, Spectrometers, Detectors and Associated Equipment*, 248(2-3):267 – 281, 1986.

[56] Glenn F. Knoll. *Radiation Detection and Measurement*. John Wiley & Sons, third edition, 2000.

[57] D. Bazin, J. A. Caggiano, B. M. Sherrill, J. Yurkon, and A. Zeller. The S800 spectrograph. *Nuclear Instruments and Methods in Physics Research Section B: Beam Interactions with Materials and Atoms*, 204(0):629 – 633, 2003. 14th International Conference on Electromagnetic Isotope Separators and Techniques Related to their Applications.

[58] D. Bazin. *S800 Spectrograph Service Level Description*, 2012. NSCL internal document, `nscl.msu.edu/files/s800_sld.pdf`.

[59] Joseph Arthur Caggiano. *Spectroscopy of Exotic Nuclei with the S800 Spectrograph*. PhD thesis, Michigan State University, 1999.

[60] J. Yurkon, D. Bazin, W. Benenson, D. J. Morrissey, B. M. Sherrill, D. Swan, and R. Swanson. Focal plane detector for the S800 high-resolution spectrometer. *Nuclear Instruments and Methods in Physics Research Section A: Accelerators, Spectrometers, Detectors and Associated Equipment*, 422(1-3):291 – 295, 1999.

[61] M. Berz, K. Joh, J. A. Nolen, B. M. Sherrill, and A. F. Zeller. Reconstructive correction of aberrations in nuclear particle spectrographs. *Phys. Rev. C*, 47:537–544, Feb 1993.

[62] W. F. Mueller, J. A. Church, T. Glasmacher, D. Gutknecht, G. Hackman, P. G. Hansen, Z. Hu, K. L. Miller, and P. Quirin. Thirty-two-fold segmented germanium detectors to identify γ-rays from intermediate-energy exotic beams. *Nuclear Instruments and Methods in Physics Research Section A: Accelerators, Spectrometers, Detectors and Associated Equipment*, 466(3):492 – 498, 2001.

[63] D. Weisshaar, A. Gade, T. Glasmacher, G. F. Grinyer, D. Bazin, P. Adrich, T. Baugher, J. M. Cook, C. Aa. Diget, S. McDaniel, A. Ratkiewicz, K. P. Siwek, and K. A. Walsh. CAESAR: A high-efficiency CsI(Na) scintillator array for in-beam spectroscopy with fast rare-isotope beams. *Nuclear Instruments and Methods in Physics Research Section A: Accelerators, Spectrometers, Detectors and Associated Equipment*, 624(3):615 – 623, 2010.

[64] T. Baugher, A. Gade, R. V. F. Janssens, S. M. Lenzi, D. Bazin, B. A. Brown, M. P. Carpenter, A. N. Deacon, S. J. Freeman, T. Glasmacher, G. F. Grinyer, F. G. Kondev, S. McDaniel, A. Poves, A. Ratkiewicz, E. A. McCutchan, D. K. Sharp, I. Stefanescu, K. A. Walsh, D. Weisshaar, and S. Zhu. Intermediate-energy Coulomb excitation of ^{58,60,62}Cr: The onset of collectivity toward $N = 40$. *Phys. Rev. C*, 86:011305(R), Jul 2012.

[65] O. Sorlin and M.-G. Porquet. Nuclear magic numbers: New features far from stability. *Progress in Particle and Nuclear Physics*, 61(2):602 – 673, 2008.

[66] Takaharu Otsuka, Toshio Suzuki, Michio Honma, Yutaka Utsuno, Naofumi Tsunoda, Koshiroh Tsukiyama, and Morten Hjorth-Jensen. Novel features of nuclear forces and shell evolution in exotic nuclei. *Phys. Rev. Lett.*, 104:012501, Jan 2010.

[67] D. Pauwels, O. Ivanov, N. Bree, J. Büscher, T. E. Cocolios, J. Gentens, M. Huyse, A. Korgul, Yu. Kudryavtsev, R. Raabe, M. Sawicka, I. Stefanescu, J. Van de Walle, P. Van den Bergh, P. Van Duppen, and W. B. Walters. Shape isomerism at $N = 40$: Discovery of a proton intruder state in ^{67}Co. *Phys. Rev. C*, 78:041307(R), Oct 2008.

[68] M. Hannawald, T. Kautzsch, A. Wöhr, W. B. Walters, K.-L. Kratz, V. N. Fedoseyev, V. I. Mishin, W. Böhmer, B. Pfeiffer, V. Sebastian, Y. Jading, U. Köster, J. Lettry, H. L. Ravn, and the ISOLDE Collaboration. Decay of Neutron-Rich Mn Nuclides and Deformation of Heavy Fe Isotopes. *Phys. Rev. Lett.*, 82:1391–1394, Feb 1999.

[69] A. Gade, R. V. F. Janssens, T. Baugher, D. Bazin, B. A. Brown, M. P. Carpenter, C. J. Chiara, A. N. Deacon, S. J. Freeman, G. F. Grinyer, C. R. Hoffman, B. P. Kay, F. G. Kondev, T. Lauritsen, S. McDaniel, K. Meierbachtol, A. Ratkiewicz, S. R. Stroberg, K. A. Walsh, D. Weisshaar, R. Winkler, and S. Zhu. Collectivity at $N = 40$ in neutron-rich ^{64}Cr. *Phys. Rev. C*, 81:051304(R), May 2010.

[70] M. Bernas, Ph. Dessagne, M. Langevin, J. Payet, F. Pougheon, and P. Roussel. Magic features of ^{68}Ni. *Physics Letters B*, 113(4):279 – 282, 1982.

[71] C. Guénaut, G. Audi, D. Beck, K. Blaum, G. Bollen, P. Delahaye, F. Herfurth, A. Kellerbauer, H.-J. Kluge, J. Libert, D. Lunney, S. Schwarz, L. Schweikhard, and C. Yazidjian. High-precision mass measurements of Nickel, Copper, and Gallium isotopes and the purported shell closure at $N = 40$. *Phys. Rev. C*, 75:044303, Apr 2007.

[72] S. Rahaman, J. Hakala, V.-V. Elomaa, T. Eronen, U. Hager, A. Jokinen, A. Kankainen, I.D. Moore, H. Penttilä, S. Rinta-Antila, J. Rissanen, A. Saastamoinen, C. Weber, and J. Äystö. Masses of neutron-rich Ni and Cu isotopes and the shell closure at $Z = 28$, $N = 40$. *The European Physical Journal A*, 34:5–9, 2007.

[73] S. Zhu, R. V. F. Janssens, M. P. Carpenter, C. J. Chiara, R. Broda, B. Fornal, N. Hoteling, W. Królas, T. Lauritsen, T. Pawłat, D. Seweryniak, I. Stefanescu, J. R. Stone, W. B. Walters, X. Wang, and J. Wrzesiński. Nature of yrast excitations near $N = 40$: Level structure of ^{67}Ni. *Phys. Rev. C*, 85:034336, Mar 2012.

[74] E. Caurier, F. Nowacki, and A. Poves. Large-scale shell model calculations for exotic nuclei. *The European Physical Journal A - Hadrons and Nuclei*, 15:145–150, 2002.

[75] L. Gaudefroy, A. Obertelli, S. Péru, N. Pillet, S. Hilaire, J. P. Delaroche, M. Girod, and J. Libert. Collective structure of the $N = 40$ isotones. *Phys. Rev. C*, 80:064313, Dec 2009.

[76] W. Rother, A. Dewald, H. Iwasaki, S. M. Lenzi, K. Starosta, D. Bazin, T. Baugher, B. A. Brown, H. L. Crawford, C. Fransen, A. Gade, T. N. Ginter, T. Glasmacher, G. F. Grinyer, M. Hackstein, G. Ilie, J. Jolie, S. McDaniel, D. Miller, P. Petkov, Th. Pissulla, A. Ratkiewicz, C. A. Ur, P. Voss, K. A. Walsh, D. Weisshaar, and K.-O. Zell. Enhanced Quadrupole Collectivity at $N = 40$: The Case of Neutron-Rich Fe Isotopes. *Phys. Rev. Lett.*, 106:022502, Jan 2011.

[77] J. Ljungvall, A. Görgen, A. Obertelli, W. Korten, E. Clément, G. de France, A. Bürger, J.-P. Delaroche, A. Dewald, A. Gadea, L. Gaudefroy, M. Girod, M. Hackstein, J. Libert, D. Mengoni, F. Nowacki, T. Pissulla, A. Poves, F. Recchia, M. Rejmund, W. Rother, E. Sahin, C. Schmitt, A. Shrivastava, K. Sieja, J. J. Valiente-Dobón, K. O. Zell, and M. Zielińska. Onset of collectivity in neutron-rich Fe isotopes: Toward a new island of inversion? *Phys. Rev. C*, 81:061301(R), Jun 2010.

[78] A. Bürger, T.R. Saito, H. Grawe, H. Hübel, P. Reiter, J. Gerl, M. Górska, H.J. Wollersheim, A. Al-Khatib, A. Banu, T. Beck, F. Becker, P. Bednarczyk, G. Benzoni, A. Bracco, S. Brambilla, P. Bringel, F. Camera, E. Clément, P. Doornenbal, H. Geissel,

A. Görgen, J. Grebosz, G. Hammond, M. Hellström, M. Honma, M. Kavatsyuk, O. Kavatsyuk, M. Kmiecik, I. Kojouharov, W. Korten, N. Kurz, R. Lozeva, A. Maj, S. Mandal, B. Million, S. Muralithar, A. Neusser, F. Nowacki, T. Otsuka, Zs. Podolyák, N. Saito, A.K. Singh, H. Weick, C. Wheldon, O. Wieland, and M. Winkler. Relativistic Coulomb excitation of neutron-rich ^{54,56,58}Cr: On the pathway of magicity from $N = 40$ to $N = 32$. *Physics Letters B*, 622(1-2):29 – 34, 2005.

[79] N. Aoi, E. Takeshita, H. Suzuki, S. Takeuchi, S. Ota, H. Baba, S. Bishop, T. Fukui, Y. Hashimoto, H. J. Ong, E. Ideguchi, K. Ieki, N. Imai, M. Ishihara, H. Iwasaki, S. Kanno, Y. Kondo, T. Kubo, K. Kurita, K. Kusaka, T. Minemura, T. Motobayashi, T. Nakabayashi, T. Nakamura, T. Nakao, M. Niikura, T. Okumura, T. K. Ohnishi, H. Sakurai, S. Shimoura, R. Sugo, D. Suzuki, M. K. Suzuki, M. Tamaki, K. Tanaka, Y. Togano, and K. Yamada. Development of large deformation in ^{62}Cr. *Phys. Rev. Lett.*, 102:012502, Jan 2009.

[80] A. N. Deacon, S. J. Freeman, R. V. F. Janssens, F. R. Xu, M. P. Carpenter, I. R. Calderin, P. Chowdhury, N. J. Hammond, T. Lauritsen, C. J. Lister, D. Seweryniak, J. F. Smith, S. L. Tabor, B. J. Varley, and S. Zhu. Changes in shape polarisation across the odd neutron-rich Cr isotopes. *Physics Letters B*, 622(1-2):151 – 158, 2005.

[81] S. Zhu, A. N. Deacon, S. J. Freeman, R. V. F. Janssens, B. Fornal, M. Honma, F. R. Xu, R. Broda, I. R. Calderin, M. P. Carpenter, P. Chowdhury, F. G. Kondev, W. Królas, T. Lauritsen, S. N. Liddick, C. J. Lister, P. F. Mantica, T. Pawłat, D. Seweryniak, J. F. Smith, S. L. Tabor, B. E. Tomlin, B. J. Varley, and J. Wrzesiński. Level structure of the neutron-rich ^{56,58,60}Cr isotopes: Single-particle and collective aspects. *Phys. Rev. C*, 74:064315, Dec 2006.

[82] A. N. Deacon, D. Steppenbeck, S. Zhu, S. J. Freeman, R. V. F. Janssens, M. P. Carpenter, B. Fornal, M. Honma, B. P. Kay, F. G. Kondev, J. Kozemczak, A. Larabee, T. Lauritsen, C. J. Lister, A. P. Robinson, D. Seweryniak, J. F. Smith, Y. Sun, X. Wang, F. R. Xu, and Y.-C. Yang. Single-particle and collective structures in ^{55}Cr and ^{55}V. *Phys. Rev. C*, 83:064305, Jun 2011.

[83] D. Weisshaar. *NewSpecTcl: Analyzing Software for SeGA + S800 Experiments*, 2009.

[84] *NewSpecTcl*. Customized version of NSCL SpecTcl software: `http://docs.nscl.msu.edu/daq/spectcl/`.

[85] Andreas Fitzler. *Tv User Manual*. Institute for Nuclear Physics, University of Cologne, 2000. `http://www.ikp.uni-koeln.de/misc/doc/Tv_user-manual/Tv_user-manual.html`.

[86] S. Agostinelli, J. Allison, K. Amako, J. Apostolakis, H. Araujo, P. Arce, M. Asai, D. Axen, S. Banerjee, G. Barrand, F. Behner, L. Bellagamba, J. Boudreau, L. Broglia, A. Brunengo, H. Burkhardt, S. Chauvie, J. Chuma, R. Chytracek, G. Cooperman, G. Cosmo, P. Degtyarenko, A. Dell'Acqua, G. Depaola, D. Dietrich, R. Enami, A. Feliciello, C. Ferguson, H. Fesefeldt, G. Folger, F. Foppiano, A. Forti, S. Garelli, S. Giani, R. Giannitrapani, D. Gibin, J.J. Gómez Cadenas, I. González, G. Gracia Abril, G. Greeniaus, W. Greiner, V. Grichine, A. Grossheim, S. Guatelli, P. Gumplinger, R. Hamatsu, K. Hashimoto, H. Hasui, A. Heikkinen, A. Howard, V. Ivanchenko, A. Johnson, F.W. Jones, J. Kallenbach, N. Kanaya, M. Kawabata, Y. Kawabata, M. Kawaguti, S. Kelner, P. Kent, A. Kimura, T. Kodama, R. Kokoulin, M. Kossov, H. Kurashige, E. Lamanna, T. Lampén, V. Lara, V. Lefebure, F. Lei, M. Liendl, W. Lockman, F. Longo, S. Magni, M. Maire, E. Medernach, K. Minamimoto, P. Mora de Freitas, Y. Morita, K. Murakami, M. Nagamatu, R. Nartallo, P. Nieminen, T. Nishimura, K. Ohtsubo, M. Okamura, S. O'Neale, Y. Oohata, K. Paech, J. Perl, A. Pfeiffer, M.G. Pia, F. Ranjard, A. Rybin, S. Sadilov, E. Di Salvo, G. Santin, T. Sasaki, N. Savvas, Y. Sawada, S. Scherer, S. Sei, V. Sirotenko, D. Smith, N. Starkov, H. Stoecker, J. Sulkimo, M. Takahata, S. Tanaka, E. Tcherniaev, E. Safai Tehrani, M. Tropeano, P. Truscott, H. Uno, L. Urban, P. Urban, M. Verderi, A. Walkden, W. Wander, H. Weber, J.P. Wellisch, T. Wenaus, D.C. Williams, D. Wright, T. Yamada, H. Yoshida, and D. Zschiesche. Geant4-a simulation toolkit. *Nuclear Instruments and Methods in Physics Research Section A: Accelerators, Spectrometers, Detectors and Associated Equipment*, 506(3):250 – 303, 2003.

[87] Rene Brun and Fons Rademakers. ROOT - An object oriented data analysis framework. *Nuclear Instruments and Methods in Physics Research Section A: Accelerators, Spectrometers, Detectors and Associated Equipment*, 389(1-2):81 – 86, 1997. New Computing Techniques in Physics Research V.

[88] A. Obertelli. private communication.

[89] Zhou Chunmei. Nuclear Data Sheets Update for A = 197. *Nuclear Data Sheets*, 76(3):399 – 456, 1995.

[90] Alan L. Nichols, Balraj Singh, and Jagdish K. Tuli. Nuclear Data Sheets for A = 62. *Nuclear Data Sheets*, 113(4):973 – 1114, 2012.

[91] B. Pritychenko, J. Choquette, M. Horoi, B. Karamy, and B. Singh. An update of the B(E2) evaluation for transitions in even-even nuclei near. *Atomic Data and Nuclear Data Tables*, 98(4):798 – 811, 2012.

[92] M. Seidlitz, P. Reiter, A. Dewald, O. Möller, B. Bruyneel, S. Christen, F. Finke, C. Fransen, M. Górska, H. Grawe, A. Holler, G. Ilie, T. Kotthaus, P. Kudejová, S. M. Lenzi, S. Mandal, B. Melon, D. Mücher, J.-M. Regis, B. Saha, P. von Brentano,

A. Wiens, and K. O. Zell. Precision lifetime measurements of the first 2^+ and 4^+ states in ^{56}Cr at the $N = 32$ subshell closure. *Phys. Rev. C*, 84:034318, Sep 2011.

[93] L. A. Riley, M. A. Abdelqader, D. Bazin, M. J. Bojazi, B. A. Brown, C. M. Campbell, J. A. Church, P. D. Cottle, D. C. Dinca, J. Enders, A. Gade, T. Glasmacher, M. Honma, S. Horibe, Z. Hu, K. W. Kemper, W. F. Mueller, H. Olliver, T. Otsuka, B. C. Perry, B. T. Roeder, B. M. Sherrill, T. P. Spencer, and J. R. Terry. Thick-target inverse-kinematics proton scattering from ^{46}Ar and the $N = 28$ shell below ^{48}Ca. *Phys. Rev. C*, 72:024311, Aug 2005.

[94] S. J. Freeman, R. V. F. Janssens, B. A. Brown, M. P. Carpenter, S. M. Fischer, N. J. Hammond, M. Honma, T. Lauritsen, C. J. Lister, T. L. Khoo, G. Mukherjee, D. Seweryniak, J. F. Smith, B. J. Varley, M. Whitehead, and S. Zhu. Low-lying levels in ^{59}Cr: Inadequacy of the fp model space and onset of deformation. *Phys. Rev. C*, 69:064301, Jun 2004.

[95] Hiroyuki Sagawa, Toshio Suzuki, and Kouichi Hagino. New structure problems in drip line nuclei. *Nuclear Physics A*, 722(0):C183 – C189, 2003.

[96] W. A. Richter, S. Mkhize, and B. Alex Brown. *sd*-shell observables for the USDA and USDB Hamiltonians. *Phys. Rev. C*, 78:064302, Dec 2008.

[97] J. J. Valiente-Dobón, S. M. Lenzi, S. J. Freeman, S. Lunardi, J. F. Smith, A. Gottardo, F. Della Vedova, E. Farnea, A. Gadea, D. R. Napoli, M. Axiotis, S. Aydin, D. Bazzacco, P. G. Bizzeti, A. M. Bizzeti-Sona, G. Benzoni, D. Bucurescu, L. Corradi, A. N. Deacon, G. De Angelis, E. Fioretto, B. Guiot, M. Ionescu-Bujor, A. Iordachescu, S. Leoni, N. Mărginean, R. Mărginean, P. Mason, R. Menegazzo, D. Mengoni, B. Million, G. Montagnoli, R. Orlandi, F. Recchia, E. Sahin, F. Scarlassara, R. P. Singh, A. M. Stefanini, D. Steppenbeck, S. Szilner, C. A. Ur, B. J. Varley, and O. Wieland. Spectroscopy of neutron-rich $^{59-63}$Mn isotopes. *Phys. Rev. C*, 78:024302, Aug 2008.

[98] H. L. Crawford, P. F. Mantica, J. S. Berryman, R. Broda, B. Fornal, C. R. Hoffman, N. Hoteling, R. V. F. Janssens, S. M. Lenzi, J. Pereira, J. B. Stoker, S. L. Tabor, W. B. Walters, X. Wang, and S. Zhu. Low-energy structure of ^{61}Mn populated following β decay of ^{61}Cr. *Phys. Rev. C*, 79:054320, May 2009.

[99] L. Gaudefroy, O. Sorlin, C. Donzaud, J.C. Angélique, F. Azaiez, C. Bourgeois, V. Chiste, Z. Dlouhy, S. Grévy, D. Guillemaud-Mueller, F. Ibrahim, K.-L. Kratz, M. Lewitowicz, S.M. Lukyanov, I. Matea, J. Mrasek, F. Nowacki, F. de Oliveira Santos, Yu.-E. Penionzhkevich, B. Pfeiffer, F. Pougheon, M.G. Saint-Laurent, and M. Stanoiu. Beta-decay studies of neutron-rich Sc- Cr nuclei. *The European Physical Journal A - Hadrons and Nuclei*, 23(1):41–48, 2005.

[100] G. Audi, O. Bersillon, J. Blachot, and A.H. Wapstra. The nubase evaluation of nuclear and decay properties. *Nuclear Physics A*, 729(1):3 – 128, 2003. The 2003 NUBASE and Atomic Mass Evaluations.

[101] E. Runte, K. L. Gippert, W. D. Schmidt-Ott, P. Tidemand-Petersson, L. Ziegeler, R. Kirchner, O. Klepper, P. O. Larsson, E. Roeckl, D. Schardt, N. Kaffrell, P. Peuser, M. Bernas, P. Dessagne, M. Langevin, and K. Rykaczewski. Decay studies of neutron-rich isotopes of manganese, iron, cobalt, nickel, copper and zinc. *Nuclear Physics A*, 441(2):237 – 260, 1985.

[102] I.Y. Lee. Gamma-ray tracking detectors. *Nuclear Instruments and Methods in Physics Research Section A: Accelerators, Spectrometers, Detectors and Associated Equipment*, 422(1-3):195 – 200, 1999.

[103] A. P. Zuker, J. Retamosa, A. Poves, and E. Caurier. Spherical shell model description of rotational motion. *Phys. Rev. C*, 52:R1741–R1745, Oct 1995.

[104] K. Wimmer *et al.* Single-particle structure of neutron-rich $N = 40$ nuclei, 2012. NSCL experiment.

[105] R. York, G. Bollen, C. Compton, A. Crawford, M. Doleans, T. Glasmacher, W. Hartung, F. Marti, J. Popielarski, J. Vincent, J. Wlodarczak, X. Wu, A. Zeller, and Q. Zhao. FRIB: A New Accelerator Facility for the Production of Rare Isotope Beams. In *Proceedings of SRF 2009; Berling, Germany; September 20-25, 2009*, pages 888–894, 2009.

[106] T. Baugher *et al.* Simulations of CAESAR. In preparation.

[107] V. Bader, A. Gade, D. Weisshaar, T. Baugher, D. Bazin, J. S. Berryman, B. A. Brown, A. Ekström, M. Hjorth-Jensen, S. R. Stroberg, W. B. Walters, K. Wimmer, and R. Winkler. Quadrupole collectivity in neutron-deficient Sn nuclei: ^{104}Sn. Submitted for publication.